# The defining length scales of mesomagnetism: a review

2002 J. Phys.: Condens. Matter 14 R1175

(http://iopscience.iop.org/0953-8984/14/49/201)

INSTITUTE OF PHYSICS PUBLISHING JOURNAL OF PHYSICS: CONDENSED MATTER

J. Phys.: Condens. Matter **14** (2002) R1175–R1262 PII: S0953-8984(02)64917-3

TOPICAL REVIEW

# The defining length scales of mesomagnetism: a review

**C L Dennis**[1], **R P Borges**[1], **L D Buda**[2], **U Ebels**[2], **J F Gregg**[1], **M Hehn**[3], **E Jouguelet**[1], **K Ounadjela**[2], **I Petej**[1], **I L Prejbeanu**[2] and **M J Thornton**[1]

[1] Clarendon Laboratory, University of Oxford, Parks Road, Oxford OX1 3PU, UK
[2] IPCMS, 23 rue du Loess, Strasbourg 67037, France
[3] Laboratoire de Physique des Matériaux, Université Henri Poincaré, 54506 Vandoeuvre lès Nancy, France

E-mail: cindi.dennis@magd.ox.ac.uk

Received 13 May 2002
Published 29 November 2002
Online at stacks.iop.org/JPhysCM/14/R1175

**Abstract**

This review is intended as an introduction to mesomagnetism, with an emphasis on what the defining length scales and their origins are. It includes a brief introduction to the mathematics of domains and domain walls before examining the domain patterns and their stability in 1D and 2D confined magnetic structures. This is followed by an investigation of the effects of size and temperature on confined magnetic structures. Then, the relationship between mesomagnetism and the developing field of spin electronics is discussed. In particular, the various types of magnetoresistance, with an emphasis on the theory and applications of giant magnetoresistance and tunnelling magnetoresistance, are studied. Single electronics are briefly examined before concluding with an outlook on future developments in mesomagnetism.

## Contents

0953-8984/02/491175+88$30.00

## 1. Introduction

Mesomagnetism is the study of the novel physical phenomena which appear when magnetic systems are reduced to the nanoscale. These phenomena arise because magnetic processes are characterized by specific length scales. When the physical size of a magnetic system is engineered to dimensions comparable to or smaller than these characteristic lengths, novel behaviour is observed, including (for example) giant magnetoresistance (GMR), Coulomb blockade, perpendicular anisotropy, superparamagnetism and current induced switching. Furthermore, as technology continues to miniaturize and novel materials are developed, these characteristic length scales and their resulting phenomena define the ultimate limits of devices.

These mesoscopic characteristic length scales have various origins. Many of them—domain size, domain wall width, exchange length and thin film perpendicular anisotropy

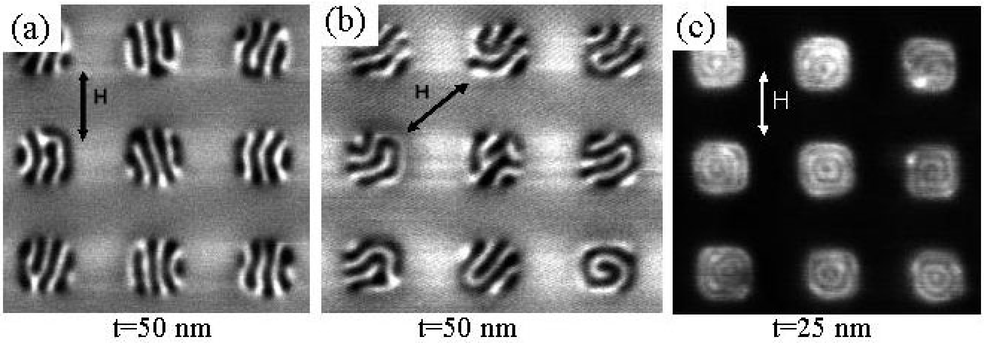

**Figure 1.** Example of stripe domains induced in ~0.5 $\mu$m wide epitaxial Co(0001) dots 50 nm thick and demagnetized (a) parallel to the edge of the square dot and (b) along the diagonal. (A change in domain orientation in an MFM image is indicated by a change from white to black. However, the colours do not indicate an absolute orientation, just that a change has occurred.) (c) Circular stripe domains induced in ~0.5 $\mu$m wide epitaxial Co(0001) dots 25 nm thick and demagnetized parallel to the edge of the square dot. (The dots were fabricated using x-ray lithography and ion beam etching from continuous epitaxial hcp Co(0001) films in arrays of 5 × 5 mm$^2$. The dots have a square basal plane with 0.5 $\mu$m lateral dimension, 1$\mu$m array periodicity and a thickness varying from 10 to 150 nm [4, 5].)

threshold—are governed by minimization of energy considerations. Others, like the spin diffusion length and spin precession length, are the result of diffusion processes for energy, momentum or magnetization. The phenomena that appear when magnetic systems are engineered on these length scales may be very diverse since a wide variety of combinations of several characteristic lengths may be involved.

These mesoscopic phenomena place ultimate limits on device performance, improve current technology or generate new technology, and it is these ultimate materials/device engineering interests which are driving research in mesomagnetism. The electronics, data storage and computer industries are continuously pushing the limits of technology, trying to make things better, faster and cheaper; other industries are also involved, including medical technology. This has led to the development of novel devices (such as biological physics sensors for medicine) as well as advancements in GMR for read heads in data storage, the investigations into domains in granular media for data storage, magnetic field sensing for automotive sensors (and other applications which require sensors), MRAM and many others. Other investigations are pursuing more advanced concepts like single electronics for quantum computers.

This review is intended as an introduction to mesomagnetism. The aim is to explore the connections between the different phenomena and their characteristic length scales as well as their relevance to (or operation in) devices. Therefore, only the length scales relevant for describing these phenomena are discussed here. Throughout, the reader will be pointed to other sources for further details.

## 2. Domains

Perhaps the most fundamental of all of the characteristic length scales is the exchange length. It is balancing the energy associated with this length scale (the exchange energy) with the other energy terms (see section 2.2) present in the magnet—anisotropy, magnetostatic, Zeeman and magnetoelastic—that defines the size of the domains (regions of uniform magnetization) and the width of the domain walls (regions of transition between one area of uniform magnetization in a given direction and another region of uniform magnetization in a different direction—see figure 1). Put differently, alternating the direction of the magnetization with respect to a surface can minimize the energy in the static magnetic fields surrounding a finite, magnetized material. Many types of domains are possible depending on what energy contribution is dominant and what the magnetic history is. These differences enable applications such as high-density memory storage in magnetic bubbles or magnetoresistance from striped domains [1]. For the interested reader, several excellent reviews by Kittel [2] and Hubert [3] more completely summarize this area of magnetism.

### *2.1. A brief history of... magnetic domains*

Although first considered in Weiss's famous work [6], the term 'domain' does not appear until later [7]. Originally, domains[4] were only an abstract construction to explain

(1) that even far below the Curie temperature, the total magnetization of a magnet is not the same as its saturation magnetization;
(2) that a permanent magnet can be made from a ferromagnetic material by applying a magnetic field;
(3) the presence of hysteresis in the magnetization curve and the necessity of a coercive field to remove any net magnetization and
(4) that ferromagnetic materials can simultaneously have zero average magnetization and non-zero local magnetization.

However, not until the 1930s with the works of Sixtus and Tonks [13] and Bitter [14] was Weiss's theory fully confirmed. Not until 1935 did Landau and Lifshitz [15] propose that domains originate from the minimization of the magnetostatic energy stemming from the magnetic dipolar interaction.

### *2.2. Energy considerations in domain formation*

*2.2.1. General overview.* Before diving into the detail and mathematics of domain formation, a general overview of the factors involved is appropriate. Three different energy terms dominate domain formation: magnetostatic, exchange and anisotropy. (Other energies also play a role, but these are the most important.) The effect of each of these can be illustrated using a large[5] rectangular magnet magnetized along its easy axis (figure 2(a)). In this case, the exchange energy (the energy proportional to the angle between two spins) and the anisotropy energy (the energy proportional to the orientation of the magnetization relative to the crystalline axes) are both zero. However, the magnetostatic energy (the energy due to the field produced by the magnet) is maximized since the magnet acts like a single, giant dipole. In order to minimize the total energy, two parallel domains and two closure domains will form, as shown in figure 2(b). This increases the anisotropy and exchange energies due to the transition regions between the domains, but significantly reduces the magnetostatic energy. The total energy can be further reduced by decreasing the size of the closure domains (the shaded region in figure 2(c)) by forming three additional domains. This reduces the overall anisotropy energy (since fewer moments are aligned perpendicular to the easy direction) as well as the magnetostatic energy, but the exchange and anisotropy energies originating from the transition regions increase. However, if the magnet is small enough, then the anisotropy energy cost of the shaded areas

---

[4] The concept of domains is not restrained to magnetism [8]; it is also found in ferrofluids [9], Langmuir layers [10], superconductivity (as the intermediate state) [11], liquid crystals [12] and block copolymers [12].

[5] 'Large' means exceeding the monodomain size (see section 4.1) of a particle or a thin film of that material.

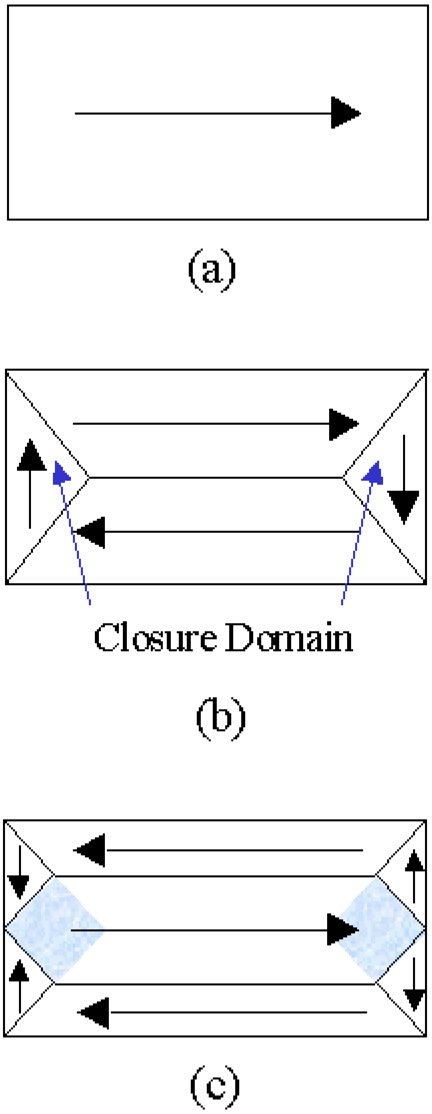

**Figure 2.** Overall pattern of domain formation in a large rectangular magnet. The black arrows indicate the magnetization direction of each domain.

shown in figure 2(c) is less than the exchange and anisotropy energy cost to form the extra domain walls, so figure 2(b) would be the final domain configuration. Therefore, as this example shows, although the formation of domains is driven by the magnetostatic energy, the actual domain configuration is determined by the total anisotropy energy and the competition between the exchange and anisotropy energies during domain wall formation.

*2.2.2. Mathematics.* First proposed by Vleck [16], the energy required to rotate one atomic spin with respect to its neighbours (overcoming the Pauli principle which tends to align the magnetic moments parallel—ferromagnetic configuration—or antiparallel—

antiferromagnetic configuration) is called the exchange energy $E_{exchange}$. 'Direct' exchange interaction is the sum of all of the different interactions[6]—spin–spin, spin–orbit etc. However, although equation (1) is commonly referred to as the direct exchange interaction, it is actually an effective spin–spin interaction resulting from symmetry rules and orbital overlap [17]. Equation (1) is the quantum mechanical version:

$$E_{exchange} = -J\boldsymbol{S}_1 \cdot \boldsymbol{S}_2 \tag{1}$$

where $J$ is the exchange parameter and $S_j$ is the spin of the electron. The classical expression is analogous, except for an arbitrary factor of two which is generally included:

$$E_{exchange} = -\sum_{i>j} 2J_{ij}\boldsymbol{S}_i \cdot \boldsymbol{S}_j \tag{2}$$

where $J$ is the exchange integral linking the $i$th atom with spin $S_i$ to the $j$th atom with spin $S_j$. Using the classical expression (equation (2)) and assuming that only the nearest neighbour interactions are important, the energy per unit area can be determined for a specific crystal lattice (e.g. simple cubic) to be

$$E_{exchange} = \int_{-\infty}^{\infty} \frac{JS^2}{a} (\nabla \boldsymbol{M})^2 \,\mathrm{d}r^3 = A \int_{-\infty}^{\infty} (\nabla \boldsymbol{M})^2 \,\mathrm{d}r^3 \tag{3}$$

where $A = JS^2/a$ and is the exchange parameter (approximately 1 eV times a proportionality factor related to the overlap of the wavefunctions) and $a$ is the lattice spacing. Therefore, the probability of an individual spin flipping is proportional to

$$\mathrm{e}^{(E_{exchange}/k_B T)}. \tag{4}$$

When the material is ferromagnetic at room temperature and the measurement is made at a few Kelvin, this probability is exponentially small. Therefore, the exchange energy results in a characteristic exchange length for the material—the distance over which it is energetically favourable for all of the magnetic moments to be aligned.

However, the energy required to rotate the entire magnetization vector of the particle without moving the particle or changing the relative orientation between spins is called the magnetocrystalline anisotropy energy. It is the result of the interaction between the crystalline fields of the ferromagnet with spin–orbit coupling. Therefore, when the magnetic moments are directed along certain axes called the easy axes, which are determined by the symmetry of the crystal, the energy is minimized. Along other directions, called the hard axes, the energy is maximized. In the case of a cubic crystal[7], the anisotropy energy can be written as

$$E_{anisotropy} \approx K_1[m_1^2m_2^2 + m_1^2m_3^2 + m_2^2m_3^2] + K_2m_1^2m_2^2m_3^2 \tag{5}$$

where $K_i$ is the magnetocrystalline anisotropy constant along the $i$th direction and $\boldsymbol{M} = m_1\underline{\boldsymbol{i}}+m_2\underline{\boldsymbol{j}}+m_3\underline{\boldsymbol{k}}$ is the magnetization vector. The ratio of the exchange energy to the anisotropy energy is approximately $10^{-5}$–$10^{-3}$; the exchange energy dominates.

The magnetostatic energy[8] dominates domain formation [18, 19]. Each single domain produces free surface magnetic poles (N and S), which give rise to stray fields and, therefore, magnetostatic energy. This can be calculated from Maxwell's equations:

$$\begin{aligned} \nabla \cdot \boldsymbol{B} &= \nabla \cdot (\mu_0 \boldsymbol{H} + \boldsymbol{M}) = 0 \\ \nabla \cdot \boldsymbol{H}_d &= -\nabla \cdot (\boldsymbol{M}/\mu_0) \end{aligned} \tag{6}$$

---

[6] The exchange interaction exponentially decays so it is only a short-range effect.

[7] For uniaxial or orthorhombic or any of the other anisotropies, a different form of the energy is written. See chapter 3 section 2 of [3] for more information.

[8] Magnetostatic energy is a dipolar interaction so it decreases as $r^{-3}$ and is a non-local mechanism.

where $H_d$ is the stray field generated by the divergence of the magnetization $M$. In analogy with electrostatics, the sinks and sources of magnetization act like 'magnetic charges' that are always balanced, but are really just the free surface magnetic poles. The energy can now be given by

$$E_{magnetostatic} = \tfrac{1}{2}\mu_0 \int_{all\,space} H_d^2 \,\mathrm{d}V = -\tfrac{1}{2} \int_{sample} \boldsymbol{H}_d \cdot \boldsymbol{M} \,\mathrm{d}V. \tag{7}$$

The general solution for equation (7) can be calculated through a fictitious potential[9] of 'magnetic poles' $\varphi(\boldsymbol{r})$. Knowing the density of charges in the volume ($\rho$) and on the surface ($\sigma$):

$$\begin{aligned} \rho(\boldsymbol{r}) &= -\nabla \cdot \boldsymbol{M}(\boldsymbol{r}) \\ \sigma &= \boldsymbol{M} \cdot \bar{n} \end{aligned} \tag{8}$$

where $n$ is the normal to the surface, yields the total internal field, just as in electrostatic theory:

$$\varphi(r) = \frac{M}{4\pi\mu_0}\left[\int_V \frac{\rho(r')}{|r - r'|}\,\mathrm{d}V' + \oint_S \frac{\sigma(r')}{|r - r'|}\,\mathrm{d}S'\right]. \tag{9}$$

Once $\varphi(\boldsymbol{r})$ is known, it can be directly substituted into equation (7) to find the total energy.

Alternatively, the demagnetizing field[10] can be written in terms of a demagnetizing tensor $N$:

$$H_d = \frac{-\boldsymbol{N} \cdot \boldsymbol{M}}{\mu_0}. \tag{10}$$

For a uniformly magnetized ellipsoid or for a thin, infinite film magnetized perpendicular to the surface, $N$ can be calculated exactly and is a diagonal tensor [20] or a scalar, respectively. In the latter case, this shape demagnetizing energy takes the same form as the uniaxial anisotropy[11] (see section 4.1), and can be treated analogously.

$$K_d = \frac{M^2}{2\mu_0}. \tag{11}$$

Since $K_d$ is a measure of the maximum energy density that may be connected with the stray fields, the ratio

$$Q = \frac{K}{K_d} \tag{12}$$

where $K$ is the appropriate anisotropy constant, is often useful for determining how strong a particular energy is. Unfortunately, if the anisotropy energy is not very high compared to the demagnetization energy calculated by equation (11), the torque formed by the new demagnetization field can lead to a far more complicated equation than the electrostatic analogy [21]. The magnetization vector is then approximated by assuming the magnetization is nearly parallel to an easy direction so that the permeability tensor $\varepsilon^*$ can be diagonalized.

The fourth energy contributor is the Zeeman energy, or the interaction of the magnetization with the external field. This is given by

$$E_{Zeeman} = -\mu_0 \int \boldsymbol{H}_{external} \cdot \boldsymbol{M} \,\mathrm{d}V \tag{13}$$

where $\boldsymbol{H}_{external}$ is the external applied field. For a uniform external field, this depends only upon the average magnetization of the sample, and not on the particular domain structure or the sample shape, unlike the magnetostatic energy just discussed.

---

[9] The absence of internal current means that $\nabla \times \boldsymbol{H} = 0$ which implies that $H = -\nabla\varphi(r)$.

[10] The demagnetizing field points in the opposite direction to the magnetization.

[11] Uniaxial anisotropy occurs when there is only one easy axis pointing along a specific detection.

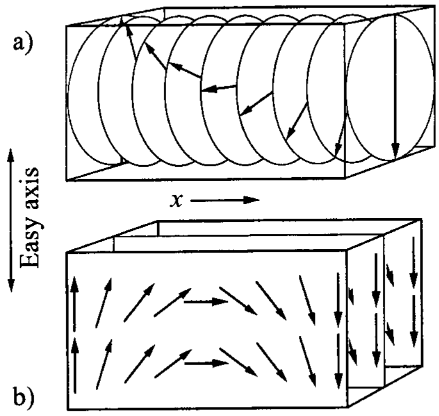

**Figure 3.** Variation of the magnetization in (a) a Bloch wall or (b) a Néel wall in a planar film where the magnetization in the domain is parallel to the film plane. (From [3].)

The final energy contributor is the magnetoelastic energy. This energy is the result of the deformation that a magnetic body experiences under the influence of a magnetic interaction. In general, this is described by an asymmetric tensor of elastic distortion, $p(r)$. However, these effects are generally small in ferromagnetism, and play an even smaller role compared to the other four[12]. References [17] and [22] contain more information for the interested reader. Together, these five energies determine the domain formation with equations (1)–(13) defining the micromagnetic equations ruling the internal structure of domains. For most materials, the domain size ranges from 0.1 to 10 $\mu$m.

### 2.3. *Characteristics of domain walls*

The formation of a domain wall is energetically costly since the deviations of the magnetization involve exchange, anisotropy, magnetostatic, Zeeman and magnetoelastic energy. Therefore, the ground state of an *infinite* bulk material would be a homogeneously magnetized single-domain state. However, real materials have finite boundaries, which involve a discontinuity in the magnetization, and therefore produce surface magnetic poles that give rise to shape demagnetization fields. The tendency to reduce these surface demagnetization fields (pole avoidance principle) ultimately gives rise to the formation of multiple domains, where the reduction in demagnetization energy and the cost of forming a wall are balanced against each other. Furthermore, the width of the domain wall is determined by this same competition [15, 23].

When a magnetic field is applied, domains with the magnetization oriented along the applied field direction grow by displacement of the walls at the expense of domains with the magnetization oriented opposite to the field direction. An alternative view is that the movement of domain walls modifies the overall magnetization. Inside the wall, a continuous variation of spin vector direction costs less energy than an abrupt transition. This results in two main types of domain wall: Bloch walls and Néel walls. The difference between these two types can be best illustrated for the case of a 180° wall in an infinite uniaxial (see footnote 11) medium (see figure 3). Assuming that the wall plane contains the anisotropy axis, then the domain magnetizations are parallel to the wall. However, if the magnetizations rotate parallel to the

---

[12] The zeroth order represents the non-deformed lattice, the first order represents the magnetoelastic interaction energy and the second order represents the elastic energy, which is usually assumed to be independent of the magnetization direction.

wall plane then the component of the magnetization perpendicular to the wall is the same on both sides and the stray field will have its smallest value (zero). This mode is called a Bloch wall. Néel walls occur when the component of the magnetization perpendicular to the wall changes during the rotation—i.e. the magnetizations do not rotate parallel to the wall plane. Bloch walls are generally favoured, but Néel walls can be preferable in thin films and in applied fields.

Using the simple case outlined above, it would appear that taking the longest distance to flip the spin direction from ↑ to ↓ would minimize the energy (see figure 3). This does minimize the exchange energy, but since the spins are attached to atoms in a crystal lattice, changing the spin orientation in the material costs anisotropy energy. The compromise between the exchange and anisotropy energy imposes a thickness $\lambda$ on the domain wall that is approximately given by

$$\lambda \sim a\left(\frac{E_{exchange}}{E_{anisotropy}}\right)^{1/2} \tag{14}$$

where $a$ is the lattice spacing. For a more exact solution, minimizing both energies

$$\begin{aligned} E_{exchange} &= A\left(\frac{\mathrm{d}\varphi(x)}{\mathrm{d}x}\right)^2 \\ E_{anisotropy} &= K_1 \cos^2 \varphi(x) \end{aligned} \tag{15}$$

yields the equation for the angle of rotation $\varphi(x)$

$$\sin\varphi(x) = \tanh\frac{x}{\lambda} \tag{16}$$

and the domain wall width

$$\lambda = \left(\frac{A}{K_1}\right)^{1/2} \tag{17}$$

where $A$ is the exchange parameter given in equation (3). The transition between two magnetizations is, in the simplest case, described by the formalism of Bloch walls in a single variable $\varphi$. However, adding anisotropy or demagnetization energy introduces a second angle of variation according to the crystal structure and shape. The magnetization, therefore, does not vary along only a single line defined by the angle $\varphi$, but on a spherical surface (figure 4).

In the case of a thin film (figure 3), energy minimization will vary the angle $\varphi$ from $-90°$ to $90°$ by changing the magnetization parallel to the surface in order to restrict the demagnetization effects created by the proximity of the planes. When the demagnetization field begins to dominate, the wall will be a Néel wall [24] with a characteristic length of

$$\lambda_{N\acute{e}el} = \sqrt{A/K_d}. \tag{18}$$

Domain walls range between 10 and 100 nm wide for most materials.

### 2.4. Perpendicular anisotropy

The first example of mesomagnetism occurs when one of the dimensions of a bulk magnet is reduced to the nanoscale, thereby forming a thin film. In these systems, the energy terms must be broken up into two different parts—the energy per unit volume and the energy per unit surface. When the volume energy dominates, then the shape demagnetization field from the perpendicular surfaces prefers an alignment of the magnetization parallel to the film plane. However, the presence of magnetic anisotropies (excluding shape anisotropy) can lead to the dominance of the surface energy. When this so-called perpendicular anisotropy threshold is

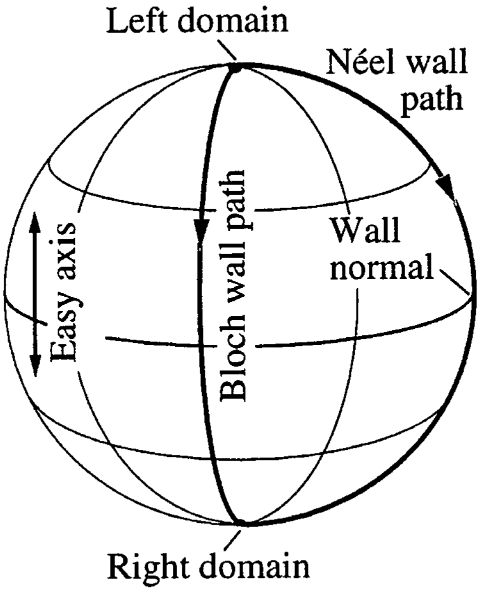

Figure 4. Geometric description of the magnetization on a spherical surface $(\varphi, \theta)$. (From [3].)

satisfied, the magnetization changes orientation, making it possible for the magnetization to lie perpendicular to the film plane. One important case is that of a uniaxial anisotropy where the crystalline orientation favours an alignment of the magnetization out of the film plane (called perpendicular films). There was a great deal of interest in the 1970s in these perpendicular films, primarily in single crystals of orthoferrites, hexagonal ferrites and magnetic garnets, with the idea of using the observed stable domain structures for storing and processing binary data in magnetic recording devices [25–27].

### *2.5. Types of domain*

In thin, perpendicular films, the competition between the shape demagnetization fields and the out-of-plane magnetocrystalline anisotropy induces a periodic variation of the order parameter leading to typical domain patterns which, depending on the magnetic history, can be either circular cylinders (bubble domains) [28] or serpentines (stripe domains) [3, 17, 22, 25, 29, 30] where the width is defined by the material parameters of exchange energy, saturation magnetization and uniaxial anisotropy and scales with the inverse of the magnetization [3, 17, 22, 25]. Typical bubble diameters in the metallic oxides mentioned in section 2.4 are on the order of 10 $\mu$m [25–27], and do not allow for sufficiently dense packing of information to be competitive. Fortunately, the material parameters of metallic thin films are all at least one order of magnitude larger than those of the oxide materials, giving rise to stripe or bubble domains with dimensions between 10 and 100 nm [31–36]. Therefore, the domains in metallic films are 100–1000 times smaller than in the metallic oxides, which is obviously preferable from the application point of view.

## 3. Domains in confined magnetic structures

Although domains, domain walls and their characteristic length scales (the exchange length and perpendicular anisotropy threshold) play a major role throughout mesomagnetism, it is very important at this point to take a look at what happens to the domains when a magnetic structure is confined to the nanoscale—the region of importance to mesomagnetism. The domain structure of this region is examined not only experimentally with magnetic force microscopy (MFM), but also theoretically, with micromagnetic calculations based on first principles (equations (1)–(13)), in order to correlate the shape and size of these magnetic mesoscopic structures with the micromagnetic configurations. Furthermore, the dependence of the domain structure on the strength and direction of the applied field, the stability of the domain configurations and the methods of magnetization reversal will also be examined. Specifically, the structures considered are sub-micron dots (three-dimensional confinement), rings (three-dimensional confinement) and wires (two-dimensional confinement), sufficiently far from each other so that any interactions can be neglected. (The effect of dipolar interaction in closely packed arrays[13] is an interesting subject area on its own but goes beyond the scope of this review.)

### *3.1. Reduction of lateral sizes—an overview*

As outlined earlier in section 2.2, domains are formed to reduce demagnetization energies arising at the sample surfaces. For each system, different domain configurations or magnetization distributions can be induced, depending on the magnetic history. These different configurations will generally be characterized by different energies. Besides the dependence on the particle shape and size, the various possible domain configurations will also be determined by the strength and symmetry of its magnetic anisotropy.

A reduction of the system size generally enhances the relative importance of the surface boundaries. For example, starting from an in-plane magnetized continuous film, the demagnetization fields arising at the edges are negligible compared to the bulk of the film and the ground state of the film is the single-domain state. Reducing the lateral sizes of the film, the demagnetization fields across the film increase and, at some point, induce a domain structure [3, 49]. Interesting properties are expected when the dimensions are further reduced, such that they become comparable to the domain size, the domain wall width (20 nm in hcp Co) or the exchange length (3.37 nm for Co) [3, 4, 50–53]. In particular, below a critical system size, it is predicted that domain formation is suppressed and the magnetic particle is in a single-domain state (see section 4.1).

First, the influence of the thickness of the thin film with perpendicular anisotropy (see section 2.4) needs to be understood. Then, the influence of the reduction of the lateral sizes in two dimensions will be discussed for Co(0001) dots with perpendicular uniaxial anisotropies for the three thickness regions of figure 5(a) with (i) perpendicular stripe domains, (ii) canted stripe domains and (iii) in-plane magnetization. The reduction of the lateral sizes of the continuous film in only one dimension, yielding wires, is discussed in section 3.5.

### *3.2. Stripe domains*

Recently, the domain configurations in thin hcp Co(0001) films grown on Ru buffers have been studied as a function of film thickness [31]. The relatively strong perpendicular uniaxial magnetocrystalline anisotropy ($K_u = 6 \times 10^6$ erg cm$^{-3}$) of these films has been compared to the shape demagnetization energy $K_d$ yielding a $Q$-factor (equation (12)) of 0.4 [3, 31, 32]. In principle, this means that the anisotropy is not strong enough to overcome the demagnetization field. However, upon domain formation the effective demagnetization field is reduced to the point that a perpendicular orientation of the magnetization inside the domains can be stable. Typical

---

[13] Some of the recent work on the interactions of self-assembled arrays of nanoparticles is discussed in [37–48].

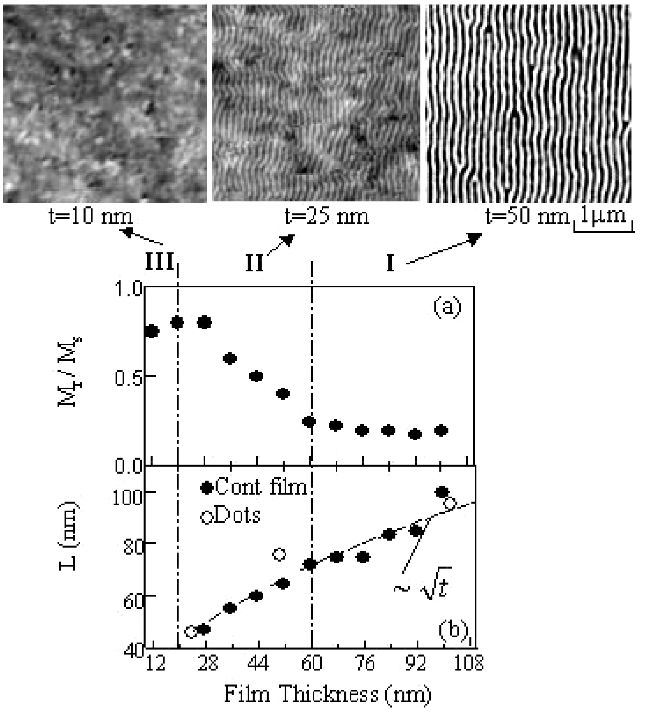

**Figure 5.** (a) MFM images of stripe domain structures developing in epitaxial Co(0001) thin films. Images are shown for a strong stripe structure ($t = 50$ nm), a weak stripe structure ($t = 25$ nm) and an in-plane magnetized film ($t = 10$ nm). These three images correspond to the three regions I–III where the thickness dependence of the in-plane remnance ratio $M_r/M_s$ is shown. (b) The thickness dependence of the domain width $\lambda$ for continuous Co(0001) films (closed circles) and 500 nm$^2$ Co(0001) dots (open circles). The dotted curve is a fit to $t^{1/2}$.

MFM images for stripe domains in Co films are shown in figure 5(a), from which the domain width $\lambda$ as a function of film thickness $t$ was deduced (figure 5(b)). $\lambda$ decreases with decreasing $t$ proportional to $t^{1/2}$ in accordance with Kittel's law for stripe domains [29]. In contrast, the ratio $\lambda/t$, which scales the demagnetization field inside a single domain, increases. This means that the effective demagnetization field inside a single stripe domain increases upon reducing $t$, causing the magnetization to rotate into the film plane for a ratio $\lambda/t$ potentially larger than unity [17, 22, 54]. This canting is seen in the MFM images (figure 5(a)) by the decreasing contrast of the stripe domains for $t = 50$ and 25 nm and the loss of any stripe domain contrast in the thinnest film. The reorientation of the magnetization is a continuous rotation process as indicated by the thickness dependence of the in-plane remnance ratio $M_r/M_s$ shown in figure 5(a). Above 60 nm (region I) the in-plane remnance is low, given only by the canted spins inside the domain wall, while the domain magnetization is perpendicular to the film plane. In the intermediate range (region II), the remnance increases indicating a canting of the domain magnetization towards the film plane. Below 20 nm (region III), the magnetization is fully in plane.

### *3.3. Domains in dots*

*3.3.1. Perpendicular dots.* The MFM images for square Co dots (500 nm) are shown in figure 1 for two different in-plane demagnetization states for fields applied (a) parallel to the dot edge and (b) parallel to the dot diagonal. These dots have a thickness of 50 nm corresponding to thickness region I, figure 5, of perpendicular domain magnetization. For these dots, the influence of the thickness and the effect of shape are considered [4, 5, 55, 56].

(a) *Effect of height.* The number of domains inside the dots increases with decreasing dot thickness, corresponding to a decrease in domain size in much the same way as in continuous thin films (see figure 5). When the domain size is much smaller than the lateral dimension of the dot, one expects identical behaviour for a continuous film and a magnetic dot. This is verified in figure 5(b) where the domain size as a function of thickness is compared for the continuous films (closed circles) and the dots (open circles) [56]. The dependence of the domain size on thickness is the same in both cases. This indicates that the magnetostatic energy at any point inside a domain is primarily determined by nearby domains.

(b) *Effect of shape.* While the domain sizes do not differ much between square dots and continuous films, the effects of the shape and finite size can be clearly observed for the alignment and order of the stripe domain pattern. For the continuous films, the stripe domain structure shown for $t = 50$ nm in figure 5(a) is induced by an in-plane demagnetization procedure which results in well aligned stripes oriented along the applied field direction, independent of the orientation within the film plane. In the case of the square dots, shown in figure 1, it is observed that the stripes are not very straight and can show a strong bending away from the field direction. Furthermore, this mis-orientation and bending is more pronounced when applying the field along the diagonal (figure 1(b)). The bending in the case of figure 1(a) can be explained by the nucleation process of the stripe domains [57]. However, for the demagnetization along the dot diagonal, domains are nucleated which have a tendency to align themselves parallel to the edges rather than to the demagnetization field direction and which try to avoid the corners of the dots [55, 56]. A possible explanation for this [53, 58] is that at saturation along the diagonal, the magnetization is in plane, yielding an inhomogeneous demagnetization field across the square. The demagnetization fields at the corners are much stronger and induce an inhomogeneous alignment of the magnetization to reduce the field (in a manner similar to the leaf state shown in figure 13(b)). Since the domain walls orient themselves parallel to the local field at nucleation, an inhomogeneous demagnetization field in addition to the applied field yields an effective local field that results in strongly curved stripe domains that avoid corners.

*3.3.2. Canted dots.* The MFM images for square Co dots 500 nm wide and 25 nm thick shown in figure 1(c) [4, 5, 56] correspond to the thickness region II in figure 5, with strong canting of the domain magnetization towards the film plane. In the dots, the stripes form concentric circles of alternating black and white domains tending to keep the stripes parallel to the edges of the dots. This circular arrangement implies that a singularity occurs at the centre of the dot where the in-plane magnetization reorients fully perpendicular to the plane to form a so-called vortex structure. This pattern is obtained independent of the orientation of the in-plane demagnetization field and, therefore, must be analysed in terms of the in-plane and out-of-plane components of the canted domain magnetization, which give rise to in-plane and out-of-plane demagnetization fields. The tendency to reduce the out-of-plane demagnetization field component induces the alternating stripes. In contrast, the presence of an in-plane magnetization component, giving rise to in-plane demagnetization fields, induces the circular arrangement of the stripes in order to avoid surface magnetic poles at the dot edges. This indicates that strong effects are expected when the magnetization component is fully in plane in dots patterned from Co(0001) films less than 20 nm thick (region III of figure 5).

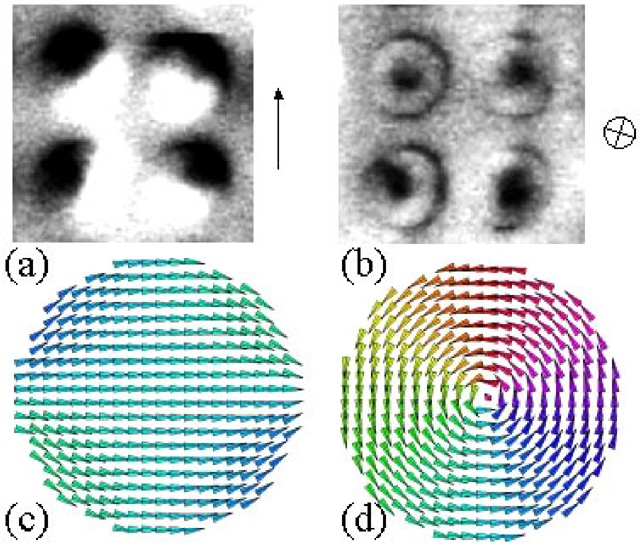

**Figure 6.** MFM images of (a) a single-domain structure and (b) a vortex type structure observed in 200 nm diameter epitaxial Co(0001) circular dots where $t = 10$ nm; (c) and (d) are the corresponding magnetization vector plots obtained from three-dimensional micromagnetic modelling.

*3.3.3. In-plane circular dots.* Since the presence of an in-plane magnetization component can have a drastic influence on the geometric arrangement of the stripe domains, we will consider only elements patterned from in-plane magnetized materials. These materials correspond either to those described in figure 5 in thickness region III (the magnetization in the continuous film is fully in-plane), or materials without magnetic anisotropy.

For these in-plane films, the reduction of the lateral sizes first induces a multi-domain structure in order to minimize the edge demagnetization fields. When the lateral dimensions of the element become comparable to the width of the domains, only simple magnetization configurations can be realized as a direct consequence of the finite size effect [3, 59]. Upon further size reduction comparable to the length scale of the domain wall width, the domain structure will finally become single domain [3, 60].

(a) *Single-domain and vortex configurations.* MFM investigations of arrays of epitaxial circular Co(0001) dots of 200 nm diameter have shown that different magnetic states can be induced depending on the dot dimensions as well as on the magnetic history [50, 61]. In figure 6, two examples are shown for $t = 10$ nm after in-plane saturation and out-of-plane demagnetization. The strong dipolar contrast in figure 6(a) is interpreted as a single-domain state while the weaker contrast with a dark spot in the centre in figure 6(b) is indicative of a vortex-like state for which the magnetization vectors remain parallel to the edges. The circular magnetization pattern results in a singularity in the centre of the dot where the magnetization becomes out of plane, giving the name to this magnetization configuration. Similar observations have been made by several authors for polycrystalline circular dots, which do not exhibit magnetocrystalline anisotropy [51, 52, 62, 63], as well as on elliptical or elongated dots [64–67]. The Lorentz transmission electron microscopy observations reported by Schneider *et al* [52] are particularly nice and they are detailed further in figure 9.

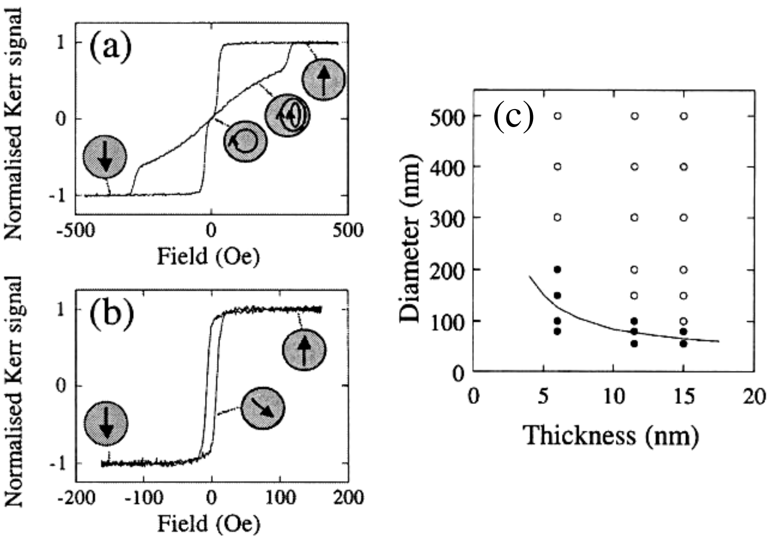

**Figure 7.** Hysteresis loops measured by Kerr magnetometry from supermalloy NiFeMo circular dots of $t = 10$ nm and (a) 300 nm or (b) 100 nm in diameter. (c) Experimental phase diagram denoting the single-domain (filled circles) and vortex states (open circles) as a function of dot diameter and thickness. (From [60].)

(b) *Reversal of the single-domain and vortex configurations.* Further experimental evidence of the two magnetization configurations was given by Cowburn *et al* [60]. They have measured two classes of magnetization loops (figure 7) by in-plane Kerr magnetometry on soft NiFeMo (supermalloy) circular dots as a function of the lateral dot dimension and the dot height. These loops are reminiscent of either a flux-closing type of magnetic structure with the formation of a central vortex (figure 7(a)) or a single-domain structure in which the magnetization is aligned along one specific direction within the dot (figure 7(b)).

(i) *Single-domain reversal in in-plane fields.* As shown in the hysteresis loop in figure 7(b), for a 100 nm wide and 10 nm thick NiFeMo dot array, the single-domain loop retains a high remnance at zero field and switches abruptly at very low field because of the absence of anisotropy [60]. This reversal is classically described by the Stoner–Wohlfarth model [3, 68, 69], which treats the reversal process as a coherent rotation of the magnetization. This reversal type has been further confirmed by MFM imaging under a magnetic field performed on polycrystalline Co dots [70], which display a purely dipole character (figure 8). Varying the field shows that the magnetization rotates coherently and locks on the opposite direction.

(ii) *Vortex reversal in in-plane fields.* As seen from figure 7(a) for a 300 nm wide and 10 nm thick NiFeMo dot array [60], when the applied field is reduced from saturation, the dots retain full moment until a critical field slightly above zero field, when nearly all the magnetization is lost. This sudden loss of magnetization is characteristic of the formation of a flux-closing configuration.

This description of the macroscopic hysteresis loop taken from an array of dots is in agreement with the observation of the reversal of a flux-closure structure of soft NiFe dots (figure 9(a)), reported recently by Schneider *et al* [52]. The observation started by applying an in-plane field of −200 Oe, which is sufficiently high to saturate the discs to the left. Increasing the magnetic field from saturation first leads to the formation of

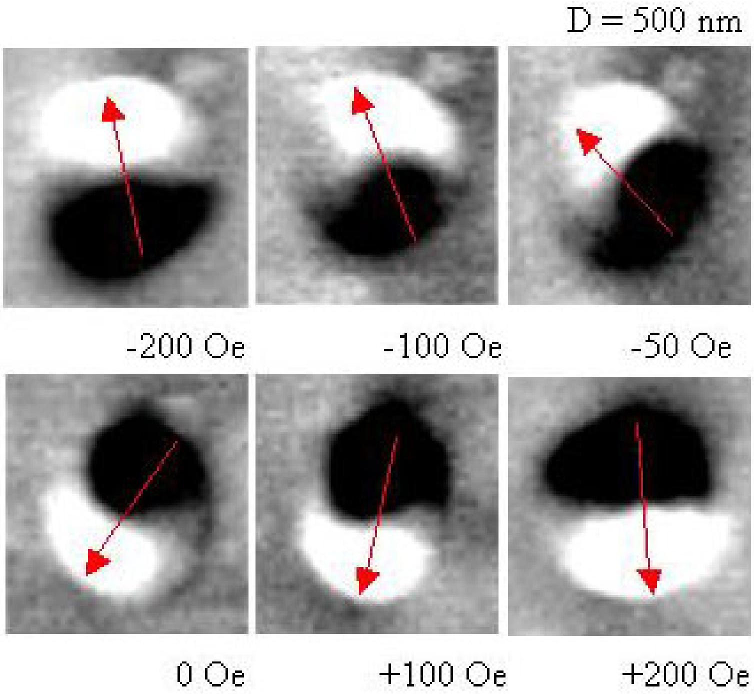

**Figure 8.** MFM images as a function of applied field for $t = 10$ nm polycrystalline circular Co dots 500 nm in diameter. The field values given correspond to those of the external applied field generated by two permanent magnets with variable separation. The actual field is the sum of the applied and the tip field.

magnetization inhomogeneities at the edges of the dots. A vortex state appears for a field of $-60$ Oe, but not at the centre of the dot. This indicates that the magnetic rotation centre moves perpendicular to the direction of the applied field to give rise to a net contribution of the magnetization along the direction of the applied field. Further increase of the external field results in the motion of the vortex (perpendicular to the applied field) until zero field when the vortex centre coincides with the geometric disc centre. This then results in a zero remnant magnetization in agreement with the $M$–$H$ curves shown in figure 7(a). Field reversal shifts the vortex centre towards the particle border as shown in figure 9(a).
This experimental observation is in agreement with two-dimensional numerical micromagnetic calculations using the NIST OOMMF code [71]. As shown in figure 9(b), at the early stage of the reversal process, a magnetization vortex is formed at the upper edge of the element. The polarity of the magnetization circulation is such that the bottom part of the magnetization vortex is in the same direction as the applied reversing field. At zero field the vortex is in the centre and during the field reversal the vortex is forced to the lower edge of the dot element.

In figure 9(c), MFM images are given for the reversal obtained on polycrystalline Co dots [70]. This field-dependent sequence shows the transformation of the single-domain state at negative saturation, into the vortex state at zero field and finally into the reversed single-domain state at positive saturation. Similar MFM observation have been reported by Pokhil *et al* [63] on NiFe discs 800 nm in diameter and varying thickness (5–50 nm). It is interesting to note that in these experiments on the thinner dots, the deviations from

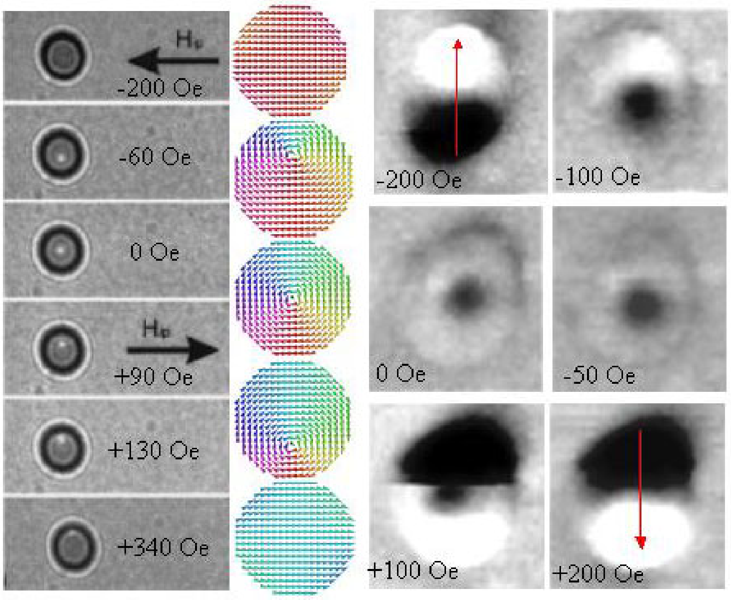

**Figure 9.** Lorentz microscopy images for circular permalloy dots with $t = 15$ nm and diameter of 340 nm showing the motion of a vortex as a function of an in-plane field. (From [52].) (b) Magnetization vector plots obtained from two-dimensional numerical micromagnetic calculations using the NIST OOMMF code for circular Co dots 400 nm in diameter and 50 nm in thickness. (c) MFM images showing the reversal for epitaxial Co dots 10 nm thick and 500 nm in diameter measured with the external field applied in plane.

the single-domain state upon lowering the saturation field led to the reversible formation of a double-vortex structure [63] before an irreversible transition to the single-vortex state occurred, with the vortex motion shown in figure 9(a). In the initial double-vortex structure, the vortices are described as partially open with opposite chirality and appear at opposite positions along the edges.

(c) *Phase boundary and energy considerations.* From the Kerr hysteresis loop measurements (figure 7), an experimental phase boundary between the vortex and the single-domain state has been deduced as a function of dot thickness and diameter. For larger dot thicknesses and diameters, the vortex state is stable, while a transition to the single-domain state occurs upon decreasing the thickness and diameter. This transition is explained simply by the dominant energy contributions in the two configurations. The flux-closure vortex structure minimizes the demagnetization field energy and is dominated by exchange energy. In contrast, the single-domain configuration is dominated by demagnetization field energy with negligible exchange energy. Upon decreasing the diameter, for example, at constant thickness, the exchange energy of the vortex structure becomes increasingly comparable to the magnetostatic energy of the single-domain state. Consequently, below a critical diameter the circular magnetization mode can no longer be maintained and the single-domain state becomes energetically more favourable. This transition is demonstrated in the calculation of the total energy density of circular dots shown in figure 11. Similar arguments apply when reducing the film thickness with a constant diameter. In addition, Cowburn *et al* [60] have compared the experimental phase diagram with the one calculated using micromagnetic simulations and found them in good agreement.

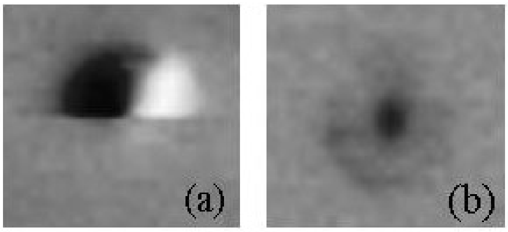

**Figure 10.** The influence of the MFM tip on the single-domain pattern of epitaxial Co(0001) dots. By decreasing the lift scan height from (a) 100 nm to (b) 50 nm, the metastable single-domain state transforms into the vortex state, which is the ground state of the system (thickness of 20 nm, diameter of 200 nm).

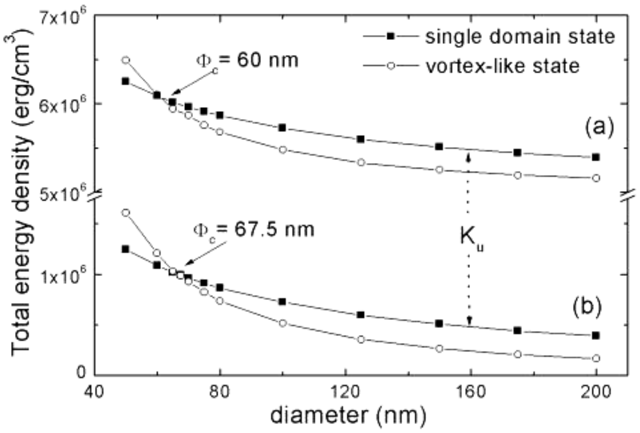

**Figure 11.** Total energy density of the vortex (open circles) and single-domain states (full squares) as a function of the dot diameter obtained from three-dimensional numerical micro-magnetic calculations for circular Co dots of $t = 5$ nm and having (a) perpendicular uniaxial anisotropy and (b) zero anisotropy.

Another interesting aspect concerns the coexistence of magnetic states. In the MFM measurements performed on the Co(0001) dots [50], the single-domain and vortex states are observed simultaneously, but with a larger probability of single domains existing after in-plane saturation. However, those single-domain states are found to be metastable (in agreement with micromagnetic calculations and the phase diagram in figure 9(c) which predict a vortex structure as the stable state). In fact, as shown in figure 10 for a Co(0001) dot 200 nm in diameter and 20 nm thick, small perturbations (such as the stray field from the MFM tip) can induce a transition into the vortex-like state. This type of transition will be discussed further in section 3.4.

(d) *Stability of the vortex state in circular dots.* Various authors have performed MFM or Lorentz microscopy on systems with perpendicular magnetic anisotropy [50] or zero anisotropy [51, 52, 62, 63]. It is interesting to note that similar observations on the presence of the vortex state have been made. The recent experiments performed on soft NiFe dots [52]—figure 9(a), soft Co dots [70]—figure 9(c)—and epitaxial Co(0001) dots with large magnetic anisotropy perpendicular to the dot base [50]—figure 6—are a perfect illustration. This raises questions about what the actual role of the perpendicular uniaxial anisotropy in the epitaxial Co(0001) dots is concerning the formation and stability of the vortex state, supposing that such an anisotropy may favour the presence of vortices or stabilize the vortex state.

In order to investigate the role of perpendicular magnetic anisotropy, three-dimensional numerical micromagnetic calculations were performed [72]. Two cases were compared, Co dots with strong perpendicular magnetic anisotropy and those having zero magnetocrystalline anisotropy. Using different starting configurations, the system relaxed either into a single-domain state (figure 6(c)) or a vortex-like state (figure 6(d)). For thicknesses ranging between 5 and 20 nm or for dot diameters between 60 and 200 nm, the vortex-like state was found to be the lowest energy state. The dependence of the total energy density on the diameter of the dots is shown in figure 11 with very similar behaviour observed in both cases. However, the total energy density of the single-domain and vortex dots with strong perpendicular magnetic anisotropy is shifted upwards by an amount equal to the magnetic anisotropy energy $K_u$. This shift is due to the fact that most spins are in plane and hence point in a hard direction of the magnetic anisotropy.

From figure 11, it can be seen that the presence of strong perpendicular magnetic anisotropy does not influence the ground state configuration very much, nor the transition from the vortex state towards the single-domain state. It does, however, affect the onset of this transition—the critical diameter for Co(0001) dots with strong perpendicular magnetic anisotropy is 60 nm whereas it is 67.5 nm for dots with no anisotropy. This weak dependence on the perpendicular magnetic anisotropy is related to the fact that the thickness range investigated here corresponds to the one for which the continuous epitaxial Co(0001) films are in-plane magnetized ($Q = 0.4$)—see figure 5, region III. Thus, thin Co(0001) dots with a thickness below 20 nm behave like in-plane isotropic elements and the transition from the vortex state to the single-domain state is determined by the same energy considerations as for dots with zero magnetic anisotropy (a pure balance between demagnetization shape energy and exchange energy). However, the presence of the perpendicular magnetic anisotropy lowers the total energy density of the magnetization inside the vortex core slightly, since the spins inside the vortex point along the magnetocrystalline easy axis, thus lowering their anisotropy energy. Close to the critical diameter of 60 nm (for a dot thickness of 5 nm), this gain in energy is most pronounced, since the relative volume fraction of the vortex is large (vortex diameter of 30 nm [72, 73]). This stabilizes the vortex state at smaller diameters and as a consequence the critical diameter for the transition into a single-domain state is pushed to lower values as compared to dots with zero magnetic anisotropy (figure 11).

It is noted that the critical diameter $\Phi_c$ calculated for Co dots ($\Phi_c = 60$–$67.5$ nm for $t = 5$ nm) is in good agreement with the values given in the phase diagram of figure 7 when scaled with the magnetization. Due to the larger saturation magnetization in Co (1400 emu cm$^{-3}$ as compared with 800 emu cm$^{-3}$ for NiFeMo [60]), the critical diameter of Co dots is pushed lower than the corresponding critical diameters reported for NiFeMo (approximately 150 nm for $t = 5$ nm).

(e) *Configurational anisotropy in mesoscopic ferromagnets.* This brief review of sub-micron dots would not be complete without discussing the effect of configurational anisotropy [74]. This type of anisotropy, first proposed theoretically in 1988 by Schabes and Bertram for the case of magnetic cubes, finds its origin in the fact that sharp edges in constrained nanostructures induce deviations from the uniform magnetization, deviations that are dependent on the direction of the magnetic moment with respect to the axis of the nanostructures. The first experimental evidence was reported by Cowburn *et al* [58] on squares of permalloy. Their system of monodomain squares is ideal since they do not exhibit any in-plane demagnetization shape anisotropy, thus making the observation of

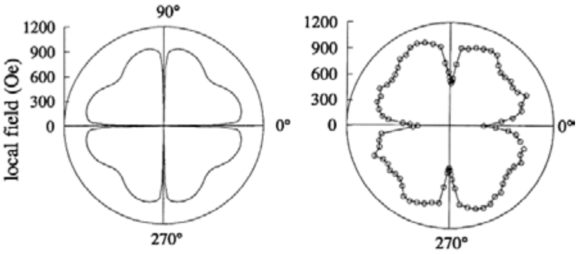

**Figure 12.** Left: polar plot of the effective field (internal anisotropy field plus 660 Oe of an external field) of NiFeMo square elements as a function of the applied field direction. Right: simulation using numerical micromagnetics. (From [58].)

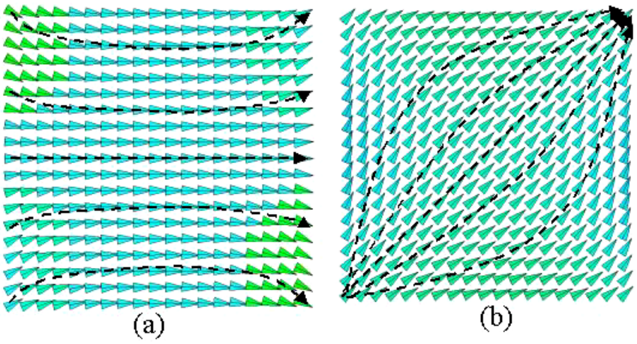

**Figure 13.** Magnetization vector plot showing (a) the lower energy state and (b) the leaf state for a square permalloy element with a thickness of 5 nm and side length of 95 nm. The dotted black curves indicate the demagnetization field curves. The vector plots were obtained from three-dimensional numerical micromagnetic simulations after saturation (a) parallel to the edges and (b) at an angle of 45° from the edges.

any other type of anisotropy easier. The results of Cowburn *et al* [58] are illustrated in figure 12 for a 15 nm thick permalloy square with a side length of 150 nm. The polar plot of the effective field reveals a fourfold anisotropy with an abrupt minimum in the internal anisotropy field whenever the magnetization is parallel to one of the edges of the square. The strength of this configurational fourfold anisotropy field deduced from the polar plot has been found to be extremely strong, about 360 Oe [58].

Although the energy of a perfect, uniformly magnetized square is independent of the in-plane magnetization direction, energy differences do arise when taking into account the non-uniformity of the magnetization distribution at the edges. The non-uniformities lead to magnetization patterns shown in figure 13 (derived from three-dimensional micromagnetic calculations) and depend on whether the sample is magnetized with the external field parallel to the edges (lower energy state) or at an angle of 45° from the edges (yielding the leaf state). Since these two magnetic configurations differ in energy [58], the measured anisotropy energy must be related to the energy difference of the two magnetic configurations and, therefore, to the geometric shape of the structure. This is confirmed by numerical micromagnetic calculation (figure 12). This anisotropy should be more difficult to observe in structures like circles or ellipses where the magnetization is more uniform.

### *3.4. Domains in circular rings*

*3.4.1. Linear versus circular magnetization orientations.* In all reported magnetic random access memory (MRAM[14]) designs to date, the magnetization in the active device is primarily controlled by the shape of the element, e.g. rectangles or ellipses. For this type of memory element, it is well known that non-repeatable switching is caused by the presence of edge domains [3, 75, 76]. To overcome this irreproducibility, several groups have proposed tapering the ends of the magnetic element [75, 77–80]. For elements with a linear magnetization orientation, the sharpness of the tapered ends is critically important to the repeatability of the switching field [3, 76, 80, 81]. Geometric variations of the ends from element to element can yield significant variations in the magnetic switching, and effectively reduce the margin of error for memory element addressing [80].

Alternatively, instead of having a linear magnetization in the memory element, the magnetization orientation can be circular (or closed flux) as discussed in section 3.3.3 (a), thus eliminating the problems associated with end effects. In order to form this mode, the memory element can be either a ring or a circular dot. As discussed in section 3.3.1, the circular magnetization configuration in circular dots can only be maintained above a critical diameter (figure 7). Below this critical diameter, the single-domain state is the lower energy state. One way to stabilize the circular magnetization mode in smaller diameters is to eliminate the central vortex that contains the dominant energy contribution (from exchange energy) of the flux-closure configuration. For these ring-shaped elements, the flux-closure structure results in significantly lower energy than that of a circular dot with the same outer diameter. It is clear, therefore, that upon reducing the outer diameter of the rings, the transition into a single-domain state is suppressed to lower values than for the circular structure. As shown previously in section 3.3.3, the flux-closure state of a circular dot 5 nm thick is the lower energy state only above a critical diameter of 60 nm. In contrast, the flux closure state for the ring geometry is the lower energy state well below outer diameters of 60 nm. However, the latter can only be considered correct as long as the inner diameter is larger than the diameter of the central vortex (30 nm for Co [72]) in circular discs. Furthermore, the introduction of the inner edge reinforces the circular magnetization configuration. Recently, a vertical magnetic random access memory (VMRAM) design was proposed based on a ring-shaped magnetic multilayer stack [80, 81].

*3.4.2. Magnetization configurations and stability in sub-micron rings.* The stability range of the flux-closure structure of polycrystalline Co rings as a function of film thickness and ring diameter using MFM images and micromagnetic simulations has been studied recently [82]. The thickness of the investigated rings ranged between 10 and 50 nm; the outer ring diameter was varied between 300 and 800 nm and the inner ring diameter was varied between 100 and 300 nm.

In contrast to the case of circular dots discussed previously, the flux-closure state is the lowest energy state for all dimensions of rings investigated. However, a metastable single-domain state at zero field can be induced after saturation with an in-plane applied field. The probability of trapping this single-domain state increases for decreasing film thickness and increasing outer diameter. Figure 14 identifies the MFM images[15] and the corresponding micromagnetic configurations of the single-domain and flux-closure structures, respectively. The strong black and white contrast in figure 14(a) corresponds to the single-domain structure whereas the weaker alternating contrast shown in figure 14(b) corresponds to the flux-closure

---

[14] Non-volatile memory devices based on magnetic materials.

[15] In order to make the flux-closure configuration visible in the MFM imaging, all rings were patterned in an octagonal rather than a circular shape.

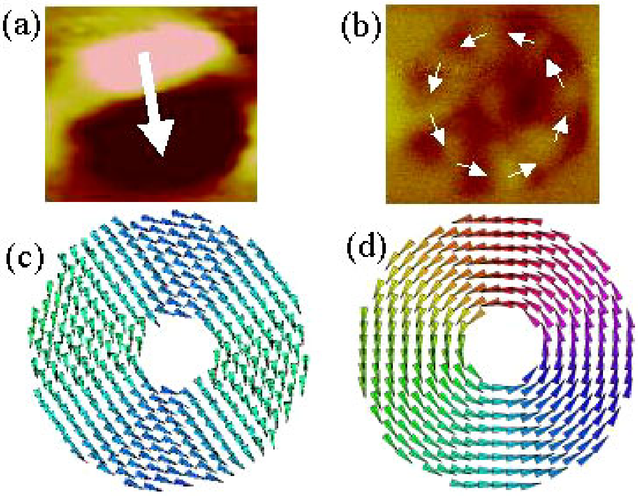

**Figure 14.** MFM contrast of octagonal polycrystalline Co rings (outer diameter 800 nm, inner diameter 400 nm and thickness 20 nm) denoting (a) a single-domain state and (b) a flux-closure configuration. (c) and (d) are magnetization vector plots of circular ring elements (outer diameter 200 nm, inner diameter 50 nm, and thickness 5 nm) calculated using a three-dimensional micromagnetic code.

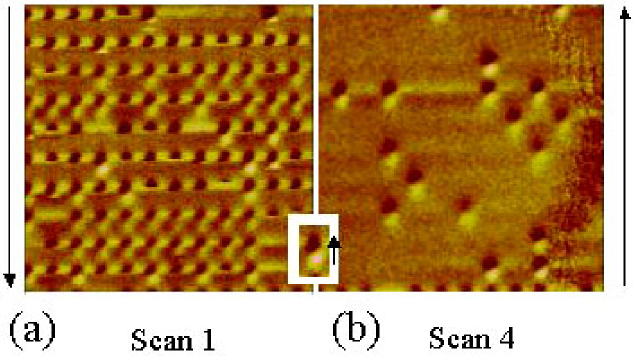

**Figure 15.** Repeated MFM scans of the same area (20 × 20 $\mu$m$^2$) at zero field after in-plane saturation for polycrystalline Co rings with a thickness of 20 nm and outer diameter of 800 nm. The images are (a) the first scan from top to bottom and (b) the fourth scan from bottom to top. For a certain number of rings only the upper black part of the single-domain state is seen, revealing that the tip–sample interaction switches the rings into the flux-closure state when positioned above the centre of the ring.

state. Figures 14(c) and (d) give the corresponding magnetization-vector plots obtained from three-dimensional numerical calculations.

*3.4.3. Metastable states observed using the MFM tip effect.* The metastability of the in-plane remnant single-domain state is demonstrated in figure 15, where repeated zero-field MFM scans over the same area of rings are shown. The scan height is held at a large distance of 150 nm, which still allows one to visualize the strong dipolar contrast of the single-domain state, but not the much weaker contrast of the flux-closure state. In figure 15(a), almost all

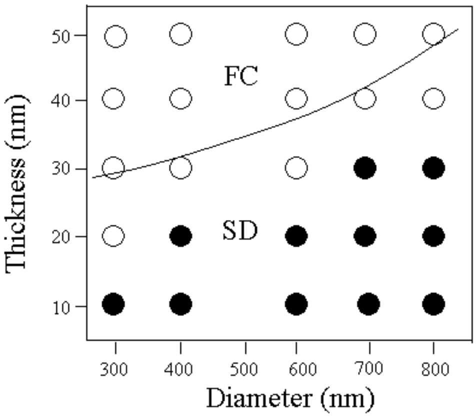

**Figure 16.** The experimentally determined ‘phase diagram’ of the metastable single-domain state (solid circles) and the flux-closure state (open circles) as a function of thickness and outer diameter for polycrystalline Co rings obtained from Kerr-effect hysteresis loop measurements. The solid curve represents the calculated boundary [82].

rings (96%) are in a single-domain state before the MFM tip is scanned for the first time (from top to bottom). The tip field appears to be strong enough to switch the rings during the scan, as can be seen by the fact that for many rings only the upper black half is visible. Repeating the scan a second time (from bottom to top), only 25% of the rings are left in the single-domain state, with more rings switching into the flux-closure state during the scan. After the fourth scan, only 14% of the rings are left in the single-domain state (figure 15(b)). However, the reversal of the dots from the single-domain into the flux-closure state is not a relaxation effect. Changing the scan area, after having ‘erased’ most of the single-domain states in one area by repeated scanning, again shows the high remnance single-domain state.

From Kerr magnetometry performed on all of the ring arrays, it was found that the probability of the presence of the metastable single-domain state at zero field depends on both the film thickness and the outer ring diameter. This is summarized in the qualitative phase diagram of figure 16. Micromagnetic calculations indicate that for increasing diameter, the energy of the single domain and flux-closure states decrease, but at different rates so that the energy difference between them also decreases. Therefore, the probability for trapping the single-domain state in a local energy minimum increases.

*3.4.4. Reversal processes in rings.* Although the in-plane remnant state can be the single-domain state, the reversal of all the rings investigated takes place via the transformation of the saturation single-domain state into the flux-closure structure. From there, the ring can transform into the reversed single-domain state under a reverse bias field. This process is illustrated in figure 17 on an array of rings having a large remnance at zero field (as deduced from Kerr hysteresis-loops). To minimize the tip–sample interaction, a lift scan height of 200 nm was used. Therefore, the actual field value at each ring is the sum of the applied field and the tip field. Starting from the remnant state at 0 Oe (induced in the absence of the tip), a large number of rings switch from the single-domain into the flux-closure state due to the tip field (figure 15). However, after several scans a number of rings stabilize and a −100 Oe field is required to switch all the rings from the single-domain state into the flux-closure state (figure 17). This means that the reversal occurs through the formation of a flux-closure configuration. Upon increasing the reversed field value to −450 Oe (the maximum field of the

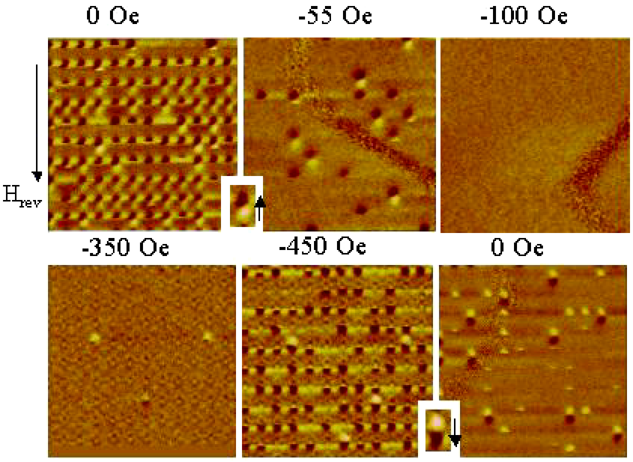

**Figure 17.** MFM images of a 20 × 20 $\mu$m$^2$ area for polycrystalline Co rings 20 nm thick and 800 nm in outer diameter as a function of applied field, where the field that the images were scanned in is indicated at the top of each image. The arrow to the left indicates the reverse field direction $H_{rev}$ (negative).

magnet), 70% of the rings are in the reversed single-domain state. Reducing the field back to zero, only 25% of the rings were in the remnant state as compared to 96% initially. This is due to the fact that the initial remnant state was obtained in the absence of the tip field, while the remnant state at the end of the hysteresis cycle is obtained in the presence of the tip field, resulting in a small additional field applied to the rings.

### *3.5. Domains in wires*

Most of the pioneering work was carried out on elongated particles [83–86] since they act as a model system for the nucleation–propagation reversal process. From these studies, basic micromagnetic information such as the nucleation volume can be derived [83, 85]. Moreover, due to the high aspect ratio (length to lateral cross-section), the magnetization direction can be well controlled by both shape and magnetic anisotropy. In the following, rectangular epitaxial cobalt wires[16] are considered where the in-plane uniaxial anisotropy is oriented either perpendicular (section 3.5.1) or parallel (section 3.5.2) to the long wire axis.

#### *3.5.1. Crystal anisotropy field perpendicular to the wire axis.*

(a) *Single-domain to stripe-domain transformation.* The flat rectangular Co wires are characterized by a strong uniaxial magnetocrystalline anisotropy ($K_u = 6 \times 10^6$ erg cm$^{-3}$) oriented in plane and perpendicular to the wire axis. This magnetocrystalline anisotropy is in competition with the demagnetization shape anisotropy, which in turn favours

---

[16] These wires were prepared from epitaxial Co(1010) thin films of thickness 30, 40, 50, 60 and 80 nm. The films were grown under ultrahigh vacuum conditions on (110) MgO substrates by molecular beam epitaxy using a Mo–Cr buffer layer. Structural investigations confirm that they are hcp and magnetic investigations confirm a strong in-plane uniaxial anisotropy [87]. The films were patterned using electron-beam lithography, lift-off techniques and ion beam etching. For each thickness ($t$), wire arrays were prepared with widths ($w$) of 100, 150, 200, 500, 800 and 1000 nm. The wires were 10 $\mu$m long and the separation between the wires was 5 $\mu$m, sufficient to neglect any dipolar interaction. For each set of ($t$, $w$)-values, the wires were patterned with the long wire axis aligned either perpendicular or parallel to the magnetocrystalline anisotropy axis.

an alignment of the magnetization parallel to the wire axis. A reduction of this demagnetization energy can be achieved by the formation of a periodic stripe domain pattern, analogous with the stripe domains in continuous perpendicular Co(0001) films (section 3.2). In addition, the stripe domain width can be controlled by the wire thickness and the wire width. However, in contrast to the continuous films, which can be described by a thickness-independent, constant $Q$-factor $Q_0 = K_u = 4\pi M_s$ (=0.4 for Co), only an effective $Q$-factor $Q_{eff}$ can be defined for the wires, since it varies as a function of system size $(t, w)$. This is because, in contrast to the continuous film (with $N_{eff} = 1$), the effective demagnetization factor $N_{eff}$ inside the wires depends on the film thickness $t$ and wire width $w$ according to the following:

$$N_{eff} = \left(\frac{2}{\pi}\right) \arctan\left(\frac{t}{w}\right). \tag{19}$$

This varies between 0 (for $t \to 0$ or $w \to \infty$) and 1 (for $w \to 0$ or $t \to \infty$), yielding an effective $Q$-factor $Q_{eff} = Q_0/N_{eff}$, which can vary between the value of the continuous film and infinity. For the continuous films, different types of stripe-domain structure have been described depending on the value of $Q$ [88]; open or strong stripes have $Q > 1$ and flux-closed or weak stripes have $Q < 1$. So, for wires, different domain configurations are expected [89] to be stable for different wire dimensions $(t, w)$. A phase diagram is shown in figure 18, which takes into account four possible magnetization configurations.

(i) The transverse single-domain state ($\boldsymbol{M}$ perpendicular to the wire axis).
(ii) The longitudinal single-domain state ($\boldsymbol{M}$ parallel to the wire axis).
(iii) The open stripe structure.
(iv) The flux-closure stripe structure.

The boundaries between the different configurations (dotted curves in figure 18) were calculated from a domain theory model based on Kittel's formulation [29].

In order to be able to compare this predicted phase diagram to the experimental data, one first has to define the procedure by which the magnetic system can relax into its ground state. It has already been mentioned for dots and rings (sections 3.3 and 3.4) that, depending on the magnetic history, the induced configuration might be a metastable state. For instance, as shown in figure 19, a transverse single-domain state is induced when magnetizing along the crystal anisotropy direction (in plane and perpendicular to the wires). However, a stripe-domain pattern is induced when magnetizing along any other direction. Furthermore, the stable ground state is induced after hard axis demagnetization procedures (labelled $D\|s$ and $D\perp$ in figure 19). Typical MFM images of stable single-domain and stripe-domain states are shown in figure 18 for different values of $t$ at constant $w$ as well as the stable single-domain and stripe-domain configurations.

For decreasing film thickness and increasing wire width, the transverse single-domain state stabilizes because the gain in demagnetization energy (from nucleation of the stripe-domain state) decreases. For some critical values the gain will not be sufficient to compensate for the wall energy causing the system to acquire a transverse single-domain state. The bold line in the $(t, w)$-diagram of figure 18 summarizes the experimental boundary between the stable stripe-domain state and the stable transverse single-domain state. The discrepancy between the calculation and the experiments is due to the fact that the Co bulk value for the domain wall energy (12 erg cm$^{-2}$) was taken as constant in the calculation. However, due to the vertical and lateral confinement, the wall energy in the wires should be much larger [87].

(b) *Metastability of the observed magnetic structures.* As already discussed, metastable states can be induced depending on the magnetic history. For instance, most of the wires

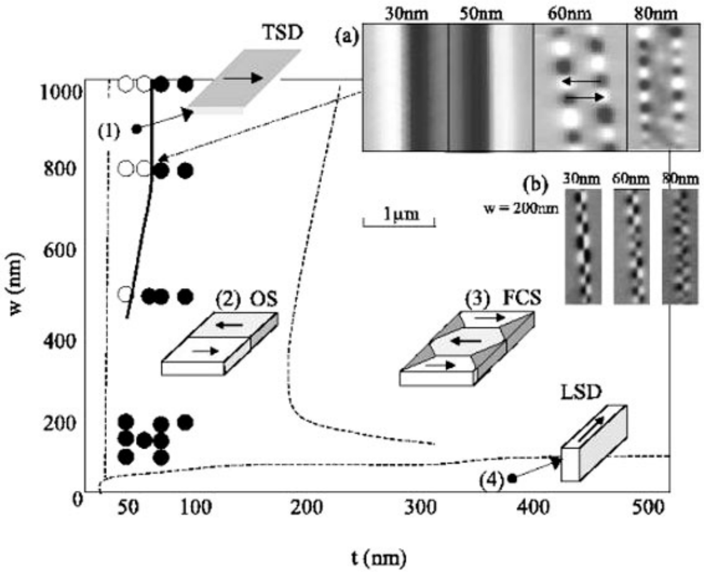

**Figure 18.** Qualitative phase diagram ($t$, $w$) of the ground state domain configurations of epitaxial Co(1010) wires with uniaxial magnetocrystalline anisotropy aligned perpendicular to the long wire axis. The dotted curves are calculated boundaries while the bold line is the experimental boundary between the transverse single-domain (open circles) and the open stripe-domain state (filled circles). Inset (a) MFM images for wires of width 800 nm showing the evolution of the ground state with thickness. Inset (b) MFM images for wires of width 200 nm showing the thickness dependence of the domain period.

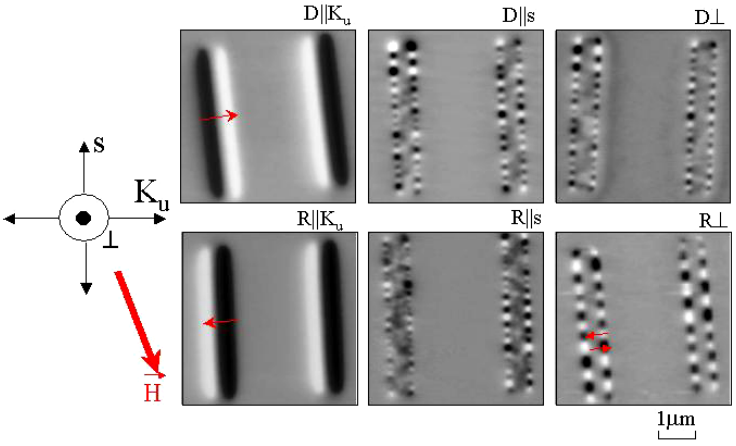

**Figure 19.** MFM images for a Co(1010) wire 800 nm wide and 60 nm thick obtained after different magnetization histories. $D$ denotes a demagnetized state; $R$ denotes a remnant state; $K_u$ is the easy axis direction; $s$ is the direction of the long wire axis; ⊥ denotes the application of the magnetic field perpendicular to the film plane.

investigated show a transverse single-domain state as the remnant state, when saturated along the direction of the crystal anisotropy field (in plane and perpendicular to the wire axis). This single-domain state is the stable state only for those dimensions reported in the phase diagram as open circles. For all others, this state is metastable and is

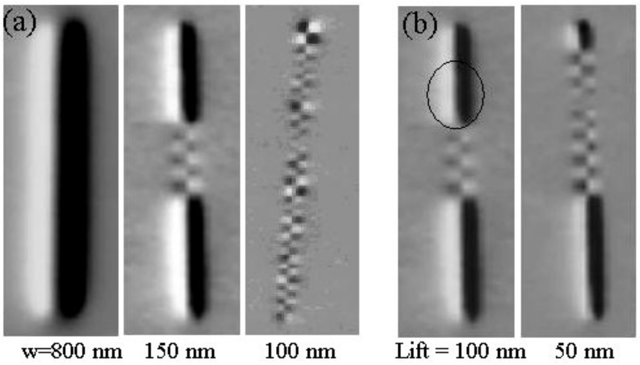

**Figure 20.** MFM images taken on Co(1010) wires after in-plane, easy-axis saturation and at a lift scan height of 100 nm for wires 60 nm thick with widths of 800, 150 and 100 nm. (b) Upon decreasing the lift scan height from 100 to 50 nm (left image) the number of the stripe domains in a 150 nm wide wire is increased (right image), corresponding to an irreversible switch of the magnetization.

induced because the applied field parallel to the easy magnetocrystalline anisotropy axis gives a preferential orientation to the magnetization $\boldsymbol{M}$, stopping $\boldsymbol{M}$ in a local energy minimum. As this barrier between the single-domain state and the multi-domain stripe state decreases, the wires become narrower and thicker due to the increase in the in-plane shape demagnetization fields (scaling with $t/w$) which favours the nucleation of reversed domains. This dependence is confirmed in figure 20(a) for which the remnant state after saturation along the direction of the crystal anisotropy direction (in plane and perpendicular to the wire axis) is shown. For $w = 800$ nm a pure transverse single-domain state is stabilized, while for $w = 150$ nm the stripe-domain and transverse single-domain state coexist and for $w = 100$ nm a complete stripe structure is induced.

The stability or metastability of the single-domain state described above can be experimentally verified by applying a small perturbation to the domain structure. This can be done using the stray field of the MFM tip. As shown in the left MFM image of figure 20(b), the single-domain and the stripe-domain state coexist at zero field for a narrow wire of 150 nm. Upon lowering the lift scan height from 100 to 50 nm when scanning the MFM tip over the wire, the enhanced stray field from the MFM tip produces an irreversible transition from the single-domain into the stripe-domain state in some regions.

*3.5.2. Crystal anisotropy field parallel to the wire axis.* In this section, the cobalt wires are characterized by a magnetocrystalline uniaxial anisotropy that co-operates with the shape anisotropy to maintain the magnetization parallel to the wire axis. Two cases are considered, one with wires[17] having a rectangular cross-section 100 nm on a side and the other with cylindrical wires[18] having circular cross-sections ranging from 30 to 50 nm. These wires proved to adopt a rather good quality hexagonal compact structure with a preferential texture along the wire axis [92].

In both cases, the magnetic ground state is the single-domain structure. The magnetization reversal in a parallel field of such Co wires can, to a certain extent, be simulated by coherent (or unison) rotation of spins [3, 68, 69, 83, 93]. In this model, a single giant magnetic moment is

---

[17] These wires were prepared from epitaxial Co(1010) thin films by electron beam lithography.

[18] These wires are prepared by electrodepositing Co into the pores of high quality track-etched polycarbonate membranes [90–92].

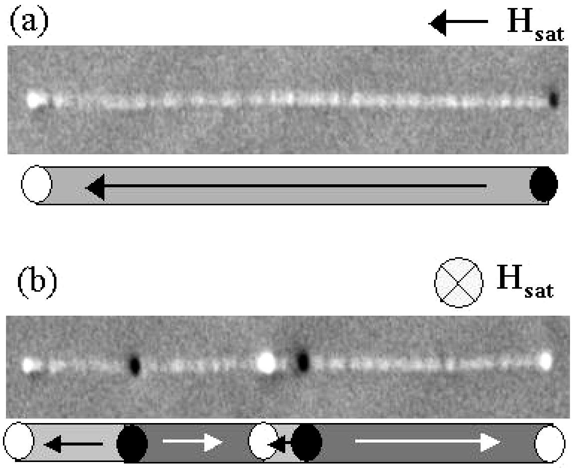

**Figure 21.** Zero-field MFM images of a 35 nm cylindrical Co wire after saturation in a field (a) parallel to the wire axis and (b) perpendicular to the wire axis.

subjected to not only the external field, but also to a first order uniaxial anisotropy of constant value $K_u$, the direction of which is parallel to the wire axis. Micromagnetic theory predicts that in these structures, two other types of nucleation (and reversal) mechanism besides coherent rotation can occur: buckling and curling [3, 93–95]. All these reversal modes should result in a square hysteresis loop when the field is applied parallel to the axis of the wire [83, 85]. Hence, only two magnetization states, parallel and antiparallel to the wire axis, are possible in this type of wire. This is confirmed by MFM imaging, as shown in figure 21(a), for a cylindrical Co wire 35 nm in diameter, after application of a large field parallel to the wire axis [96]. The dark and bright contrasts at the wire extremities correspond to 'magnetic charge' distributions at the end faces, which arise when the magnetization is in a single-domain state and aligned parallel to the wire axis.

In contrast to the saturation along the wire axis, a multi-domain state with head-to-head domain walls can be induced by saturation in a field perpendicular to the wire axis, as shown in figure 21(b). Upon reduction of the field from perpendicular saturation to zero, the magnetization may rotate clockwise or anti-clockwise towards the wire axis, resulting in this multi-domain structure.

(a) *Wall structures.* The dark and bright contrasts visible along the wire axis in figure 21(b) arise from the strong accumulation of 'magnetic poles' at the domain wall between two longitudinally magnetized domains of opposite magnetization directions. In bulk materials and continuous films with in-plane uniaxial anisotropy, domains of opposite magnetization orientation are usually separated by 180° domain walls that are parallel to the magnetization inside the domains. This orientation arises in order to avoid net 'magnetic poles' on the walls according to the pole avoidance principle. In contrast, the lateral confinement of the magnetization in small diameter nanowires with parallel-to-wire anisotropy forces the domains to meet head on and the separating walls to orient perpendicular to the wire axis, therefore forming domains. This results in heavily charged walls having both volume and surface-pole distributions, exhibiting the strong MFM contrast shown in figure 21(b).

As sketched in figure 22, a simple one-dimensional model for the domain wall structure can be assumed in which the spins within the wall rotate perpendicular to the wire

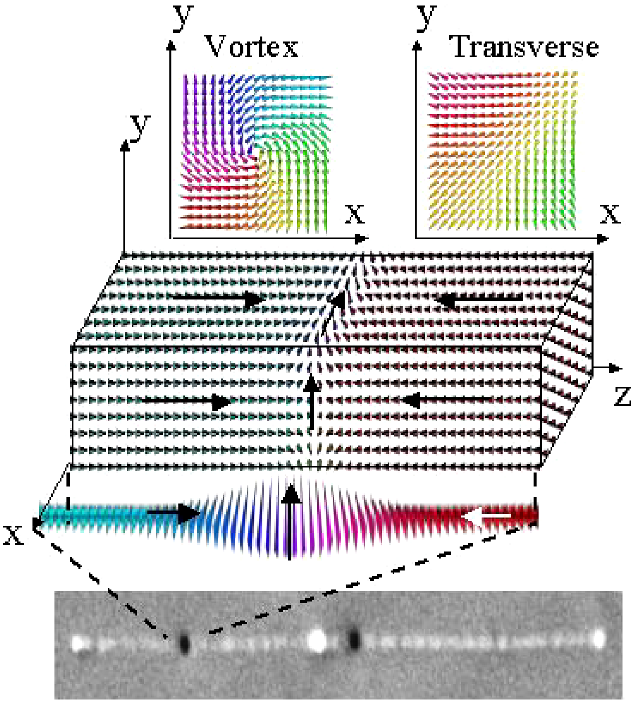

**Figure 22.** Bottom: MFM image of the domain wall contrast along an electrodeposited Co nanowire. Above the MFM image, a one-dimensional wall profile is shown where the magnetization is averaged over the wire cross-section. In this one-dimensional model the wall spins are perpendicular to the wire axis. Above the one-dimensional profile, the magnetization vector distribution calculated from three-dimensional numerical micromagnetic simulations is shown for a wire with square cross-section. Top: magnetization vector plot showing the magnetization distribution across the square cross-section at the wall centre ($z = 0$). Two modes can be stabilized, a vortex mode and a transverse mode.

axis. One question to address is the precise configuration of the magnetization inside the wall. Three-dimensional numerical micromagnetic calculations reveal two different wall magnetization modes for square wires (figure 22). These modes are very similar to the single-domain state and vortex state of circular dots shown in figure 6. Correspondingly, they are called the transverse and the vortex-type wall. In the transverse wall, the magnetization is almost uniform across the diameter and all spins are perpendicular to the wire axis, giving rise to a transverse demagnetization field. In contrast, in the vortex wall, the magnetization forms a circular magnetization path, where the wall spins try to stay parallel to the wire surface thereby reducing the magnetostatic energy. Similar to the circular dots, the total energy density of the two wall-magnetization modes depends on the diameter of the wires and a critical diameter exists below which the transverse wall is lower in energy (compare to figure 11 for circular dots). Using the Co parameters, this critical diameter is approximately 20 nm. It is interesting to note that recent numerical studies based on time quantified Monte Carlo methods have yielded similar wall-magnetization modes that are nucleated in nanowires during the magnetization reversal. Furthermore, it should be remembered that these configurations represent a theoretical solution, which does not take into account the defect structure of the real wires (variations in diameter, grain

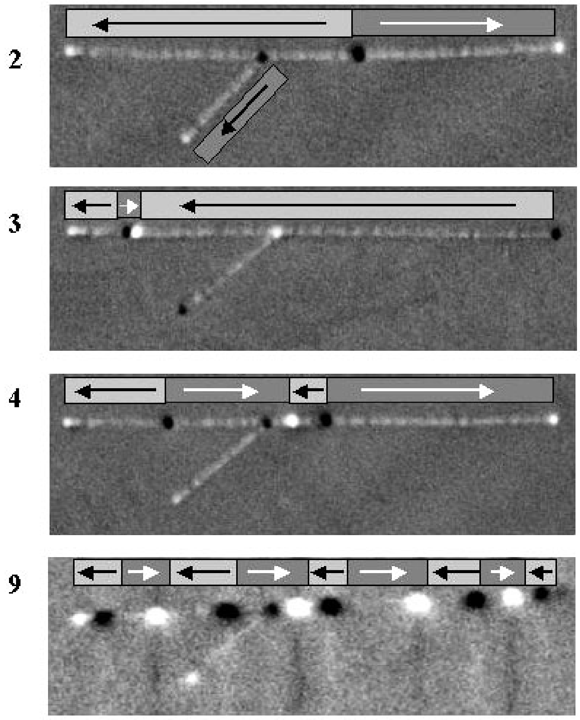

**Figure 23.** MFM images of a 35 nm electrodeposited Co wire, after saturation in a field perpendicular to the wire axis. Repeated saturation may lead to a different number of domains. Attached to the horizontally aligned wire, a second, smaller wire inclined at 45° is seen.

boundaries etc) where the walls can be pinned and which can modify the configuration shown above. Finally, it will be difficult to differentiate by MFM these two configurations, since the contrast will be dominated by the strong ‘magnetic poles,’ which will be very similar in both cases.

(b) *Pinning sites and reversal procedure.* It is observed that for the circular electrodeposited Co nanowires the number of domain walls induced in a single wire after perpendicular saturation (or demagnetization) can vary from one experiment to the next. For instance, two, three, four or even nine longitudinally magnetized domains of alternating magnetization directions were induced on a single wire (figure 23). This variation in number probably arises from the fact that the exact field orientation varies slightly from one experiment to the next, with the field being slightly more or less inclined towards the wire axis. However, it is also observed that some walls occur at the same position along the wire, suggesting that they are stabilized at pinning sites. Consequently, in order to move the walls along the wire axis, a finite de-pinning field (applied parallel to the wire axis) is required. This is demonstrated in the image sequence of figure 24 where weak and strong pinning sites are observed.

The number of pinning sites and their respective pinning strengths will depend on the crystalline quality of the wires. From TEM investigations of the electrodeposited wires it is known that the wires contain many stacking faults [91] and grains micrometres in size. For those wires, a fairly large number of walls can be induced (up to ten along a wire of 10 $\mu$m). In contrast, for the rectangular, 100 nm wide epitaxial Co(1010) wires, it is very

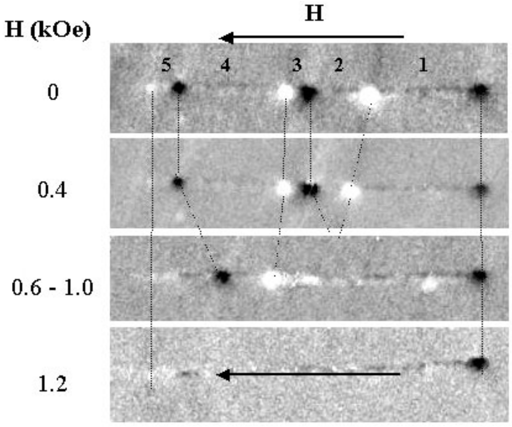

**Figure 24.** MFM images of a 35 nm electrodeposited Co wire. The top image shows the wire in zero field after out-of-plane saturation. For the remaining images, a field was applied parallel to the wire axis, with field values noted to the left.

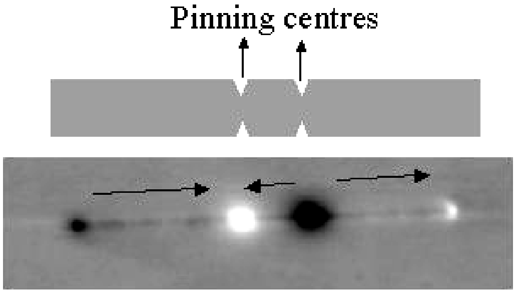

**Figure 25.** MFM image taken of a rectangular epitaxial Co(1010) wire, patterned by electron beam lithography. In order to induce pinning sites, constrictions were defined along the wire axis as shown in the schematic diagram at the top.

difficult to induce a large number of walls in a perpendicular remnant state, unless a local constriction is artificially induced, as in figure 25.

## 4. Size and temperature effects in confined magnetic structures

The next step after examining the domain structures present in confined magnetic structures is to examine how size and temperature affect the response of a magnetic material to an applied field. Simply applying a magnetic field will obviously reorient the magnetization, if the field is strong enough. However, if the sample is cooled or the size is drastically reduced, then new phenomena emerge—superparamagnetism and macroscopic quantum tunnelling (MQT). Both of these effects involve quantum mechanics—either to tunnel through the barrier, or to impart enough energy so that the particle can be excited over the barrier. More importantly, in order for these phenomena to be observed, the dimensions of a particle must be reduced until it is composed of only one, single domain—a monodomain particle. This is the characteristic length scale that defines this branch of mesomagnetism.

### *4.1. Monodomain particles*

The existence of monodomain particles (particles that, even in the absence of a magnetic field, have all of their atomic magnetic moments aligned) was first proposed by Frenkel and Dorfman [97] in 1930. The size at which it is energetically favourable to form only a single domain, rather than multiple domains, is determined by the balance between the magnetocrystalline anisotropy energy, the exchange energy, the Zeeman energy and the magnetostatic energy (see section 2.2).

In bulk ferromagnets, it is energetically favourable to form domains to decrease the surrounding magnetic field (and hence the magnetostatic energy). Although the average domain size depends upon the size and shape of the particle, it is typically greater than a few microns. Furthermore, the domain wall width $\lambda$ separating the different domains is typically much narrower than the domain size—on the order of 100 times the atomic spacing $a$. The high exchange energy makes any non-uniform rotation of the magnetization on a scale less than $\lambda$ difficult. Therefore, if the diameter of the particle is less than $\lambda$, the particle ought (and has been verified experimentally—most recently by Majetich and Jin [98]) to be monodomain. However, this does not mean that particles larger than $\lambda$ cannot be monodomain—the actual size depends on the energy balance between the magnetostatic energy and the anisotropy energy. (The exchange energy does not come into play since the particles will not have domain walls.) Therefore, any estimation of the critical size of a single-domain particle must take into account the dipole interactions (which generate the magnetostatic energy) between atomic moments of the particles, given by

$$E_{dipole} = 2\pi N_{ik} M_i M_k \tag{20}$$

where $N_{ik}$ is the $ik$th element of the shape demagnetizing tensor given in equation (10), and $M_i$, $M_k$ are the magnetic moments of atoms $i$ and $k$. From this, the maximum value of the diameter allowed for a monodomain particle is determined to be [99]:

$$d_0 = \lambda \left( \frac{E_{anisotropy}}{E_{dipole}} \right)^{1/2} \tag{21}$$

for $E_{anisotropy} \ll E_{dipole}$ (weak crystalline anisotropy) and

$$d_0 = \lambda \left( \frac{E_{anisotropy}}{E_{dipole}} \right) \tag{22}$$

for $E_{anisotropy} \gg E_{dipole}$ (strong crystalline anisotropy). For example, Fe, a material with a weak crystalline anisotropy, has a domain wall width of ~50 nm and a monodomain diameter limit of ~15 nm. MnBi, a material with a strong anisotropy, has a domain wall width of ~10 nm and a maximum monodomain diameter of ~500 nm. Therefore, even particles that are large compared to their domain wall thickness can be monodomain.

With monodomain particles, there are two fundamental modes (see figure 26) for changing their magnetization direction. The first (A) is to thermally excite the magnetization over the energy barrier (see equation (28) and figure 28) separating the two different magnetization states; the second (B) is to tunnel through the same energy barrier. The first mode is referred to as superparamagnetism and the second is called[19] MQT. However, these two modes do not describe the actual process by which the magnetization reversal [100] occurs—it could be coherent rotation (see sections 3.3.3 (b), 3.4.4, 3.5) or an incoherent process like buckling or curling[20]. (For simplicity, it will be assumed that the process is coherent since an incoherent process will generate domain walls, introducing exchange energy and thereby, in general, increasing the energy barrier.)

---

[19] This is sometimes also called quantum tunnelling of the magnetization (QTM).

[20] For further reading, see chapter 3, section 5 of [3].

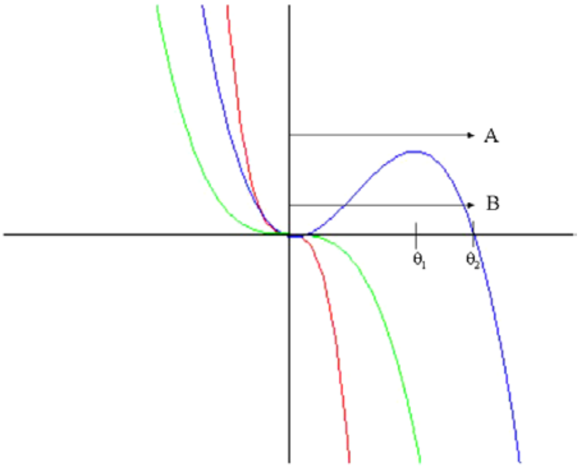

**Figure 26.** Modes of magnetization reversal: (A) superparamagnetism; (B) MQT.

### *4.2. Superparamagnetism*

Classical paramagnetism has been known from statistical mechanics since the turn of the century. Then, in 1949, Néel [101] suggested that if the volume of the particle were small enough, it would be possible for the particle to spontaneously reverse its magnetization, even in the absence of a magnetic field. Although the first clear evidence of this was presented by Heukelom and Reijen [102] in 1954, it was not until 1959 that Bean and Livingston [103] realized that at elevated temperatures, monodomain ferromagnetic particles could behave in a manner identical to that of an atomic moment—like a classical paramagnet. They termed this behaviour 'superparamagnetism' due to the very large moment of the particles[21]. To illustrate this, consider two particles (figure 27): both have a magnetic moment of $\mu$, and both are oriented at an angle of $\theta$ with respect to the applied field. The first particle is isotropic—no crystalline anisotropy—and the second has uniaxial anisotropy. In the first case, there are no additional energy terms from the anisotropy, so the energy of the particle is

$$E = -\mu H \cos\theta. \tag{23}$$

If there is an assembly of these particles at a temperature $T$, then there will be a Boltzmann distribution of angles ($\theta$) over the assembly. Therefore, the total magnetization as a function of field and temperature will yield [104] the familiar Langevin function:

$$N\mu L(x) = N\mu\left(\coth(x) - \frac{1}{x}\right) \tag{24}$$

where $x = \mu H/k_B T$ and $N$ is the total number of particles. This is analogous to a system of classical paramagnets. The only difference is in the value of $\mu$ (see footnote 21).

In reality, monodomain particles are not completely isotropic in their properties. Instead, they will have anisotropic energy contributions to their total energy from shape, crystal structure, imposed stresses etc. (An excellent discussion of nanoparticles and the role of magnetocrystalline anisotropy is given in [105].) Take the second particle as an example. Assume that it has the simplest anisotropy—uniaxial,

$$E_{anisotropy} = K_u V \sin^2\theta \tag{25}$$

---

[21] In atomic paramagnetism the value of the magnetic moment is a few $\mu_B$; in superparamagnetism it may be as large as $10^5$ $\mu_B$.

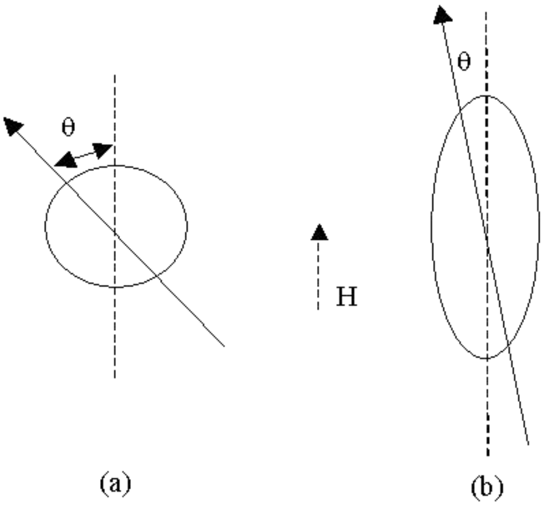

**Figure 27.** (a) Isotropic monodomain particle and (b) monodomain particle with uniaxial anisotropy.

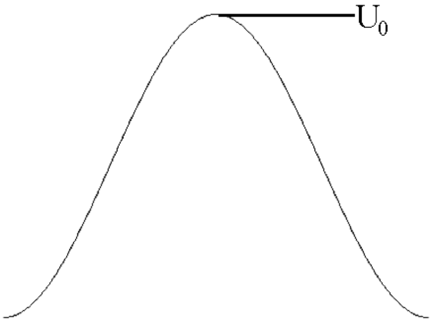

**Figure 28.** Energy barrier of a uniaxial monodomain particle.

where $\theta$ is the angle between the moment and the symmetry axis of the particle, $V$ is the volume of the particle and $K_u$ is the uniaxial anisotropy energy density. If the applied field $H$ is oriented along the symmetry axis, then the particle's energy is

$$E = K_u V \sin^2\theta - \mu H \cos\theta. \tag{26}$$

In the simplest case, all of the particles are aligned with their easy axes parallel to each other. Then the magnetic moment $\mu$ is quantized parallel or anti-parallel to the applied field $H$. The magnetization as a function of field and temperature is given by the special case of the Brillouin function:

$$M = N\mu \tanh\left(\frac{\mu H}{kT}\right). \tag{27}$$

However, if the particles are unaligned, then they will have a Boltzmann distribution of $\theta$ values in thermal equilibrium different from either of the above cases and therefore will no longer obey a simple Langevin function. The energy [99] necessary to overcome the barrier and reverse[22] the particles' magnetization remains $K_u V$. Fortunately, although the functional form may not be known, there are two methods to determine if a material is superparamagnetic: theoretically through the 'blocking temperature' and experimentally from magnetometry measurements.

Theoretically, superparamagnetism is an intimate relationship between measurement timescale, particle diameter and temperature. In order to provide an estimate of the conditions under which superparamagnetism occurs, assume that you have an assembly of particles as in figure 27(b) where the energy is given by equation (25). The energy barrier is shown in figure 28 where the barrier height is

$$U_0 = K_u V. \tag{28}$$

Hysteresis will appear and superparamagnetism will disappear when the particles of a certain size are cooled below $T_B$—the blocking temperature—or the particles' size at a fixed temperature decreases below $D_p$. In order to determine these critical values, the rate at which thermal equilibrium is approached must be considered.

*4.2.1. Case I: no applied field* ($H = 0$). Assume that there is some initial magnetization $M_i$ at time $\tau = 0$—the result of (say) an applied field that is removed at $\tau = 0$. When the field is removed, some particles will immediately reverse their magnetization since they will have enough thermal energy to do so ($k_B T_j \gg k_B T_{avg}$). The rate of decrease at any given time is given by

$$M = M_i \mathrm{e}^{-(U_0/k_B T)} \tag{29}$$

where the exponential is the probability that the particle has enough energy to overcome the energy barrier (given by equation (28)) required for reversal. The rate of decay of the magnetization is given by

$$\frac{-\mathrm{d}M}{\mathrm{d}t} = f_0 M_i \mathrm{e}^{-(U_0/k_B T)} = \frac{M}{\tau_0} \tag{30}$$

where $\tau_0$ is the relaxation time and $f_0$ is the attempt frequency—on the order of $10^9$ Hz—obtained from ferromagnetic resonance (FMR) experiments and slightly field dependent (although that is usually ignored). If you integrate the above equation with respect to time, you get

$$\begin{aligned} \int_{M_i}^{M_r} \frac{-\mathrm{d}M}{M} &= \int_0^t \frac{\mathrm{d}t}{\tau_0} \\ M_r &= M_i \mathrm{e}^{-(t/\tau_0)}. \end{aligned} \tag{31}$$

Therefore, $\tau_0$ is the time is takes to decrease the magnetization to $e^{-1}$ (37%) of $M_i$. If $M_i = M_s$ (the saturation magnetization) then

$$\frac{1}{\tau_0} = f_0 \mathrm{e}^{-(U_0/k_B T)}. \tag{32}$$

This rate comes from the Néel–Brown model of magnetization reversal [101, 107]. The first experimental verification for this was achieved by Wernsdofer *et al* [108]. Hansen *et al* [109] examined the reversal dynamics directly using neutron scattering. Furthermore, equation (32) is very similar to the classical over-barrier transition rate:

$$\Gamma_C = \left(\frac{\omega}{2\pi}\right) \mathrm{e}^{-(U_0/T)} = f_0 \mathrm{e}^{-(U_0/T)} \tag{33}$$

---

[22] It is important to recall at this point that the energy barriers here are based on the assumption of coherent rotation of the magnetization during reversal. It is possible to have incoherent reversal when the process is due to shape anisotropy (like curling) and it lowers the energy barrier [106].

where $\tau_0$ is very strongly volume and temperature dependent. For example, the spherical $\varepsilon$-Co particles ($K \sim 1.5 \times 10^6$ erg cm$^{-3}$) made by Puntes *et al* [40] with a diameter of 10 nm yield $\tau_0$ (300 K) $= 0.17$ s and $\tau_0$ (77 K) $= 1.3 \times 10^{23}$ s; a diameter of 5 nm yields $\tau_0$(300 K) $= 1.1 \times 10^{-8}$ s and $\tau_0$(77 K) $= 1.0 \times 10^{-5}$ s. So, small changes in $\tau_0$ result in *very* small changes in volume. Therefore, we can arbitrarily define the measurement timescale to be $\tau_0 = 100$ s—the time over which the magnetization must be stable in order to measure hysteresis. This results in

$$\frac{K_u V_p}{k_B T} = 25. \tag{34}$$

Therefore, only when the energy barrier

$$U_0 = K_u V_p = 25 k_B T \tag{35}$$

will the magnetization be 'stable' and hysteresis observed. This also means that

$$\begin{aligned} V_p &= \frac{25 k_B T}{K_u} \\ T_B &= \frac{K_u V}{25 k_B}. \end{aligned} \tag{36}$$

So, for Puntes' cobalt at 300 K, $V_p = 6.9 \times 10^{-25}$ m; at 77 K, $V_p = 1.8 \times 10^{-25}$ m. For the 10 nm spheres, $T_B = 228$ K; for the 5 nm spheres, $T_B = 28$ K. So, small changes in diameter have huge effects on the blocking temperature, but changes in the measurement temperature only have small effects on the critical volume.

### 4.2.2. Case II: applied field oriented anti-parallel to magnetic moment.

In an applied field oriented anti-parallel to the magnetic moment, the energy is given by

$$E = K_u V \sin^2\theta + \mu H \cos\theta. \tag{37}$$

Therefore, the energy barrier is

$$U_0 = E_{max} - E_{min} = K_u V \left(1 - \frac{\mu H}{2 K_u V}\right)^2. \tag{38}$$

As can be seen, the barrier is reduced by the application of a field. So, for particles larger than $V_p$ or $T > T_B$, the particles are stable in zero field. The field at which thermally activated reversal can occur in the specified time frame $\tau_0$ is called $H_{ci}$—the induced coercivity.

$$\begin{aligned} U_0 &= K_u V \left(1 - \frac{\mu H_{ci}}{2\,K_u V}\right)^2 = 25\,k_B T \\ H_{ci} &= \left(\frac{2\,K_u V}{\mu}\right)\left(1 - \sqrt{\frac{25\,k_B T}{K_u V}}\right). \end{aligned} \tag{39}$$

When $V \to \infty$ or $T \to 0$, $H_{ci} \to 2\,K_u V/\mu = H_{ci0}$

$$H_{ci} = \frac{H_{ci}}{H_{ci0}} = 1 - \left(\frac{V_p}{V}\right)^{1/2} = 1 - \left(\frac{D_p}{D}\right)^{3/2}. \tag{40}$$

As can be seen, the coercivity increases as the particle diameter increases beyond $D_p$.

Experimentally, there are two key factors[23] for superparamagnetism.

---

[23] Another practical difference is that superparamagnets can have large values of the magnetization at ordinary temperatures and fields, making it easier to observe, while paramagnets may need low temperatures and high fields in order to be observed.

(1) Magnetization curves measured at different temperatures superimpose when $M$ is plotted as a function of $H/T$.
(2) There is no hysteresis: the remnance and the coercivity are both zero.

Both of these features are illustrated by the measurements, made by Bean and Jacobs [110], on fine iron particles dispersed in solid mercury shown in figure 29. The curves at 200 and 77 K show typical superparamagnetic behaviour. By 4.2 K, the particles no longer have enough thermal energy to overcome the energy barrier and switch their magnetization in the time available during the measurement. This is also demonstrated by Majetich and Jin [98] when they used Lorentz microscopy to observe the magnetization directions of individual nanoparticles.

Néel [101] also pointed out that the remnance magnetization ($M_R$) observed at a given temperature should be a measure of the amount of material with a particle volume greater than that just stable at the given temperature. Therefore, by following the increase in the remnance magnetization with decreasing temperature, one can find out how much material lies in various volume ranges and (at least in principle) one could also obtain the entire particulate volume distribution. Furthermore, since superparamagnetism has a very well defined dependence on temperature and volume, the curves themselves can be used to determine the size distribution of nanoparticles. Heukelom and Reijen [102] were also the first to do a fit to determine the size distribution and Weil [111, 112] did an excellent analysis of the size distributions of Ni spheres in powder form and Co granules in Cu–Co alloys. Obviously, superparamagnetism is not just observed in nanoparticles, but also in thin films [113] and granular GMR materials [114–124]. In both cases it yields the same information about the superparamagnetic material.

However, geometry, finite size effects and organization (random or assembled) can all have significant effects on the magnetization response of nanoparticles. Cowburn *et al* [60, 125] and Stamm *et al* [126] have both investigated this dependence on geometry in different materials. Finite size effects have been examined both experimentally [127–129] and theoretically [130]. Finally, deviations from this model of superparamagnetism have been discussed both experimentally and theoretically in [131–133]. Berkowitz also wrote an excellent general review [134] of fine particle magnetism.

The key point of superparamagnetism is that it is a thermal effect that is defined according to a timescale. If the measurement takes 10 s and the system can appreciably relax in less than 10 s, then you have a superparamagnetic system; if the system takes longer than 10 s to relax, then you have a ferromagnet. If the measurement takes 100 s, then the system has 100 s to relax in order to observe superparamagnetism.

### *4.3. Macroscopic quantum tunnelling*

MQT [135] is the sister of superparamagnetism. Where superparamagnetism is the result of thermal excitation of the magnetic moment over the barrier to reverse the particle's magnetization direction, MQT is tunnelling of the magnetic moment through the barrier [136]. Quantum tunnelling of an electron is a well understood phenomenon, both experimentally and theoretically. The electron trapped in a well is a standard introductory quantum mechanics problem. Tunnelling is regularly encountered in many devices, especially semiconductor devices. However, all of this is on a microscopic scale—although an experimentalist can measure the macroscopic quantity of the current resulting from the electrons tunnelling though the barriers. Not until recently, with the advent of the single-electron transistor[24] (see section 8.2.2), has the observation of a single electron tunnelling through a barrier been

---

[24] Quantum dots have also been used to observe charging of a capacitor with single electrons.

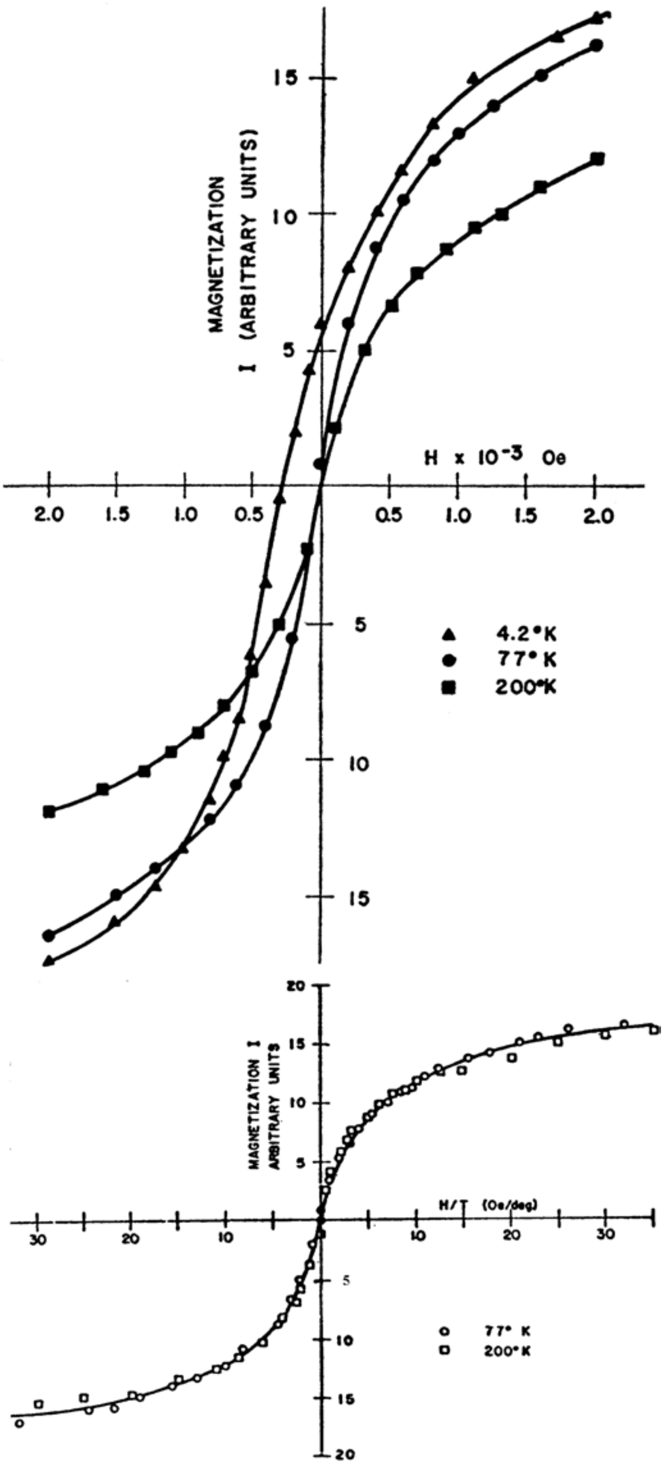

**Figure 29.** (a) Magnetization curves of iron particles (radius 2.2 nm) dispersed in mercury; (b) $H/T$ superposition of the curves. (From [110].)

observed. The next step is to observe a macroscopic quantity tunnel through a barrier. (By macroscopic, it is assumed that the object is large enough to behave classically most of the time it is being observed—i.e. quantum transitions are very rare—and that it is not strongly disturbed by the interaction with the measuring device.) The current interest is in observing the magnetic moment of a ferromagnetic/antiferromagnetic particle tunnel through a barrier. This effect can only be observed at extremely low temperatures, where the thermal excitation probability is extremely low.

The general tunnelling rate is given by

$$\Gamma(T) = A(T)\mathrm{e}^{-B(T)}. \tag{41}$$

The classical over-barrier excitation is given by equation (33). The quantum mechanical escape rate is

$$\Gamma_{QM} = \left(\frac{2T}{\hbar}\right)\left(\frac{\mathrm{Im}\{Z\}}{\mathrm{Re}\{Z\}}\right). \tag{42}$$

Analysis of the second order transition for $\Gamma_{QM}$ yields (at $T = 0$)

$$\Gamma_{QM} = \left(\frac{B}{2\pi}\right)^{1/2} \mathrm{e}^{-B} \left|\frac{\det[-\partial_T^2 + \partial_X^2 U(X=0)]}{\det[-\partial_T^2 + \partial_X^2 U(X=X_b)]}\right|^{1/2} \tag{43}$$

and (at high $T$)

$$\Gamma_{QM} = \Gamma_C = f_0 \mathrm{e}^{-(U_0/T)}. \tag{44}$$

The latter case agrees with the classical value as expected. The only effect of the thermal bath on the transition rate occurs via the temperature. Interactions with the microscopic degrees of freedom change the particle dynamics by creating dissipation. Assuming that the friction is linear with respect to the velocity, the exponent $B$ in equation (43) changes to

$$B \sim B_0\left(1 + \frac{\eta}{\omega_0}\right) \tag{45}$$

where $\omega_0$ is the instanton frequency, $\eta$ is the friction constant and $B_0$ is the bare exponent. The prefactor $f_0$ is generally assumed to be $10^9$ Hz—only for precise comparison between experiment and theory is the exact value necessary. (For further information, see [135].)

From an experimentalist's point of view, it is more convenient to express equation (41) as

$$\Gamma(T) = A(T)\mathrm{e}^{-\left(\frac{U_0}{T_{esc}(T)}\right)} \tag{46}$$

where $T_{esc}$ is the characteristic 'escape temperature'. At higher $T$, $T_{esc} = T$ (the over-barrier transition rate), and at lower $T$ (quantum tunnelling), $T_{esc}$ is a non-zero constant. The same equation determines both superparamagnetism and MQT. However, it is only at low $T$ that the thermal transitions die out and the magnetic moment freezes (within the classical approximation) into a single energy minimum. Only when this happens can quantum tunnelling between states be observed.

As discussed in superparamagnetism, the energy barrier for reversing the magnetization direction of a particle is given by equation (28). It is this volume $V$ that makes the energy barrier insurmountable for the classical particle (even if it were possible to have a micron- or millimetre-sized single-domain particle). Just as in superparamagnetism, only when the particles are small enough will $K_u V$ be small enough to observe tunnelling.

In addition to the requirements of low temperature and small size, the particle must be firmly coupled with a solid matrix because of angular momentum conservation [137]. The angular momentum for a magnetic system is given by $L + \gamma^{-1} M$ where $\gamma$ is the gyromagnetic ratio, $L$ is the rotational angular momentum and $M$ is the magnetization. If the magnetization is purely of spin origin, $\gamma^{-1}M = S$. Therefore, $M \to (-M)$ cannot occur in a free non-rotating particle since $L = 2\gamma^{-1}M$ and $E_{kinetic} = L^2/2I$ (where $I$ is the moment of inertia of the particle) would be created in the final state. For nanometre sized particles, this is non-negligible, and the energy of the final state would be significantly greater than the energy of the initial state, thereby forbidding tunnelling from $M \to (-M)$. To compensate for this, one of four things must be done.

1. The particle must be prepared in a metastable state at sufficiently high magnetic fields.
2. If the particle starts with zero total angular momentum ($L = -\gamma^{-1}M$) and an integral total number of spins $S$, then the energy is invariant under a simultaneous change of sign of both the spin and the angular momentum. (Since $L$ is always integral, $S$ must be as well. This agrees with Kramers' theorem from quantum mechanics: under no circumstances can a half-integer spin tunnel in the absence of a field.) Unfortunately, this is not feasible to study experimentally.
3. The particle must be embedded in a large solid matrix. (This means that the tunnelling probability is likely to depend on how firmly the particle is coupled with the matrix.) In order to conserve momentum, $L = -2\gamma^{-1}M$. If this is received by the entire matrix, then it will rotate with an angular velocity of $\omega = L/I_m$ and gain a kinetic energy of $L^2/2I_m$ where $I_m$ is the moment of inertia of the matrix. This is negligible if the size of the matrix is at least 100 times larger than the size of the particle. (For a more careful analysis, see [137].)
4. Transitions can also be induced by placing the particle in a uniform magnetic field. (Therefore, $k = 0$ phonons of spin $S = 1$ are produced in order to conserve the angular momentum.) Many phonons may be required for particles with a large spin moment.

There are two main tunnelling mechanisms for large monodomain particles. The first is coherent rotation, which is what is assumed for all further discussions unless specifically mentioned otherwise. The second is non-uniform curling [138–142]. This only occurs for sufficiently large uniformly magnetized particles. The extreme case of this is when the size of the monodomain particle is large compared to the magnetic dipole energy. In this case, tunnelling could, in principle, occur by domain wall motion [143]. Then,

$$B \sim \left(\frac{E_{anisotropy}}{E_{dipole}}\right)^{1/2} S \tag{47}$$

where $B$ is the exponent in equation (41). However, $d \gg \lambda \Rightarrow S \gg 1$. $E_{anisotropy} \gg E_{dipole}$ so $B$ is very large, but this makes $\mathrm{e}^{-B}$ exponentially small! However, if the energy barrier were lowered by applying a field, then the domain wall motion would speed up. Alternatively, if the particle is full of defects, then the domain wall could be pinned, limiting the domain wall motion to thermal and quantum hopping. Also, field induced domain wall entry is possible, which should be similar to the tunnelling of the domain wall in bulk ferromagnets. Therefore, the latter case only applies to particles with

$$S > \left(\frac{E_{exchange}}{E_{anisotropy}}\right)^{3/2}. \tag{48}$$

Therefore, we shall only concern ourselves with particles where

$$S > \left(\frac{E_{exchange}}{E_{anisotropy}}\right). \tag{49}$$

Now, assuming all of the above information, there are four models that have been examined in the literature. Only two of these will be discussed here—a simple model to introduce the concepts and a more experimentally useful model. Furthermore, although there are different ways of reaching the same conclusions, the methods of Chudnovsky and Tejada [135] are discussed here for ease of understanding. Recall that the component that primarily determines the tunnelling rate is $B(T)$ from equation (41).

*4.3.1. Model I—simple case.* Assuming a particle with a doubly degenerate state, and a magnetic volume $V$, the total anisotropy energy is

$$E = V(K_\perp \cos^2\theta - K\sin^2\theta\cos^2\phi). \tag{50}$$

Let $K_\perp > 0$, $K_\parallel > 0$, $X$–$Y$ be the easy plane, and $X$ be the easy direction. The energy minimum occurs at $\phi = 0, \pi$ and $\theta = \pi/2$—the $\pm X$ directions. The energy barrier is therefore equal to $K_\parallel V$ for rotation in the $X$–$Y$ plane, and $(K_\perp + K_\parallel)V$ for rotation in the $X$–$Z$ plane. Using this information, the tunnelling rate is calculated to be

$$\Gamma = |\cos(S\pi)|\omega_0 \exp\left\{-2S\ln\left[\sqrt{1+\left(\frac{K_\parallel}{K_\perp}\right)} + \sqrt{\frac{K_\parallel}{K_\perp}}\right]\right\}$$

where

$$\omega_0 = \left(\frac{2\gamma}{M_0}\right)\sqrt{K_\parallel(K_\parallel + K_\perp)}. \tag{51}$$

For integer $S$, the MQT rate simplifies to (equation (52))

$$\Gamma \sim \begin{cases} \omega_0 \mathrm{e}^{-S\ln\left(\frac{4K_\parallel}{K_\perp}\right)} = \omega_0\left(\dfrac{K_\perp}{4K_\parallel}\right) & \text{for } K_\perp \ll K_\parallel \\ \omega_0 \mathrm{e}^{-2S\left(\frac{K_\parallel}{K_\perp}\right)^{1/2}} & \text{for } K_\perp \gg K_\parallel. \end{cases} \tag{52}$$

For half-integer $S$, the MQT rate equals zero (as expected). The quantum transitions dominate for cross-over temperature below (equation (53)):

$$T_C = \begin{cases} \dfrac{\mu_B H_\parallel}{\ln\left(\frac{4H_\parallel}{H_\perp}\right)} = \dfrac{2\mu_B K_\parallel}{M_0\ln\left(\frac{4K_\parallel}{K_\perp}\right)} & \text{for } K_\perp \ll K_\parallel \\ T_C = \dfrac{1}{2}\mu_B(H_\parallel H_\perp)^{1/2} = \dfrac{\mu_B}{M_0}(K_\parallel K_\perp)^{1/2} & \text{for } K_\perp \gg K_\parallel \end{cases} \tag{53}$$

where $H_{\parallel(\perp)} = \frac{2K_{\parallel(\perp)}}{M_0}$ and $\mu_B = \frac{\hbar\gamma}{2}$. The tunnelling rate can significantly increase in the presence of the magnetic field that lowers the energy barrier.

*4.3.2. Model II—experimentally important model.* This is the most significant model for experiments. Assuming a system of particles with a uniaxial anisotropy, where the easy axis is along the $Z$-direction, then the magnetic field is applied at an angle $\theta_H$ to the anisotropy axis [144–146]. If the magnetic field is applied in the $X$–$Z$ plane at an angle $\theta_H$, where $90° \leqslant \theta_H \leqslant 180°$ and the field is below some critical value $H_{CV}(\theta_H)$, then $M$ has two equilibrium orientations. The first is metastable: $\theta_A$ is between 0° and 90°. The second is an absolute minimum and occurs for $90° \leqslant \theta_A \leqslant 180°$. Therefore, the point is to find the quantum decay of the metastable state. The magnetic energy is given by

$$E = -kM_Z^2 - M_X H_X - M_Z H_Z \tag{54}$$

where $k > 0$ is a dimensionless anisotropy constant. For an arbitrary orientation of $M$

$$E = -H_a M(\tfrac{1}{2}\cos^2\theta + h_Z\cos\theta + h_X\sin\theta\cos\phi) \tag{55}$$

where $H_a = 2\,kM$ is the anisotropy field, $h_{x,z} = H_{x,z}/H_a$ are the components of the field in the $X$- and $Z$-directions respectively and $\theta$ and $\phi$ are the conventional spherical coordinates of the magnetization vector $M$, which is a fixed length vector. The metastable state exists at $H_z < 0$. In order for this state to decay, it must either (as shown in figure 26) fluctuate to the top of the barrier at $\theta = \theta_1$ or tunnel under the barrier to $\theta = \theta_2$. Since $M$ is macroscopic, an appreciable escape rate is expected only when the barrier is lowered to $h_c(\theta_H)$ by tuning the external field. The appropriate values are

$$\begin{aligned} &h_c(\theta_H) = (\sin^{2/3}(\theta_H) + |\cos(\theta_H)|^{2/3})^{-3/2} \\ &\sin^3\theta_C = h_c \sin\theta_H. \end{aligned} \tag{56}$$

For a field $h = h_c\ (1 - \varepsilon)$ where $\varepsilon \ll 1$, this preserves the metastable state. The equilibrium value of $\theta$ is $\theta_c - \theta = \Delta \ll 1$ where $\Delta = (2\varepsilon/3)^{1/2}$. $B$ is then given by

$$B = \left(\frac{16\sqrt[4]{6}}{5}\right) S\varepsilon^{5/4} |\cot\theta_H|^{1/6}. \tag{57}$$

(Note the edges—at 90° and 180°—are invalid. They do not take into consideration the symmetry of the problem.) At this point, it is important to recall that a low barrier was assumed. This assumption must be verified at this point.

$$\begin{aligned} &U_0 = \hbar\omega_a S \left(\frac{2\varepsilon}{3}\right)^{3/2} \sin(2\theta_c) \\ &\frac{U_0}{\hbar\omega_a} = \frac{5}{36} B. \end{aligned} \tag{58}$$

At sufficiently large $T$, the tunnelling exponent becomes a Boltzmann distribution. This crossover temperature can be estimated by the following:

$$\frac{U_0}{T} = B = \frac{\frac{5}{36} B\hbar\omega_a}{T_c} \Rightarrow T_c = \frac{5}{36}\hbar\omega_a. \tag{59}$$

Due to the exponential dependence of the thermal rate on temperature, a well defined cross-over from thermal to quantum is expected.

Experimentally, this model provides three control parameters: (1) the orientation of the field, (2) the field strength and (3) the temperature. However, to do anything experimentally with this system, you need either a large number of identical particles or a single particle of carefully chosen size (neither a long nor a short lifetime) where $B \sim 30$ and $S \sim 3 \times 10^4$. Furthermore, several other effects need to be taken into account for complete analysis, including dissipation [147, 148], quantum coherence and quantum decoherence.

*4.3.3. Tunnelling of the Néel vector.* Other examples of MQT include tunnelling of the Néel vector in antiferromagnetic particles [149], quantum nucleation of magnetic domains, quantum tunnelling/de-pinning of domain walls [150], the effect of dissipation on tunnelling of domain walls [151, 152] and tunnelling of flux lines in superconductors. However, we will only discuss one more case of MQT—the tunnelling of the Néel vector (figure 30). This can only be detected if the particle has a small magnetic moment due to the non-compensation of the sub-lattice. Sources of the non-compensation are

- irregular shape of the particle,
- canting of the sub-lattices and
- different values of the magnetic moments on the different sub-lattices.

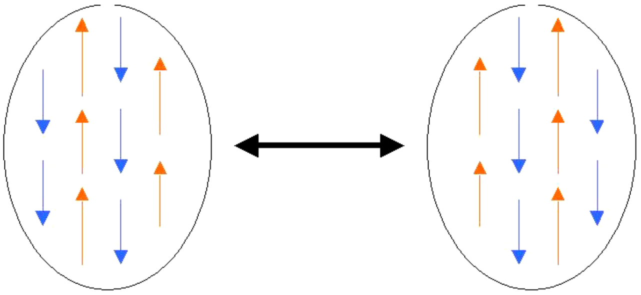

**Figure 30.** Tunnelling of the Néel vector in antiferromagnetic particles.

Assuming tetragonal anisotropy, $K_\perp \gg K_\parallel$, with the easy axis along $X$ with the $X$–$Y$ plane being the easy plane, the tunnelling rate is given by

$$\Gamma \approx |\cos(S\pi)|\omega_0 \mathrm{e}^{-(2V/\hbar\gamma)(2\chi_\perp K_\parallel + m^2(\frac{K_\parallel}{K_\perp}))} \tag{60}$$

where $\chi_\perp^{-1} m_1 m_2$ is the strong exchange interaction, and $m_1$ and $m_2$ are the magnetizations. A large non-compensation means that $m \gg (\chi_\perp K_\perp)^{1/2}$, but a small non-compensation means that $m \ll (\chi_\perp K_\perp)^{1/2}$. For any $m \neq 0$, a $K_\perp \neq 0$ is required in order to obtain a non-zero tunnelling rate. The cross-over temperature for an almost compensated antiferromagnet can then be determined from the following:

$$\begin{aligned} &\left(\frac{K_{\parallel V}}{kT_c}\right) = \left(\frac{2V}{\hbar\gamma}\right)\left(2\chi_\perp K_\parallel + m^2 \frac{K_\parallel}{K_\perp}\right)^{1/2} \\ &T_c \sim \hbar\omega_0 = \mu_B (H_\parallel H_{ex})^{1/2}. \end{aligned} \tag{61}$$

It is the exchange field $H_{ex}$ that causes the cross-over temperature to occur at a higher value than for ferromagnetic magnetizations. There are a few caveats to this system, however. The tunnelling is stronger for compensated structures or nearly compensated. However, there exists a cross-over point from a strong antiferromagnet to a weak ferromagnet. This occurs at approximately:

$$m \approx (\chi_\perp K_\perp)^{1/2}. \tag{62}$$

To ensure that the dynamics of the problem remain antiferromagnetic, the non-compensation should be on the order of 1%, or

$$\frac{m}{m_1} < \left(\frac{H_\perp}{H_{ex}}\right)^{1/2}. \tag{63}$$

This means that the tunnelling rate can be rewritten as

$$\Gamma \approx \omega_0 \mathrm{e}^{-B(T)} \sim \left(\frac{kT_C}{\hbar}\right) \mathrm{e}^{-Ns_0\left(\frac{H_\parallel}{H_{ex}}\right)^{1/2}}. \tag{64}$$

Further analysis of the tunnelling of the Néel vector—taking into account fields applied at an angle—is outlined in [153, 154].

Experimentally, the primary search for MQT has been via quantum magnetic relaxation [155, 156]. However, this was not the method used in the earliest work on MQT by Awschalom *et al* in 1990 [157]. Unfortunately, at the time, MQT theory did not include dissipation and so the results appeared anomalous. The first claimed observation of MQT was in 1995 by Coppinger *et al* [158], but the subsequent argument in the literature about what exactly was occurring experimentally prevented this from being conclusive. The first convincing experimental observation of MQT was by Thomas *et al* [159] on the $\mathrm{Mn}_{12}$ acetate system. Further work on $\mathrm{Mn}_{12}$ acetate has been spearheaded by Barbara [160–162]. Since then, MQT has also been observed in barium ferrite [163, 164], ferritin [165], $\mathrm{CoFe_2O_4}$ and $\gamma$-$\mathrm{Fe_2O_3}$ [166]. This research area has expanded so rapidly that a review of the progress in $\mathrm{Mn}_{12}$ acetate and $\mathrm{Fe}_8$ has been published [167]. However, care must be taken during the interpretation of the results—interaction affects and energy barrier distributions can appear to be MQT, while in reality they are not [168].

### *4.4. Summary*

The key points about superparamagnetism and MQT are the following:

(1) Superparamagnetism is a microscopic effect while MQT is macroscopic.
(2) Superparamagnetism occurs due to thermal excitation over an energy barrier. MQT is a quantum effect—tunnelling through a barrier.

As a direct result of the last statement, superparamagnetism takes place at high temperatures (depending on material, but on the order of 100 K— $T > T_B$) whereas MQT can only be observed experimentally at very low $T$ (thermal effects dominate if $T$ is too high, so the only experimental observation took place in the mK regime— $T < T_C$). In either case, the phenomena occur only when the particle is engineered to be single domain, and when the temperature is low enough.

## 5. Magnetoresistance

### *5.1. Spin diffusion length*

*5.1.1. Theory.* Although the exchange length and domain size discussed previously also play important roles in magnetoresistive systems, another effect comes into predominance—the spin diffusion length, $l_{SD}$. This characteristic length scale defines the average distance that a spin can travel before it flips. Unlike the previous length scales, the spin diffusion length is the direct result of diffusion processes for magnetization and momentum and can be understood when approached as a random walk problem [169]. The lateral displacement of the spin, the spin diffusion length, is

$$l_{SD} = \sqrt{N}\lambda_{mfp} \tag{65}$$

where $N$ is the number of momentum scattering events and $\lambda_{mfp}$ the mean free path. The total path travelled by the spin before flipping is

$$N\lambda_{mfp} = v_F\tau_{\uparrow\downarrow} \tag{66}$$

where $v_F$ is the Fermi velocity and $\tau_{\uparrow\downarrow}$ is the spin relaxation time. Combining equations (65) and (66) yields

$$l_{SD} = \sqrt{\lambda_{mfp}v_F\tau_{\uparrow\downarrow}}. \tag{67}$$

In order for the spin-dependent scattering to be a significant part of the total resistance, the layers must be thinner than the spin diffusion length of electrons in the bulk material.

*5.1.2. Experiment.* The initial experiments to measure the spin diffusion length were in ferromagnetic metals and ordinary metals. Gurney *et al* [170] measured the spin diffusion length at room temperature in magnetic and non-magnetic metals using a backed spin valve structure (figure 31). This standard trilayer structure consisted of a thick, pinned ferromagnetic

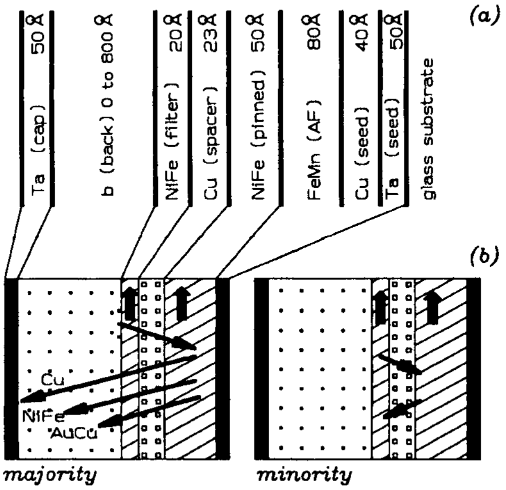

**Figure 31.** Backed spin valve structure used by Gurney to measure the spin diffusion length. (From [170].)

layer, a thin free layer and the metal to be probed, which was deposited on top of the free layer. The moment of the free layer can be switched in order to choose the type of carrier—minority or majority. Since the variation in conductance $\Delta G$ depends upon both the thickness of the probe layer and the spin diffusion length (according to a classical model derived from the Boltzmann transport equation [170, 171]), measuring the conductance of the structure for various thicknesses of the probe metal yields an average value for the carrier spin diffusion length[25]. For Co, $l_{SD} = 5.5$ nm $\gg l^*_{SD} = 0.6$ nm; for $Ni_{80}Fe_{20}$, $l_{SD} = 4.6$ nm $\gg l^*_{SD} = 0.6$ nm; for Fe, $l_{SD} = 1.5$ nm $\approx l^*_{SD} = 2.1$ nm; for Cu and $Au_{50}Cu_{50}$, $l_{SD}$ is 22.6 and 2.0 nm, respectively. Yang *et al* [172] deduced the spin diffusion lengths of a variety of multilayers by using the Valet–Fert model (see section 5.4) of CPP-MR to fit the experimental data. The measured values for Ag and Cu are 500 and 450 nm respectively, but the inclusion of magnetic impurities can reduce these values by up to two orders of magnitude.

The recent attempts to harness the electrical properties of semiconductors have led to measurements of the spin diffusion length in semiconductors, particularly Si and GaAs. Gregg *et al* [169], by placing two Co contacts separated by 1–64 $\mu$m of silicon (figure 32) and then measuring the MR, determined that the spin diffusion length in silicon is greater than 64 $\mu$m. Numerical calculations [173] suggest that this number is actually significantly larger, on the order of 280 $\mu$m. Direct measurements of the spin diffusion length in GaAs by optical pumping (the selection rules are such that the conduction band is populated primarily by spins of one type) by Awschalom *et al* [174–176] and Dzhioev *et al* [177] yield shorter spin diffusion lengths—about 100 $\mu$m. The difference between these two numbers originates from the dominance of different spin–flipping mechanisms[26] in different semiconductors [184].

### *5.2. Magnetoresistance—types and origin*

Of all the transport properties, magnetoresistance is the most important for device applications. The definition of MR is the change in resistance of a given material under an applied magnetic

---

[25] * indicates a minority carrier, just as in equation (70).

[26] All of the mechanisms are due to the interactions of the spins with the crystal lattice or with impurities. The four most important mechanisms in semiconductors are optical excitation [178], D'Yakonov–Perel [179–181], Bir–Aronov–Pikus [182] and Elliot–Yafet [183].

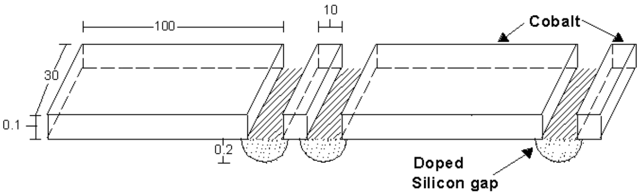

**Figure 32.** Schematic diagram of measuring the spin diffusion length in silicon via Co contacts (dimensions are in microns).

**Table 1.** Type, origin and strength of different MRs.

| Type of MR | Origin | Increase in resistance (at room temperature) (%) |
|---|---|---|
| AMR[a] | Spin–orbit interaction | 5 |
| LMR[b] | Curved paths from the Lorentz force | $B^2$ |
| GMR | Spin-dependent transport | 50 |
| CMR | Band-splitting due to ordering onset | 5 |

[a] AMR is sometimes also referred to as extraordinary magnetoresistance (EMR).
[b] LMR is sometimes referred to as ordinary magnetoresistance (OMR) or just MR.

field and is normally written[27] as

$$MR(\%) = \left(\frac{R_H - R_0}{R_0}\right) \times 100 \tag{68}$$

where $R_H$ is the value of resistance under a magnetic field $H$ and $R_0$ is the resistance in zero field. Some authors use a similar definition but with $R_H$ in the denominator. Unless clearly stated otherwise, the values of MR are calculated using equation (68).

Although this definition appears at first glance to be quite simple and straightforward, this is not quite true. There are a number of different kinds of MR, each with a different origin. Among these are anisotropic magnetoresistance (AMR), Lorentz magnetoresistance (LMR), GMR and colossal magnetoresistance (CMR). The origin and strength of each of these are outlined in table 1.

*5.2.1. Lorentz magnetoresistance.* LMR [185] only occurs in a conductive material in the presence of a magnetic field. It originates from the Lorentz force, which causes electrons in a material under the influence of a magnetic field to flow in a curved path rather than a straight line, thereby lengthening the total distance they travel. This increases the number of collisions each electron experiences, thereby increasing the resistivity as well; the larger the field, the larger the resistance is. This effect generally follows a $B^2$ dependence (although high magnetic fields and low temperatures are complications), so it is readily separable from the other types of MR. In general, when the field is perpendicular to the current the effect is larger than when the field is parallel.

*5.2.2. Anisotropic magnetoresistance.* AMR was first discovered [186] by Kelvin in the late 1850s. This MR can only be observed in magnetic materials (like Fe, Co, Ni and their alloys [187, 188]) since it depends on the relative orientation of the magnetization and the current in a single material [189]. Specifically, AMR measures the change in resistance when

---

[27] The MR has also been defined as $(R_H - R_0)/R_H$ and as the ratio $R_0/R_H$.

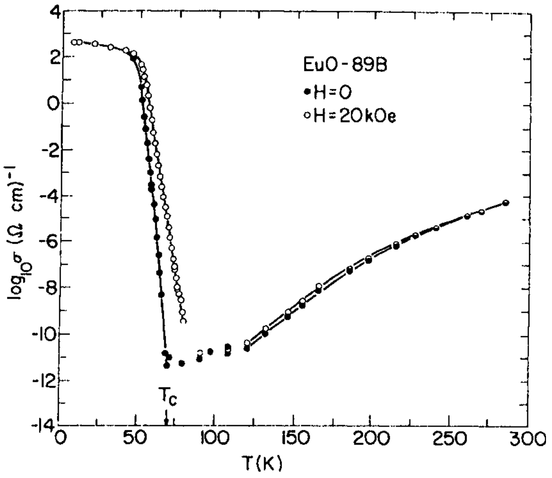

**Figure 33.** Resistance of non-stoichiometric (Eu-rich) EuO versus temperature. (From [194].)

the current flows parallel to the magnetization and when it flows perpendicular and can be written as

$$\rho = \rho_0 + \Delta\rho\cos^2\theta \tag{69}$$

where $\rho$ is the measured resistance, $\rho_0$ is the resistance of the material in zero field, $\Delta\rho$ is the measured change in resistance and $\theta$ is the angle the current makes with respect to the magnetization. In general, the resistance increases in bulk materials when the current and magnetization are parallel and decreases when they are perpendicular. This effect originates from the spin–orbit interaction between the conduction electrons and the fixed magnetic orbital. The magnetization of the system deforms the electron cloud, thereby changing the rate of spin–orbit scattering, resulting in anisotropic conduction[28].

*5.2.3. Giant magnetoresistance.* GMR describes the behaviour of heterogeneous magnetic systems that have alternating layers of ferromagnetic and non-magnetic materials—either in the form of multilayer or granular systems [190, 191]. Unlike either LMR or AMR, this effect arises as a result of spin-dependent transport within the system. The basic component of a GMR multilayer system (the same principle applies to granular systems) consists of two thin, ferromagnetic layers separated by a thin non-magnetic conducting layer. The resistivity of the system depends on the relative alignment (parallel or antiparallel) of the moments of the ferromagnetic layers. Layers with parallel magnetic moments have less scattering at the interfaces, longer mean free paths and lower resistance. Layers with antiparallel magnetic moments have more scattering at the interfaces, shorter mean free paths and higher resistance. However, in order for the spin-dependent scattering to be a significant part of the total resistance, the layers must be thinner than the spin diffusion length (now the defining length scale) of electrons in the bulk material.

*5.2.4. Colossal magnetoresistance.* CMR describes the MR behaviour of certain materials, namely the mixed valence manganites with the perovskite structure[29]. These materials exhibit

---

[28] This anisotropy actually refers to the orientation of the field and current flow, not to how the orbital deformation varies for different applied field directions.

[29] For an excellent review of this material, see [193].

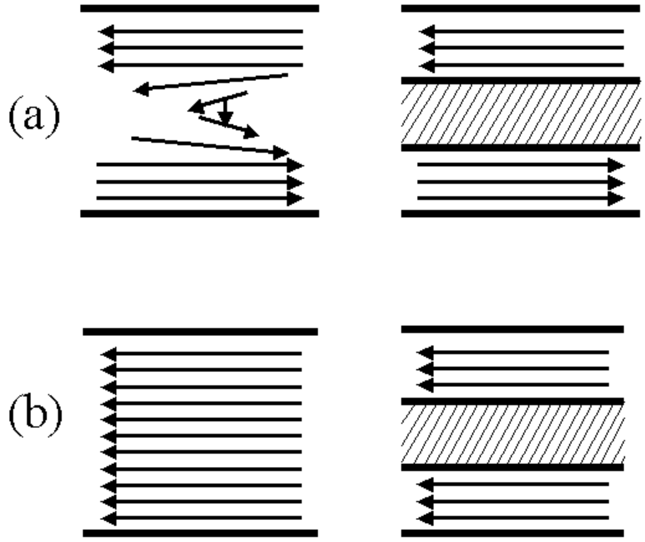

**Figure 34.** Geometric similarities of (a) an FM domain wall and (b) a GMR trilayer.

(figure 34) very large magnetoresistance around their ordering temperature (either the Curie or Néel temperature). The main mechanism controlling this phenomenon is double exchange, where the magnetic coupling between neighbouring $Mn^{3+}$ and $Mn^{4+}$ ions is mediated through the transfer of an electron with spin memory. However, the crystal lattice also plays a role via the Jahn–Teller distortion associated with the $Mn^{3+}$ ion. Crudely put, the Jahn–Teller effect only permits degeneracy of the spin-up and spin-down states (in systems without magnetic ordering) in the ground state of any quantum system. Therefore, around a structural phase transition, the symmetry of the crystal is reduced by elongating the crystal in a particular direction. This induces ferromagnetic or anti-ferromagnetic ordering.

*5.2.5. Domain wall magnetoresistance.* In sections 2 and 3, the connections between the domain configuration, energy and reduction of the lateral dimensions were explored. In this section, however, the focus centres on what happens macroscopically when a current is passed through a single-domain wall. Just as for the previous structures, this system has to be engineered on the nanoscale in order to isolate a single domain wall so that its effect can be measured. However, in this case, the length scale that dominates the physics observed is the spin precession length.

(a) *Theory—spin precession in domain walls.* In domain walls, the mixing of spin-up electrons and spin-down electrons arises from a mistracking effect, where the transport electrons' spin lag behind in orientation with respect to the local magnetization orientation inside the domain wall (see figure 35). By analogy with GMR multilayers (see section 5.2.3) and homogeneous magnetic media [195, 196], the magnetic domain wall (or region of twisted magnetization) replaces the non-magnetic spacer layer (figure 34). Just as a GMR trilayer functions provided that spin conservation occurs across the intermediate zone, this model of domain wall resistance [195–197] is determined by the degree of spin depolarization in the twisted magnetic structure which forms the heart of the domain wall. The model invokes spin precession in the ferromagnetic exchange field to determine the degree of electron spin mistracking on passing through the domain wall. This mistracking of a spin

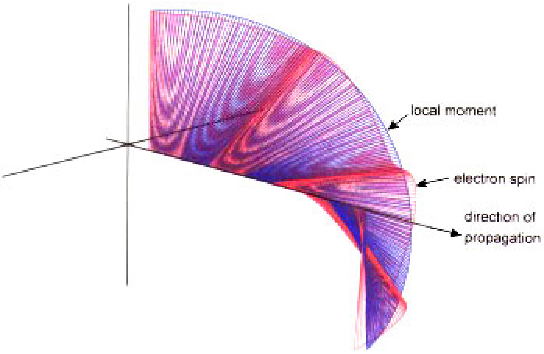

**Figure 35.** The spin trajectory is shown for the electrical carriers in transit through domain walls in Co (typical Co wall thickness of ∼15 nm). The spin orientation is shown in red and the local exchange field in blue.

leads to its making an average angle $\theta$ with the local magnetization direction in the domain wall and this corresponds to its wavefunction being contaminated by a fraction $\sin(\theta/2)$ of the opposite spin wavefunction. It is then susceptible to additional scattering by an amount equivalent to $\langle \sin^2(\theta/2)\rangle$ multiplied by the opposite spin scattering rate. This model leads to equation (70), an expression for the spin-dependent contribution—the spin precession length—to the domain wall resistivity:

$$\frac{\delta\rho_w}{\rho_0} = \left(\frac{\lambda^*}{\lambda} + \frac{\lambda}{\lambda^*} - 2\right)\left\langle \sin^2\left(\frac{\theta}{2}\right)\right\rangle \tag{70}$$

where $\lambda$ and $\lambda^*$ are the majority and minority spin mean free paths and $\rho_0$ and $\delta\rho_w$ are the bulk ferromagnetic resistivity and the resistivity increase for domain wall material, respectively. The model was re-analysed by Levy and Zhang in [198] by replacing this simple rotating frame approach with a sophisticated quantum mechanical analysis with spin-dependent scattering and spin channel mixing localized inside the domain wall; to within a simple numerical factor, identical results are obtained.

This spin-dependent contribution differs from the contributions [198–200] from the many possible mechanisms for domain wall magnetoresistance (DW-MR) in that it predicts not a fixed value of resistance for the wall, but rather a ratio increase based on the bulk value for the material.

(b) *Experimental evidence.* Many experiments on DW-MR used a system of magnetic stripe domains [195, 201–203], taking advantage of the high density of domain walls and assuming that the domain resistance and the domain wall resistance form a series of resistors. However, the presence of other MR effects (see section 5.2) such as AMR [189] or Lorentz-MR [185] as well as a complex domain wall structure often require a manipulation of the measured MR data in different magnetization configurations in order to extract the contribution from the domain wall [202]. These ‘parasitic’ effects can be avoided using the parallel wire configuration described in figures 22– 25, in which a discrete number of isolated head-to-head domain walls can be stabilized which separate opposite domains. The advantage of such a configuration is that the geometry is well defined during the reversal process, avoiding other MR contributions that may mask the DW-MR effect. Furthermore, the magnetization remains parallel or antiparallel to the current during the magnetization reversal process, whereas the domain walls are aligned perpendicular to the current and thus to the magnetization. The MR hysteresis loop of a

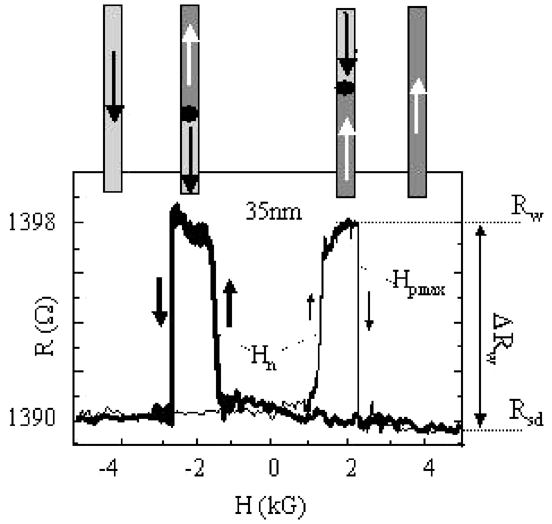

**Figure 36.** Magneto-resistance curve for a single 35 nm electrodeposited Co wire, measured as a function of a field applied parallel to the wire axis. $R_{sd}$ denotes the background signal level for a single-domain wire. $R_W$ denotes the signal level when one or two domain walls have been nucleated at $H_n$ during the reversal and are stabilized at pinning sites. (From [96].)

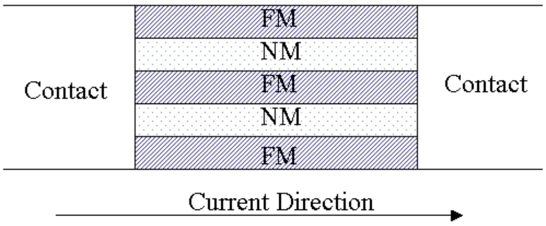

**Figure 37.** CIP geometry.

35 nm Co single wire shown in figure 36 illustrates the simplicity of this geometry [96]. There are two striking features in this loop:

(i) the background resistance level is almost flat over the field range measured and
(ii) two sharp jumps are visible, one upward at 1.3 kOe followed by a downward jump at 2.8 kOe.

The flat background level indicates, as expected, that the magnetization remains parallel to the current during the whole reversal process, confirming the MFM observations (figure 21(a)) that the effective easy axis is aligned nearly parallel to the wire axis. Since the upward jump appears around the nucleation field $H_{nucleation}$ where 1 kOe $< H_{nucleation} <$ 2 kOe, the upward and downward jumps are, respectively, identified as the nucleation field and the maximum de-pinning field $H_{pmax}$ at which all domain walls are expelled from the wire. It follows directly from this that the enhanced signal level in the field range $H_{nucleation} < H < H_{pmax}$ can be attributed to the presence of a finite number of domain walls which nucleate during the reversal and propagate along the wire. This is identified as DW-MR.

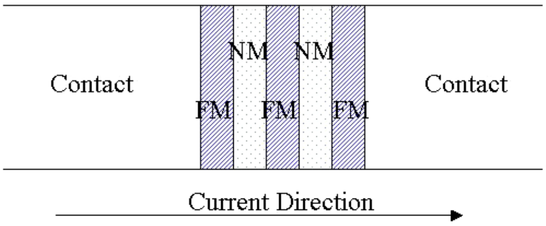

**Figure 38.** CPP geometry.

For all the Co wires measured, the MR ratio (see footnote 27) for a single wall has a value of $\Delta R_w / n R_{sd} = 0.1$–$0.3\%$ (where $n$ is the number of walls). This corresponds to a huge enhancement of the domain wall resistivity $\rho_w$ as compared to its resistivity $\rho_{sd}$ in the single-domain state. Indeed, taking the domain wall width $\lambda$ to be 10–15 nm and the length of the Co wire $l_{\mathrm{Co}}$ to be 20 $\mu$m, the resistivity ratio

$$\frac{\Delta\rho_w}{\Delta\rho_{sd}} = \left(\frac{\Delta R_w}{n R_{sd}}\right)\left(\frac{l_{\mathrm{Co}}}{\lambda}\right) \tag{71}$$

is between 100 and 600%. Such a large resistance enhancement in the presence of a domain wall has initiated further studies of spin-dependent transport in chemically homogeneous structures supporting an inhomogeneous magnetic structure.

### *5.3. GMR geometries*

*5.3.1. Current in plane versus current perpendicular to plane.* There are two principal geometries for measuring GMR. The current-in-plane (CIP) configuration is where, as its name implies, the current flows in the plane of the layers (figure 37). The current-perpendicular-to-plane (CPP) configuration is where the current flows perpendicular to the plane of the layers (figure 38). CIP is the typical geometry, since it is easier to fabricate (the transverse dimensions are on the order of $\mathrm{cm}^2$, but their thickness must be only a few nanometres so that the spin diffusion length can be effective), but CPP is easier to analyse theoretically. (In CIP, the thickness of the layers must be smaller than the mean free path in order for the carriers to be able to sample the magnetic orientation of the surrounding layers. In CPP, the layers must be thinner than the spin diffusion length in order for the spin to encounter the next magnetic layer before losing its spin memory.) Furthermore, because the layers are very thin, the resistance of the CPP geometry is extremely low, so special experimental techniques are required.

*5.3.2. Comparison—theoretical and experimental.* In a theoretical study of GMR, Zhang and Levy [204] proposed that a larger effect could be measured if the current were driven perpendicular to the plane of the layers (CPP configuration). They observed that, due to the inhomogeneous nature of multilayer structures, the application of a uniform electric field does not imply that the internal electric field is uniform. If the electric field is applied parallel to the layers, then the uniformity is maintained; if applied perpendicular to the layers, then the field varies from layer to layer (expressed as the inclusion of off-diagonal elements in the conductivity tensor $\sigma$). This means that the measured conductivity is anisotropic—different for electric fields parallel and perpendicular to the layers—and therefore dependent on the position of the conduction electrons in the structure. Furthermore, in the CIP configuration, the conduction electrons are not scattered by all the layers and all the interfaces; instead, the electron samples only from a region of size $\lambda_{mfp}$. In the CPP configuration, the electrons

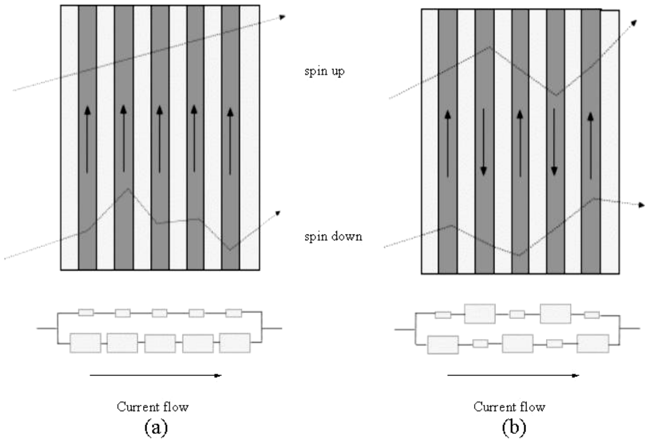

**Figure 39.** (a) Ferromagnetic and (b) antiferromagnetic configurations in the resistor network theory.

are scattered by every interface and every layer. As a result, for either the case where spin-dependent scattering is included or interface scattering is assumed to be negligible, the CPP-MR is higher because it samples all the layers and interfaces.

Pratt *et al* [205] confirmed this prediction by comparing the GMR of Co–Ag multilayers in the standard CIP geometry. By placing additional Nb electrodes at the top and bottom of the multilayer the authors were able to measure the CPP-MR. The resistance was estimated to be in the range $10^{-7}$–$10^{-8}$ for a sample 1 mm × 1 mm × 1 $\mu$m, so with an applied current of 10 mA the measured voltage was $10^{-9}$–$10^{-10}$ V (requiring high precision techniques to perform the measurements). The measured CPP-MR of the samples with various Co and Ag thicknesses had values ranging from 10 to 50% at 4.2 K and 500 G. The values measured under the same conditions in CIP geometry are three to ten times smaller.

### 5.4. GMR theory

The simplest model for GMR is what is commonly referred to as the resistor network theory of GMR. In this model, the resistance of a spin travelling through the ferromagnetic layer of the opposite orientation (call it $R_{\uparrow\downarrow}$) and the resistance of the spin travelling through a ferromagnetic layer of the same orientation (call it $R_{\uparrow\uparrow,\downarrow\downarrow}$) must be known. Furthermore, the resistances of each of the spins travelling though the non-magnetic layers must be known ($R_\uparrow$ or $R_\downarrow$). Now, the resistance can be calculated as a two independent channels of spin, operating in parallel, where the resistances used are based upon the orientation of the layers. In the ferromagnetic configuration (figure 39(a)), the resistance is

$$\frac{1}{R_F} = \left(\frac{1}{R_{\uparrow\uparrow} + R_\uparrow + R_{\uparrow\uparrow}} + \frac{1}{R_{\uparrow\downarrow} + R_\downarrow + R_{\uparrow\downarrow}}\right). \tag{72}$$

In the antiferromagnetic configuration (figure 39(b)), the resistance is

$$\frac{1}{R_A} = \left(\frac{1}{R_{\downarrow\uparrow} + R_\uparrow + R_{\uparrow\uparrow}} + \frac{1}{R_{\downarrow\downarrow} + R_\downarrow + R_{\uparrow\downarrow}}\right) = \frac{2}{R_{\uparrow\downarrow} + R_\downarrow + R_{\downarrow\downarrow}} \tag{73}$$

assuming that $R_{\uparrow\downarrow}$ is larger than $R_{\uparrow\uparrow,\downarrow\downarrow}$ and that $R_\uparrow = R_\downarrow$, this means that $R_F \ll R_A$.

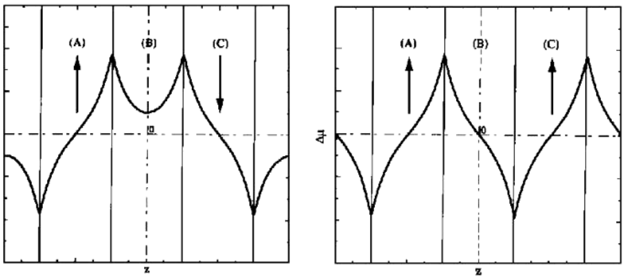

**Figure 40.** A and C are magnetic layers and B is the non-magnetic spacer in a multilayer structure. The figure shows the variation of the chemical potential for spin-up electrons as a function of the position. (From [207].)

A theoretical treatment of CPP-MR based on thermodynamic considerations has been proposed by Johnson [206] for the case of a paramagnetic layer separating two ferromagnetic electrodes. It assumes a shift of the chemical potential of the layers when the magnetizations are antiparallel, giving rise to an interface resistance $R_S$. The interface between paramagnetic and ferromagnetic layers is treated as a porous membrane separating two equilibrium systems with well defined entropy. Through the membrane the two layers can exchange charge, kinetic energy and magnetic moment. Transport equations for these quantities can be defined from linear response theory (see section 7.3.4) and an expression can be found for $R_S$ that depends on parameters that reflect the predominance of one spin direction in both paramagnetic and ferromagnetic layers. This model not only accounts for spin dependent scattering, but also introduces the concept of spin accumulation[30] at the interfaces. It considers that slow spin diffusion or relaxation leads to a steady-state non-equilibrium magnetization around the interfaces. This magnetization acts as a bottleneck for spin transport across the interface, which in turn will hinder the flow of charge. The effect applies to a single interface, but can be generalized to the multilayer structure by simply multiplying by the total number of bilayers. As there is no net charge transfer across the layers in the CIP case, there is no spin accumulation and therefore CIP-MR $<$ CPP-MR.

Valet and Fert [207] developed a CPP-MR model that provides great insight into the problem. The Boltzmann equation is solved at zero temperature by introducing into the distribution function an isotropic term to account for spin accumulation. For the case where the mean free path ($\lambda_{mfp}$) is much smaller than the spin diffusion length $l_{SD}$ (which is valid for a wide range of metals), macroscopic transport equations are obtained relating current densities to electrochemical potentials. These macroscopic equations are used to develop the analysis of a variety of cases. For the simple case of two semi-infinite magnets in contact with zero interface resistance, it is observed that over a length of $l_{SD}$ on both sides of the interface the electric field increases exponentially and the current asymmetry between up and down spins is greatly reduced. Furthermore, the reversal of the magnetization of one of the layers introduces a voltage drop, giving rise to an interface resistance with the same expression as that obtained by Johnson [206]. However, for the case of a multilayer, Johnson's formulation is only obtained in the limit where the spacing layers' thickness $t$ is much larger than the spin diffusion length. For the case of practical interest ($t \ll l_{SD}$), the interference between spin accumulation at successive interfaces leads to a significant decrease in the amplitude of MR by the factor $t/l_{SD}$.

---

[30] Spin accumulation is the build-up of magnetic moments (of spin) at an interface, similar to the build-up of charge.

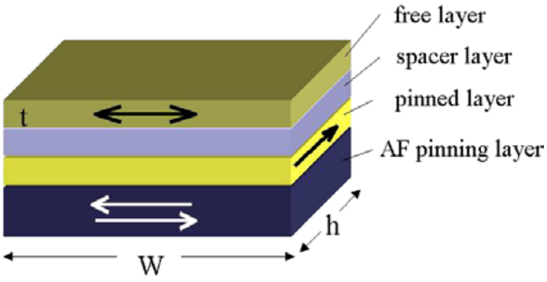

**Figure 41.** Schematic diagram of a simple four-layer spin valve structure.

The equations for the interface coupled resistances per unit area in the parallel and antiparallel cases,

$$
\begin{aligned}
R^{(P)} &= 2\beta^2 \frac{\rho_N \rho_F}{\rho_F \coth(t_N/2l_{SD}) + \rho_N \coth(t_F/2l_{SD})} l_{SD}, \\
R^{(AP)} &= 2\beta^2 \frac{\rho_N \rho_F}{\rho_F \tanh(t_N/2l_{SD}) + \rho_N \coth(t_F/2l_{SD})} l_{SD}
\end{aligned}
\tag{74}
$$

where $\rho$ is a factor expressing the spin-dependent bulk scattering and the subscripts $N$ and $F$ refer to the normal metal and the ferromagnetic layers respectively, clearly show the dependence on the spin scattering length. Even when a more complete analysis is performed by solving the Boltzmann equation with spin-dependent bulk and interface scattering [208, 209] and taking account of the two conduction channels (depending on the density of states) of 3d metals, the physics remains essentially the same as that shown in equation (74). This simple model describes the main features of magnetoresistive multilayers i.e.

(i) increase in MR with decreasing temperature,
(ii) increase with decreasing film thickness and
(iii) increase with increasing number of layers.

### *5.5. Methods for obtaining differential switching of magnetization*

There are three techniques used to engineer GMR systems such that the two ferromagnetic layers in the multilayer switch differentially in an externally applied field. The first one involves choosing the metallic interlayer thickness (≈1 nm) such that the Ruderman–Kittel–Kasuya–Yoshida (RKKY)[31] coupling via the conduction electrons forces the magnetic layers to be antiferromagnetically coupled. This causes the layers to anti-align in zero applied field, but align parallel to one another in applied field [210]. In a series of theoretical works, Costa *et al* [211–214] gave some insight how to choose the interlayer thickness. The oscillatory periods of the interlayer exchange coupling $J_{(N)}$ ($N$ is the number of non-magnetic layers) are related to the geometry of the Fermi surface of the spacer. Different extrema of the Fermi surface contribute with long or short period oscillations, which combined give the characteristic coupling for each type of multilayer. The degree of confinement imposed on the electrons at the extrema by the ferromagnetic layers also plays an important role. This approach was also proposed by Bruno and Chappert [215], and the results are in good agreement with Johnson's

---

[31] The RKKY interaction exchanges magnetization information between localized moments via the conduction electrons of the host material. The essential ingredients are a localized spin-polarized perturbation and a sharp Fermi surface leading to the coupling oscillations.

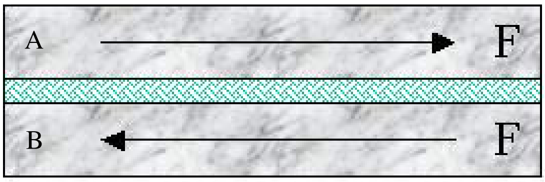

**Figure 42.** Schematic diagram of an artificial antiferromagnet.

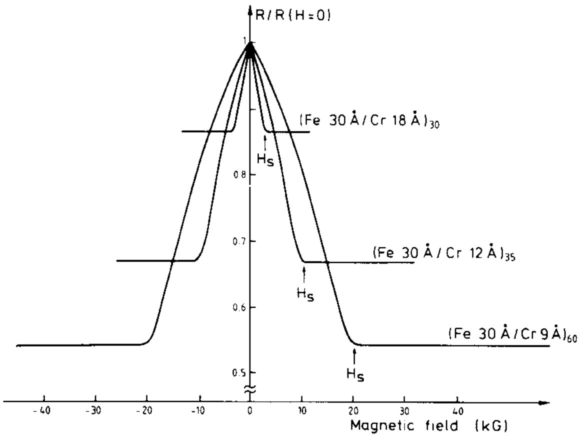

**Figure 43.** Magnetoresistance of Cr/Fe multilayers measured at 4.2 K. (From [192].)

work (see section 5.6). However, this technique imposes constraints on the device design which may not permit the best GMR signal.

The second technique is to fabricate one layer magnetically harder by exchange pinning it to an antiferromagnet on the side opposite of the GMR device. In this case only the unpinned soft layer moves in small magnetic fields. The resulting device is termed a spin valve (figure 41) [216].

The third technique involves using materials known as artificial antiferromagnets (AAFs), which combines the above two ideas. RKKY coupling is not used in the GMR spacer layer, but one of the ferromagnetic electrodes is rendered magnetically hard by fabricating it from two distinct ferromagnetic layers A and B (figure 42) of almost identical thickness. These layers are magnetically coupled such that in zero applied field they are antiparallel and hence their net moment is small. The switching field of this AAF block (A + B) is thus enhanced by a '$Q$-factor' which is the ratio of the total magnetic moment when A and B are aligned in a high field to the net moment when A and B are anti-aligned [217].

### *5.6. GMR materials studied*

The breakthrough for spin electronics arrived with the measurement of the first magnetic-field-dependent change in the resistance of metallic multilayers of Fe/Cr in 1988 [192, 218]. Baibich *et al* [192] found that when the thickness of the non-magnetic Cr layers is decreased below 20 Å, the Fe layers are coupled antiferromagnetically. With an applied magnetic field, the magnetization of the Fe layers gets progressively more aligned and the resistance of the structure decreases. GMR multilayers with around 30 Fe/Cr layers showed changes of resistance of up to 50% at 4.2 K in a magnetic field of 2 T (figure 43). This value is halved when measured at room temperature.

**Table 2.** GMR dependence on the thickness of Cr layer.

| Reference | Temperature (K) | $t_{Fe}/t_{Cr}$ | Number of bilayers | MR% (field) |
|---|---|---|---|---|
| [209] | 4.2 | 30/9 | 40 | 50 (2 T) |
| [209] | 4.2 | 30/18 | 30 | 15 (0.5 T) |
| [209] | 4.2 | 30/12 | 35 | 35 (1 T) |
| [209] | 4.2 | 30/9 | 60 | 50 (2 T) |
| [209] | 300 | 30/9 | 60 | 25 (2 T) |
| [212] | 300 | 120/10 | 1 | 1.5 (0.04 T) |
| [212] | 300 | 80/10 | 2 | 3 (0.04 T) |
| [212] | 5 | 80/10 | 2 | 10 (0.04 T) |
| [217] | 4 | 30/10 | 100 | 20 (0.5 T) |
| [217] | 4 | 33/16 | 100 | 11 (0.4 T) |
| [217] | 4 | 33/28 | 100 | 5 (0.3 T) |

The antiferromagnetic coupling (see section 5.5) between the magnetic layers has its origin in a RKKY type potential [219] increasing exponentially for thicknesses below 30 Å. Thicker Cr layers will give rise to weaker AF or FM interlayer coupling which in turn decreases the MR magnitude. Parkin *et al* [210] found an oscillatory behaviour of the magnetic coupling of Fe/Cr, Co/Cr and Co/Ru multilayers. Systematic measurements of the strength of the exchange coupling have been carried out by Celinski and Heinrich [220] for Fe/Cu, Pd, Ag and Au/Fe trilayers using GMR and surface magneto-optical Kerr effect. The results vary depending on the materials. For the Cu case, the exchange coupling was found to oscillate, but with only one crossover to antiferromagnetism at around 8 Cu monolayers (ML). Above that, the layers remained antiferromagnetic. For Ag, the ferromagnetic coupling decreases quickly with increasing thickness and vanishes altogether for thicknesses above 7 ML. The behaviour is similar for Au although a small antiferromagnetic minimum is present at 13 ML. Systematic measurements by Johnson *et al* [221] on fcc(100) Co/Cu/Co and bcc(100) Fe/Cu/Fe with a wedge-shaped Cu layer yields a series of rapid oscillations (periods of 2.6 and 2.0 ML respectively). An additional 8 ML period was observed in the fcc case.

Many other multilayer systems have been studied using the CIP geometry. Apart from extensive measurements on Fe/Cr multilayers [214–217] there are reports on Co/Cr [218], Co/Cu [219, 220], Fe/Cu [221], Ag/Ni [222], Co/Ag [223], Ni/Ti and NiC/Ti [224], $Co_9Fe$/Cu and $Co_3Fe$/Cu [225], sandwich layers of $Ni_{81}Fe_{19}$, $Ni_{80}Co_{20}$ and Ni separated by Cu, Ag or Au [213, 226] and the natural multilayer FeRh [227]. The effect can also be observed in granular alloy systems such as Co–Ag, Fe–Ag, Fe–Cu and Fe–Au [228] by alignment of randomly oriented ferromagnetic spins in a metallic matrix. Table 2 shows some results obtained on Fe/Cr multilayers in order to highlight the influence of Cr thickness and temperature on the GMR values. The influence of the thickness of the non-magnetic layer in the value of GMR is twofold:

(a) it defines the sign and magnitude of the exchange coupling and
(b) for thicknesses of the order of the spin diffusion length it can depolarize the current.

### 5.7. GMR devices

The technological potential of this effect has been realized with great success in the computer industry with the introduction by IBM of the GMR read–write head in hard disks in 1997. The new GMR heads are two to three times more sensitive than their predecessors—magnetoresistive heads based on AMR—allowing for a larger data storage density in the hard drive (100 Gb/in$^2$) [222]. This type of device could also be very important where information storage is concerned given that it would allow the fabrication of non-volatile memory elements where the information could remain stored without the presence of an electrical current. Furthermore, GMR technology is now available commercially in a variety of magnetic field and motion sensors [223, 224].

### *5.8. Improvements to GMR*

The search is still on for even higher MR values in order to implement a host of technological applications. Equation (67) suggests that the efficiency of the GMR multilayer can be increased by using non-magnetic materials having large $\lambda_{mfp}$. Alternatively, the efficiency may also be improved by reducing the thickness of the non-magnetic layers so that the electrons travel between two electrodes without losing spin information. Furthermore, by introducing magnetic materials with high spin polarization, like the half-metallic ferromagnets[32] (including the manganese perovskites—see section 5.2), the current is expected to be effectively blocked for antiparallel spin alignment, leading to a very high magnetoresistance.

## 6. Other experimental systems exhibiting MR

This section combines magnetoresistance with the energetics of domains and domain walls. The first, magnetic nanocontacts, generate DW-MR (see section 5.2.5) by trapping the domain wall in a nanoconstriction so that any current flowing through is subject to the spin precession length. Current induced switching (CIS) operates by applying a spin polarized current large enough to generate a local magnetic field that will switch the magnetization direction of the material. This phenomenon is clearly subject to the energy considerations of domain formation (see section 2.2.2) and, therefore, the characteristic length scale of CIS is the exchange length.

### *6.1. Magnetic nanocontacts*

Magnetic nanocontacts have stirred a great deal of interest because of the high values of MR reported in low magnetic fields. This results from the quantization of the energy in these narrow structures in a similar fashion to that of an electron in a square potential well. Therefore, as the lateral dimension of the contact is decreased, the energy of the sub-bands is pushed above the Fermi energy, closing the corresponding channel. Since each sub-band carries the same amount of charge, the conductance decreases in steps of $e^2/\pi\hbar$. More formally, the point-contact conductance $G$ for ballistic transport is given by [225, 226]

$$G = e^2 N_0 a(\hbar/2m)\langle|k_x|\rangle \tag{75}$$

where $N_0$ is the density of states of the two-dimensional electron gas, $a$ is the width of the constriction and the brackets represent an average of the longitudinal wavevector $k_x$ over specific directions on the Fermi circle. The average is taken over discrete transverse wavevectors leading to a wire conductance given by

$$G = \sum_{n=1}^{Nc} \frac{e^2}{\pi\hbar} \tag{76}$$

where $N_c$ is the number of sub-bands contributing to the conduction.

---

[32] Half-metallic ferromagnets, or HMFs, have zero density of states for the minority spin carriers, so they can only conduct half of the carriers—the majority spin carriers.

The transport properties of nanocontacts have been studied in two-dimensional electron gases in gated semiconductor heterostructures [225], microfabricated break junctions [227], scanning tunnelling microscopy (STM) and related techniques [228–232], macroscopic wires [233] and relays [234]. Quantized conductance was first observed by van Wees *et al* [225] in the two-dimensional electron gas of GaAs–AlGaAs heterostructures, where the width of the point contacts is defined by depletion of the electron gas from a voltage applied to a gate electrode. van Wees *et al* observed an increase in the conductance in well defined steps corresponding to integral multiples of $e^2/\pi\hbar$, exactly as predicted.

Garcia *et al* [235] reported the first transport measurements (see figure 44 for the experimental set-up) on magnetic nanocontacts on two Ni crystals, demonstrating that the conductance through the nanocontact formed by two wires depends on the relative orientation of the magnetization of the wires. The nanocontact was made by contacting the rounded tips of two Ni wires 2 mm in diameter and applying a voltage to the ends of the wires until a current was observed. The wires were tightly bound to a Teflon tube with resin to give rigidity to the structure. Two coils, one at the end of each wire, set the magnetization of each wire. The current through the nanocontact and the coils is monitored on the two channels of an oscilloscope.

When no current is applied to the coils, the current through the nanocontact is constant. When a square wave is applied to coil 2 (to alternate the magnetization of wire 2) and a constant current is applied to coil 1 (to fix the magnetization along the axis of the wire), steps in the conductance of the nanocontact are observed which correspond to a switch of the relative orientation of the magnetization of the two wires (figure 45). Magnetoconductances of 280% at room temperature and 20 Oe can be obtained. It was also observed that the magnetoresistance decreases as the contact size increases. In order to prove that this conductance has a magnetic origin, the same experiment was performed with Ni–Cu and Cu–Cu nanocontacts and no variation of conductance with magnetic field was observed.

The above magnetoconductance results were explained on the basis of spin-dependent scattering at the domain wall [235–237]. In bulk materials where the domain wall width is much larger than the Fermi wavelength $\lambda_F$, the electron spin can adiabatically accommodate the change in magnetization as it travels through the domain wall and therefore the measured magnetoresistance is small. However, in a nanocontact, the domain wall width is much smaller than the spin scattering length [237] and the electron crosses the wall without changing its spin. Therefore, it will be scattered according to the density of states configuration on the other side of the domain wall. Nanocontact materials can then be chosen according to the ratios $r = D_\uparrow/D_\downarrow$ (where $D_\uparrow$ and $D_\downarrow$ represent the spin-up and spin-down density of states at the Fermi level) and $b = \lambda/l_{SD}$ (where $\lambda$ is the domain wall width and $l_{SD}$ the spin diffusion length). Optimal results are obtained for Ni with its large value of $r = 13$. Measurements on Fe ($r = 3$) nanocontacts show maximum MR values of only 25% [238]. Nanocontacts of half-metallic ferromagnets, where $r = \infty$ in theory, should show very large values of magnetoresistance. Quantized steps in conductance have been observed in $(La_{0.7}Sr_{0.3})MnO_3$ [239], but the measured room temperature MR is only 16% at 100 Oe. In $Fe_3O_4$, another half metal, a value of 85% at 7 mT at room temperature was observed [240].

### 6.2. *Current induced switching*

It has been seen from the discussion on GMR (section 5.2.3) that spins can be scattered differently depending on the relative orientation of the magnetic moments of the layers. Slonczewski [241] was the first to suggest that the reverse effect should be expected as well, i.e. that a spin polarized current could affect the magnetic moment of a layer, called current

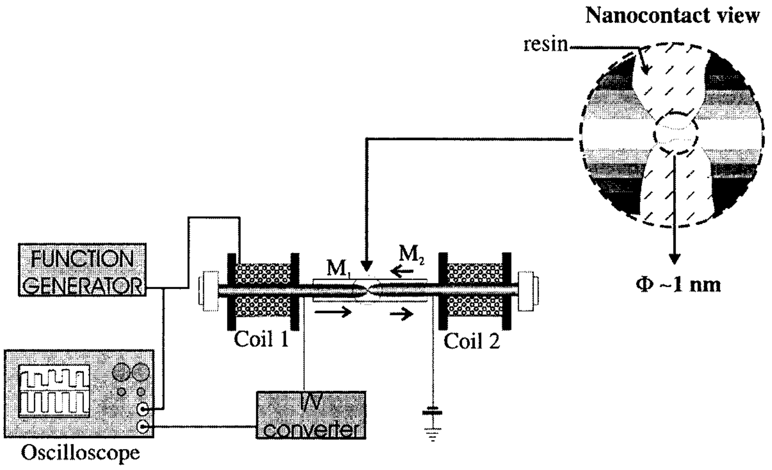

**Figure 44.** Experimental set-up for measuring magnetoresistance of nanocontacts. (From [235].)

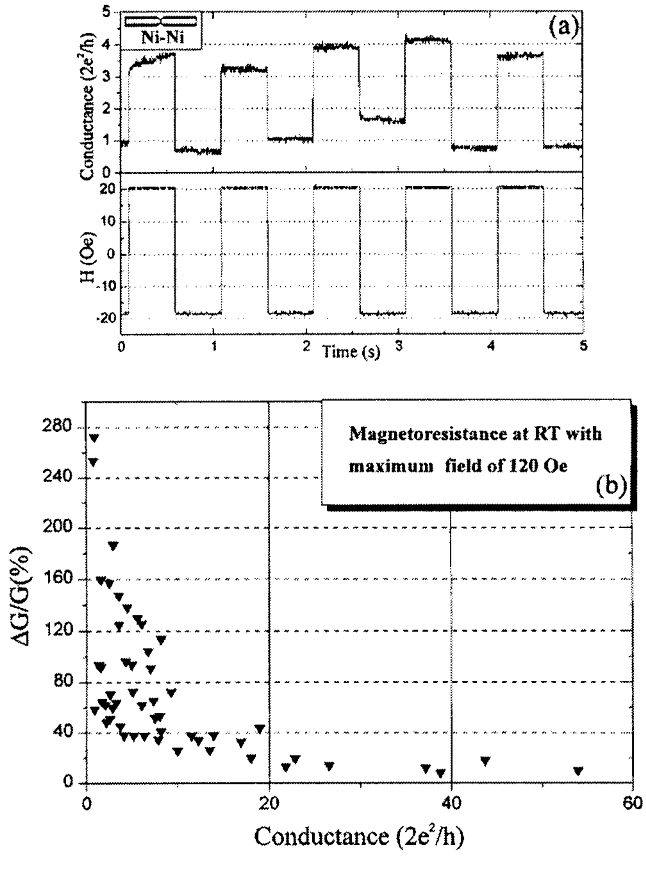

**Figure 45.** (a) Conductance variation of Ni nanocontacts with applied magnetic field. (b) Magnetoresistance at room temperature of the Ni contacts. (From [235].)

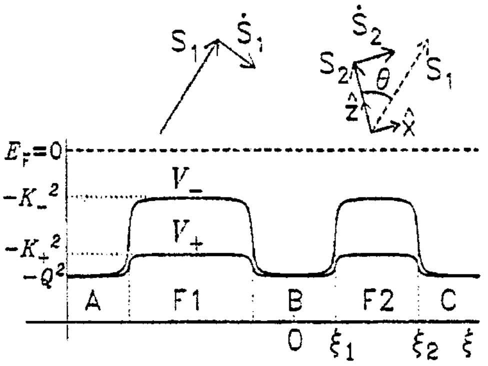

**Figure 46.** Bottom: Coulomb plus the locally diagonalized exchange potential $V_{\pm}$ versus position $\xi$ in a five-layer system composed of paramagnets A, B and C and ferromagnets $F_1$ and $F_2$. The particle flow is towards the right and the charged flow to the left ($I_e > 0$). Top: vector diagram of spin moments $S_{1,2}$ and their current-driven velocities $S_{1,2}$ for magnets $F_{1,2}$. Reprinted from [241] with permission from Elsevier Science.

induced switching (CIS). Other theoretical contributions include the works of Berger [242] on the interaction between spin waves and itinerant electrons and Bazaliy *et al* [243] on the magnetization behaviour of a ferromagnet in the presence of a spin polarized current.

*6.2.1. Theory.* The underlying mechanism of CIS is the spin-dependent scattering of conduction electrons that occurs at a normal metal/ferromagnet interface. To illustrate this, the case of a five-layer structure (figure 46) is considered. In this structure, A, B and C are paramagnetic layers; $F_1$ and $F_2$ are the ferromagnetic layers; $S_1$ and $S_2$ are the respective magnetic moments of the layers at an angle $\varphi$ with respect to each other; $V_{\pm}(\xi)$ are the Stoner plus Coulomb exchange potentials of the magnet (where the subscripts ± refer to the majority/minority spin bands) and $\xi$ is a position coordinate in real space.

First, consider the three-layer system (B, $F_2$, C) where an electron with spin in the $S_1$ direction is incident on $F_2$ from layer B. The crucial observation is that the magnet reacts to the electron via conservation of angular momentum and changes its momentum by $\Delta S_2$, an amount equal to the sum of the inward spin fluxes from B and C. Averaging this spin transfer with respect to the direction of electron motion yields

$$\langle \Delta S \rangle = \frac{\sin\theta}{2}. \tag{77}$$

This is equivalent to the total absorption of the spin of the electron incident on $F_2$. Considering the case of total reflection of electrons with spin antiparallel to the moment of $F_2$, the spin transfer per transmitted electron can be calculated as

$$\Delta S_2 = \frac{\sin\theta}{2\cos^2(\theta/2)}. \tag{78}$$

Essentially, equations (77) and (78) combined describe the complete transfer of the transverse component of the incident electron spin due to $F_2$, except for geometrically dependent fluctuations.

The full five-layer system is treated by solving the Schrödinger equation for the two spin bands in the WKB limit and with a general value of $\theta$. Generally, ballistic transport is assumed, although for room temperature measurements the two-channel current model (see section 5.4) used in GMR is necessary. The spin transfer in each magnetic layer is then given by

$$\dot{S}_{1,2} = \left(\frac{I_e g}{e}\right)\hat{s} \times (\hat{s}_1 \times \hat{s}_2) \tag{79}$$

where $I_e$ is the current density of charge, $\hat{s}_1$ and $\hat{s}_2$ are unit vectors in the direction of $\boldsymbol{S}_1$ and $\boldsymbol{S}_2$ respectively,

$$g = [-4 + (1 + P)^3(3 + \hat{s}_1 \cdot \hat{s}_2)/4P^{3/2}]^{-1} \tag{80}$$

and the spin polarization $P$ is

$$P = \frac{N_+ - N_-}{N_+ + N_-}. \tag{81}$$

We can immediately see from equation (79) that a spin polarized current flowing from the left will tend to align $S_2$ along the direction of $S_1$. But we can also see that the reflected current flowing back into $F_1$ from the right will cause a torque on $S_1$ in the same direction as that applied to $S_2$: the two moments turn in the same direction. It is also clear that the moments can be made to align parallel or antiparallel to each other depending on the direction of the applied current.

In practical terms, inducing this magnetic excitation mandates that the torque overcome exchange, anisotropy and damping effects, which, in the spin transfer theory outlined above, requires high current densities—on the order of $10^7$–$10^9$ A cm$^{-2}$. This can be achieved with a point-contact geometry (described in section 6.1). Overall, magnetic switching has the advantage of allowing for very localized control of magnetic domains without recourse to long-range magnetic fields. Furthermore, this effect places a limit on the amount of current that can be used to adequately measure GMR devices.

*6.2.2. Experimental details.* Current induced magnetization excitations have been observed in a variety of magnetic systems. Tsoi *et al* [244] made the first observation on the magnetic multilayer system $(\mathrm{Co/Cu})_N$ where $20 < N < 50$. The excitation, observable as a peak in $\mathrm{d}I/\mathrm{d}V$ as a function of $V$, is associated with the excitation of a spin wave, which forces a reduction in the magnetization of the layers. A similar effect was also detected in the all-oxide barrier of $(\mathrm{La_{0.7}Sr_{0.3}})\mathrm{MnO_3/SrTiO_3/(La_{0.7}Sr_{0.3})MnO_3}$ [245]. A low temperature hysteretic $I$–$V$ curve with a step corresponding to an increase in the resistance of the structure was interpreted as an exchange of angular momentum between a spin polarized current and a magnetic cluster located between the electrodes. Wegrowe *et al* [246] observed room temperature magnetization reversal in Ni nanowires.

Probably the most clear cut experiment showing magnetization reversal is that of Myers and co-workers [247] using a five-layer structure as depicted in figure 47. The Cu spacer between the Co layers is made thick enough (4 nm) so that there is little exchange between the magnets. The Cu layer on the left makes a point contact on the Co free layer in order to achieve higher current densities. Figure 48 shows the results obtained at 4.2 K and zero magnetic field for free layers of different thicknesses. It can be seen that above a certain current, the differential resistance develops hysteresis corresponding to the switching of the moment of the thin Co layer. In this particular configuration a positive bias current induces antiparallel alignment characterized by the upward step of the differential resistance. As the bias current is swept back to negative values the system remains in the high resistance branch until, at large enough negative bias, parallel alignment is induced and the system returns to its low resistance state. The resistance variation is in the range 3–5% and it vanishes at room temperature.

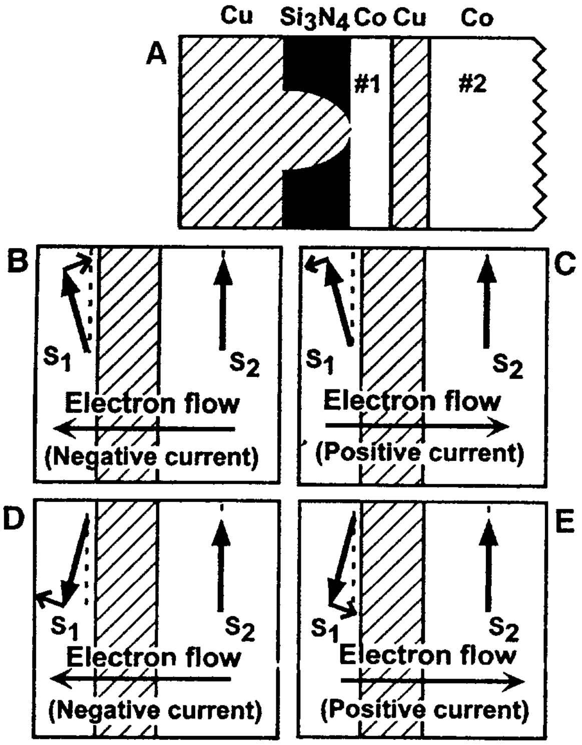

**Figure 47.** Schematic representation of the five-layer structure used to measure current induced switching (A) and the torque induced in the moment of the thin layer for each current direction (B)–(E). (From [247].)

## 7. Tunnelling magnetoresistance

The seventh example of mesomagnetism is tunnelling magnetoresistance. This phenomenon combines quantum tunnelling with 'magnetoresistance'. In this case, the defining characteristic is the thickness of the tunnel barrier, not the spin diffusion length. The barrier must be engineered on the scale of a few nanometres so that a measurable current from quantum tunnelling can occur.

### 7.1. *Quantum tunnelling*

If a potential is applied between two conducting layers separated by a thin insulating film, an electrical current passes between the metal electrodes by quantum mechanical tunnelling of the current carriers through the barrier (figure 49(a)). The tunnelling rate for carriers of a particular energy is proportional to the product of the carrier densities of states at that energy on each side of the barrier. Also, the thinner the barrier and the lower the barrier height, the larger the current is. The thickness of the tunnel barrier must be in the low nanometre regime to obtain reasonable current densities. This phenomenon was extensively studied in the context of superconducting thin films where it enables accurate determination of the superconducting energy gap [248].

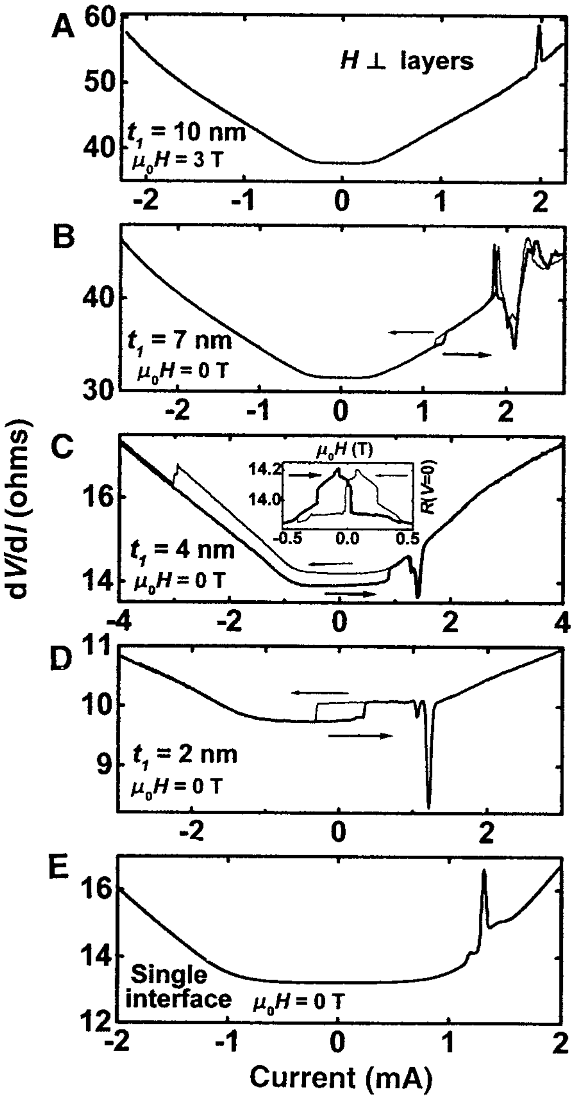

**Figure 48.** Differential resistance at 4.2 K of Co/Cu/Co sandwich devices for different values of thickness $t_l$ of the Co free layer. (From [247].)

### *7.2. Spin tunnelling*

Spin tunnelling is analogous to quantum tunnelling, except that instead of metallic electrodes, ferromagnetic electrodes[33] are used (figure 49(b)). They exhibit (figure 50) large changes in tunnel resistance depending on the relative alignment of the magnetizations of the ferromagnetic electrodes. This effect is called tunnelling magnetoresistance (TMR) and may be understood, at least simplistically, by Julliere's model [250] which was inspired by the ideas of Merservey and Tedrow [252].

---

[33] This was first investigated by Julliere [250] and Maekawa and Gafvert [251], who showed that the tunnelling conductance (for these dissimilar electrodes) increased when the relative orientation of the electrodes changed from parallel to antiparallel.

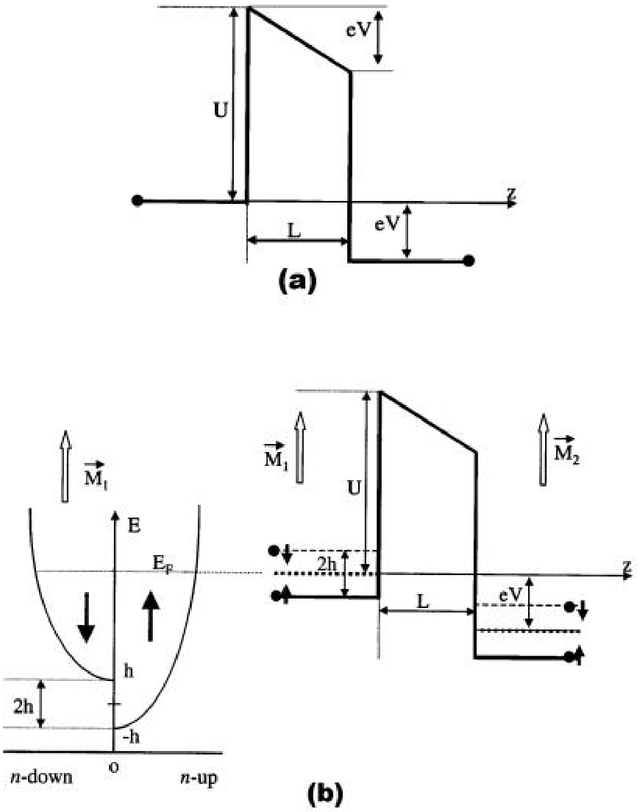

**Figure 49.** (a) Quantum tunnelling between two metallic electrodes separated by an insulating barrier. (b) Spin tunnelling between two ferromagnetic electrodes separated by an insulating barrier. (From [249].)

### *7.3. Theoretical description of spin tunnelling*

*7.3.1. Classical theory of tunnelling—Julliere's model.* Julliere's classical description for this effect is that the spin splitting of the Fermi level in the magnetic metals causes an unequal distribution of up- and down-spin electron states. This, combined with the classical model of tunnelling [254] which states that the overall tunnelling conductance is proportional to the product of the densities of states of the two electrodes assuming that spin is conserved in the process of tunnelling, resulted in a simple formula which stated that

$$\frac{\Delta R}{R} = \frac{(R^P - R^{AP})}{(R^P + R^{AP})} = \frac{2P_1P_2}{(P_1 + P_2)} \tag{82}$$

where $P_i$ is the polarization of the $i$th electrode defined as

$$P_i = \frac{D_i^{\uparrow} - D_i^{\downarrow}}{D_i^{\uparrow} + D_i^{\downarrow}} \tag{83}$$

where $D$ is the density of states.

In the simple case of half-metallic ferromagnet electrodes whose magnetic moments are anti-aligned, it is clear that the product of the initial and final densities of states is zero for either spin type and no current flows. However, if the moments are aligned, the half-band of majority

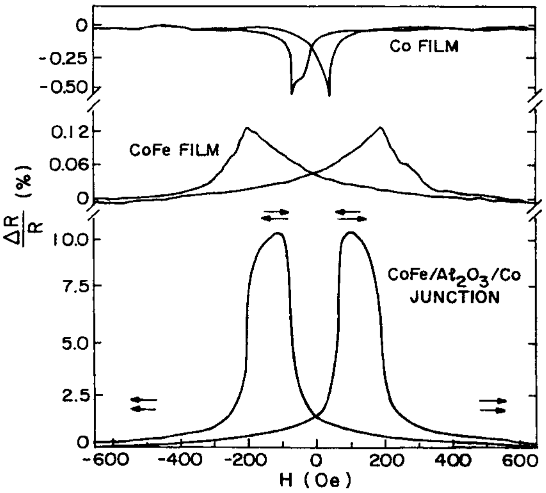

**Figure 50.** Experimental signature of spin tunnelling; resistance of CoFe/$Al_2O_3$/Co tunnelling junction plotted as a function of $H$ in the film plane, at 295 K. Also shown is the variation of CoFe and Co resistances. The arrows indicate the direction of $M$ in the two films. (From [253].)

spins may tunnel and the device has low resistance. It may be seen that this device, called a spin tunnel junction (TJ), is analogous to the CPP-MR trilayer except that it relies exclusively on asymmetry in density of states and does not invoke mobility spin asymmetry. This makes analysis cleaner and also means that, in general, the MR effects are larger than for GMR devices, which rely on asymmetry in both the density of states and mobility. Furthermore, the parameters of a TJ are more readily adaptable to practical applications.

*7.3.2. Slonczewski's model.* The basic defect in the classical theory of spin tunnelling is that it treats the two ferromagnetic electrodes as independent systems. In Julliere's model, the electron wavefunctions within the barrier are treated as evanescent and are assumed to not perturb the electron wavefunction in the other electrode. It also considers only the simple case of a square barrier—i.e. one that is unbiased, or at least where the effect of the bias voltage on the barrier shape may be ignored. As a result, this early model does not predict any barrier width or height dependence of the tunnelling magnetoresistance, in clear contradiction to the measured results[34]. The necessity of modifying Julliere's model was first realized by Slonczewski [255], who argued that because most practical barriers are relatively permeable, the wavefunction overlap within the barrier means that wavefunction matching must be considered across the entire device. Using two parabolic bands (spin up and down) shifted relative to one another by the exchange splitting, Slonczewski solved the Schrödinger equation for the wavefunctions of the polarized electrons tunnelling across a rectangular barrier and determined the resulting conductance from the current operator. The principal result of his calculation was that the effective polarization of the tunnelling electron (which when substituted into equation (82) gives the TMR) now depends on the height of the barrier $V_b$ through an imaginary wavevector in the barrier $\kappa$ defined by

$$\hbar\kappa = \sqrt{[2m(V_b - E_F)]} \qquad (84)$$

---

[34] For instance, in a classic experiment by Moodera and Kinder [253], it was found that the observed TMR is largely dependent not only on the type of insulator used as a TJ, but also the barrier height and width.

by an amount:

$$P = \left[\frac{k_\uparrow - k_\downarrow}{k_\uparrow + k_\downarrow}\right]\left[\frac{\kappa^2 - k_\uparrow k_\downarrow}{\kappa^2 + k_\uparrow k_\downarrow}\right]. \tag{85}$$

This equation has a simple physical interpretation: since the magnitude of the Fermi wavevector for a particular spin channel is proportional to the density of states at the Fermi energy, we can see that the first factor $(k_\uparrow - k_\downarrow)/(k_\uparrow + k_\downarrow)$ is identical to the polarization obtained in Julliere's classical theory of tunnelling, but is now multiplied by a new factor $(\kappa_2 - k_\uparrow k_\downarrow)/(\kappa_2 + k_\uparrow k_\downarrow)$. Since $\kappa$ ranges from zero (low barrier) to infinity (high barrier) we can see that in the limit of high barrier height the effective polarization reduces to Julliere's result; however, for low barrier height it departs significantly and can even change sign. Hence the matching of the wavefunctions across the tunnel barrier offers a plausible explanation for the observed dependence of TMR on the thickness and height of the tunnelling barrier, and hence on the choice of insulator itself.

*7.3.3. Fowler–Nordheim tunnelling regime.* An additional sophistication, which may be added to both the Julliere and Slonczewski models is the replacement of the simple square barrier with a triangular topped barrier whose shape more accurately reflects the applied bias across the TJ. This has the effect that the tunnelling electron wavefunction in the barrier becomes an Airy function rather than a simple evanescent wave. The circumstances in which this modification is necessary (i.e. when the bias potential term is not small compared with the barrier height) is termed the Fowler–Nordheim tunnelling regime. The Fowler–Nordheim regime manifests itself experimentally as non-linearity in the current/voltage curve for the TJ.

*7.3.4. Linear response theory.* Although Slonczewski's model provides a much more realistic treatment of the ferromagnet/insulator/ferromagnet (F/I/F) interface than the classical theory of tunnelling, its drawback is that it cannot be readily extended to complex systems with more than one electron band. Any rigorous model of TMR, however, has to include, or at least justify the exclusion of, the multi-orbital structure of ferromagnetic electrodes. It is for this reason that a great majority of the work undertaken in explaining TMR over the last decade has been based on the linear-response theory of electron tunnelling.

The main assumption of this theory (often referred to as the Kubo/Landauer formalism) is that the overall conductance in either spin channel for any (insulating or conducting) sample sandwiched between two electrodes can be written in terms of its total transmission coefficient [256]. The expression for the conductance in either spin channel can be written in terms of the one-electron Green functions in the left-and right-hand planes of the tunnelling junction, in a direction parallel to the current flow [257]

$$G^\sigma = \frac{4e^2}{h}\sum_{k_\parallel}\mathrm{Tr}([\boldsymbol{T}_\sigma\,\mathbf{Im}\,g^\sigma_R(E_F, k_\parallel)] \times [\boldsymbol{T}^+_\sigma\,\mathbf{Im}\,g^\sigma_L(E_F, k_\parallel)]). \tag{86}$$

The theory includes more essential components necessary to explain the observed effects than any earlier model. The Green functions for each of the $k$-states $\mathrm{Im}\{g_R,{}^{\sigma}_{L}\,(E_F, k_\parallel)\}$ (which are closely related to the densities of states) are multiplied by a matrix $T_\sigma$ whose elements indicate the strength of the tight binding hopping between atomic orbitals in the left-and right-hand planes. Furthermore, the matrix contains an element that is responsible for the evaluation of the dependence of TMR on the height and width of the tunnelling barrier, as will be shown below. Summation over the two-dimensional Brillouin zone and taking into account the different characteristics of the s, p and d orbitals yields an overall conductance.

As an illustration, the formalism can be simplified to evaluate the above equation for the case of coherent ($k_\parallel$ and spin conserved) tunnelling through a high barrier, assuming that the electrons originate from only one band. In this case, it is found that the current in each channel is then proportional to the product of the surface densities of states of the two electrodes (as in the classical theory of tunnelling), but the product is scaled by the denominator which describes the mutual interaction of the two electrodes due to overlap of the wavefunctions. Such a model has been used to perform numerical calculations on a structure chosen to resemble a junction with Co electrodes and the result (increasing TMR with increasing barrier height $V_I$, saturating when $V_I$ is of the order of the bandwidth of the electrodes) is in excellent agreement with recent experimental results of Sousa *et al* [258, 259]. The observed weak variation of TMR with the barrier thickness [260] can be explained by the model if we assume that most TMR experiments are performed in the high barrier regime.

By adding a fully realistic band structure for the ferromagnetic electrodes to the above model (i.e. by distinguishing between s, p and d orbitals), it is possible to test whether the Kubo/Landauer formula predicts the correct sign for the polarization of the tunnelling electrons. Two such calculations have been performed—one dealing with tunnelling between Co electrodes through a vacuum gap, one through a simple step barrier [261]. The results from the first study are particularly encouraging—the calculated polarization of the tunnelling electrons as a function of the tunnelling vacuum gap shows that, when the tunnelling gap is small, of the order of the lattice constant, the conductance is dominated by d electrons, and the polarization has the 'wrong' sign, i.e. $P < 0$ as in the classical Julliere theory of tunnelling. There is a rapid crossover, however, as the width of the gap increases, and the polarization changes to positive values. Moreover, the calculated saturation value of 35–40% TMR is in excellent agreement with the observed values [262]. The crossover occurs due to the fact that the overlap of the d orbitals decreases with the increasing gap much faster than that of s orbitals, and it is therefore s electrons which determine the conductance in most tunnelling experiments. One may therefore deduce that the observed sign of the polarization in junctions between ferromagnets and $Al_2O_3$ suggests that the sd hybridization between the two must be weak.

Going a step further in the Kubo/Landauer formalism, it is possible to consider the effect on the observed TMR of disorder or impurities in the barrier. In most tunnelling experiments the fabricated barriers are amorphous so the assumption of conservation of momentum parallel to the tunnelling junction ($k_\parallel$) is not satisfied. Advanced studies of the effect of disorder on spin tunnelling using a single-orbital tight binding model and the Kubo formalism show that, in addition to the mixing of the $k_\parallel$ channels, disorder also induces resonant tunnelling via localized electronic states [263–265]. These states are formed in the barrier in the presence of impurities or defects. Resonant tunnelling results in quasi-one-dimensional high conductance channels, which dominate the overall conductance when the degree of disorder is high and the barrier is thick [266]. It follows that the overall tunnelling current, and hence the TMR, is not only determined by the intrinsic properties of the densities of states of the ferromagnet, but also to a large extent by the properties of the insulator.

As a further test of this theory, it is useful to compare its predictions with the experiments performed by several workers [267, 268] in which a thin layer of non-magnetic metal is inserted between one of the ferromagnetic electrodes and the insulating barrier. According to the classical theory, as there is no spin asymmetry in one of the metal–insulator interfaces, no TMR should be observed, which contradicts the experimental findings. In fact, calculations using the Kubo formalism by Mathon and Umerski [269] predict that the TMR should oscillate with increasing thickness of the Cu interlayer in a Co junction with a vacuum gap. For a very thin interlayer this leads to a negative TMR. This effect can be explained by considering the Fermi surfaces of Cu and Co. For the majority spin electrons in Co the matching of the surfaces with Cu is good, whereas for the minority spins it is not. It follows that the majority spin electrons can easily cross the Co/Cu interface while the poor match for the minority spin electrons results in the formation of down-spin quantum well states in the Cu overlayer [270–272], whose loss of transport gives rise to a spin asymmetry of the tunnelling current, and hence to a non-zero TMR.

### *7.4. Problems and refinements in the understanding of spin tunnelling*

The simple Julliere model gives good insight into the physical basis of spin tunnelling, but is incapable of explaining the finer experimental detail. On the other hand, linear response theory is relatively successful in offering explanations for the many subtleties in the observed TMR effects. However, extensive research carried out over the last 20 years has posed new questions, some of which remain unexplained even today. The search for a comprehensive theoretical model for TMR that is answerable to all available experimental data is as yet an unresolved challenge.

One of the more challenging problems is the true origin of the fall in TMR with the increase in temperature and applied bias [273], irrespective of the junction quality. For the former, there are currently two possible explanations: one involves the mechanism of spin–flip scattering arising from magnetic impurities in the barrier [274], which, being an inelastic process, increases with temperature; the other suggests that the increase in temperature leads to a reduction of the overall magnetization in the ferromagnet due to excitations of magnons [275–277]. At this stage it is not clear to what extent each of these holds true. In a similar way, bias dependence can be accounted for by Slonczewski's model, although the initial decrease of TMR is much slower than observed [278]. An alternative explanation invokes electron–magnon scattering which (since magnons are spin-1 quasi-particles) flips the electron spin in the process [263]. Since the phase space for electron–magnon scattering increases with increasing bias, the total TMR decreases. Again, at present it is unclear to what extent these mechanisms are responsible for the observed behaviour.

Furthermore, the classical description suggests that a particular spin asymmetric material should always exhibit the same characteristic polarization for tunnelling processes and that this polarization value is closely related to and predictable from its bulk band structure. However, experiment reveals that, on the contrary, the polarization which magnetic electrodes manifest for tunnelling purposes is found to be a function of the magnetic metal/insulator combination, not just of the magnetic metal itself. The polarization of a particular spin electronic material may actually change sign depending on which insulator accompanies it [279]. The explanation is thought to be that the tunnelling electrons come from the first few atomic layers of the metal which are hybridized with the insulator and hence do not have the bulk band structure. Since spin electronic effects are almost all interface related, it is generally these interface band structures that are more relevant to practical device performance.

### *7.5. Spin tunnel junction—resistance and heat dissipation*

Spin TJs are characterized by a real conductance per unit area. The associated junction resistance scales, according to the very simplest theory, exponentially with thickness and barrier height. However, the net dissipation associated with this tunnel resistance when a tunnel current flows is not dissipated in the junction itself, but rather in the conducting material on its downstream side. Furthermore, hot carriers are injected into this region from the junction insulator and thermalize rapidly owing to their being high above the Fermi surface where there is a high density of empty states into which they may scatter.

### 7.6. *Coherent spin tunnelling—resonant structures*

Clearly, if two separate TJs are cascaded, their resistances add according to Ohm's law. However if the junctions are sufficiently close that the wavefunction of the electrons entering the first junction overlaps with those exiting the second junction—in other words the transport is ballistic in the layer separating the junctions—the analysis is more complex. Since the electrons have at least partially preserved their phase memory, they have not been properly thermalized in the intermediate layer and the concept of single-junction resistance is not valid. The entire multiple-tunnel structure must then be analysed as a single entity in similar fashion to how optical thin film interference filters are treated. Such resonant tunnel structures are potentially useful for making spin-tunnel devices with a high back-to-front electrical transmission ratio. The relevance of such considerations to quantum coherent spin electronics is discussed in section 8.2.

### 7.7. *Applications of spin tunnelling*

By analogy to the spin valve, the spin tunnelling junction acts as an electronic switch whose operation mirrors that of a pair of crossed optical polarizers which may be switched on and off by application of external magnetic fields. If the electrodes are not ideal HMFs, then the on/off conductance ratio is finite and reflects the majority and minority density of states for the ferromagnet concerned. Spin TJs as described have the added advantage that their operation depends only on the net properties at the interfaces and do not invoke carrier mobility. Therefore, unlike in GMR, there is no competition between these two effects. Moreover, unlike all metallic systems, they have lower conductances per unit area of device so larger signal voltages (of the order of mV or more) are realizable for practical values of operating current. The device characteristics such as the size of the 'on' resistance, current densities, operating voltages and total current may be tuned by playing with the device cross-section, the barrier height and the barrier width. In particular, spin tunnelling offers much greater flexibility in choosing the point in the electronic band structure where the spin injection is implemented. As we shall see below, this is just one reason why they are very promising candidates for the spin-injector stages of future spin electronic devices, including the next generation of tunnel MRAM[35].

## 8. Single electronics

Single electronics is electronics where only one electron forms the current. In order to control the passage of just a single charge, the system must be engineered to very specific dimensions. Exactly what the dimensions must be and how they are determined are outlined in the following sections.

### 8.1. *Coulomb blockade*

The electrostatic energy of a charged capacitor is

$$\frac{1}{2}\frac{Q^2}{C}. \tag{87}$$

If the capacitance $C$ is sufficiently small, this energy can exceed that of the prevailing thermal quanta of size $k_BT$, even for $Q = e$, the charge of an electron. Small metallic spheres or

---

[35] Tunnel MRAM is MRAM that uses a magnetic TJ and its TMR for conveying the magnetic orientation of the memory bit.

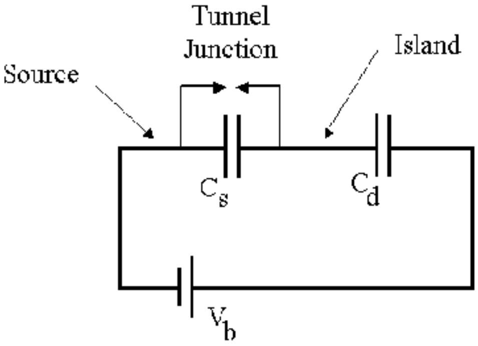

**Figure 51.** Single-electron box.

pads with physical dimensions in the nanometre range have capacitances in the right ballpark to obtain this condition [280]. If an electron now tunnels to such an island from an adjacent electrode under the influence of a small voltage bias, the variation of the island potential owing to the arrival of this excess electron may be large enough to react back on the tunnelling probabilities. When this negative feedback is capable of stopping further charge transfer, the result is known as Coulomb blockade.

### *8.2. Single-electron devices*

If such a metallic island (or a series of such islands) is sandwiched between two physically close metallic electrodes (the source and the drain), we have a device which, in principle, is capable of handling one electron charge at a time [281–283]. In practice, the self-capacitance of the metal island is negligible compared to its capacitive coupling to the adjacent electrodes and this latter defines the island capacitance for practical purposes. If the island–electrode separation is favourable, electron tunnelling may take place between them. Only three basic types—the single-electron box, the basic single-electron transistor (SET) and the turnstile—are considered here in order to give an overview of the behaviour which single-electron devices may be induced to display.

*8.2.1. The single-electron box.* We consider first the 'single-electron box' (figure 51) in which the left-hand (source) junction has a TJ in parallel with the junction capacitance ($C_s$), but the right-hand (drain) junction is perfectly insulating with a capacitance $C_d$. (Note that the subscripts indicate which junction is being referred to.) The applied voltage $V_a$ between the source and drain is distributed between the junctions in a way that is determined by the relative junction capacitances and the excess charge on the island. As $V_a$ is increased, more electrons tunnel through the source junction and charge up the island. The relevant free energy associated with this charging is

$$E = \frac{(Ne - C_d V_a)^2}{2(C_s + C_d)}. \tag{88}$$

This is plotted in figure 52 for different numbers $N$ of excess electrons on the island. Minimizing it shows that as $V_a$ is increased, the stable charge excess increases from $Ne$ to $(N + 1)e$ at values of

$$V_a = \frac{(N + 1/2)e}{C_d}. \tag{89}$$

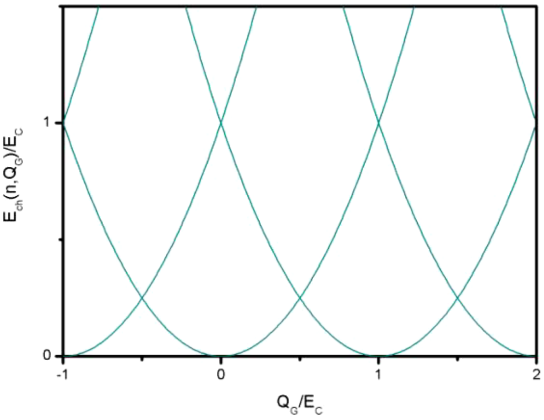

**Figure 52.** Stable charge configurations.

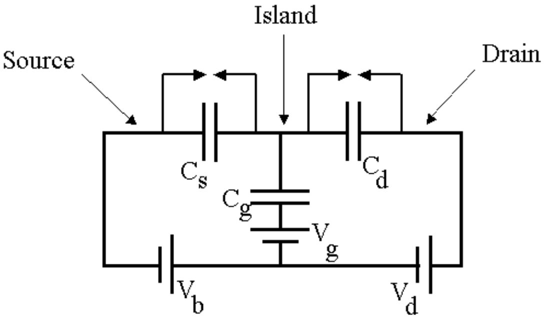

**Figure 53.** Single-electron transistor (SET).

*8.2.2. The single-electron transistor.* To convert an 'electron box' into a fully fledged SET, a tunnel junction is added in parallel with $C_d$ and a gate electrode is added which couples to the island via an additional capacitance $C_g$ (by which the island's total capacitance is now augmented). For simplicity, separate biasing is now introduced for each of the three electrodes, which are held at $V_s$, $V_d$ and $V_g$ respectively (figure 53).

Now, owing to introduction of the drain TJ, charge may transfer across the entire device. Depending on bias conditions it may do this and give rise to a continuous drain current, or the island may be Coulomb blockaded, in which case no current flows. Coulomb blockade arises if it is energetically unfavourable for the excess charge that has arrived on the island from the source to leave by tunnelling to the drain. Even in the presence of small positive source–island bias, the excess charge on the island Coulomb blockades the source junction so no further current may flow. To establish the conditions for Coulomb blockade we consider the incremental free energy of the system when the island excess charge is increased from $Ne$ to $(N+1)e$ :

$$\Delta E = E(N+1) - E(N) = \left[(N+1/2) - \frac{1}{e(C_g V_g + C_s V_s + C_d V_d)}\right]\left[\frac{e^2}{C_g + C_s + C_d}\right]. \tag{90}$$

This increment may be tuned by altering the gate voltage $V_g$. Figure 54 shows $\Delta E$ plotted for different values of $n$ and compared with the electrostatic driving energies $eV_s$ and $eV_d$. For an electron to transfer from source to island, $eV_s$ must exceed $\Delta E$: for an electron to transfer

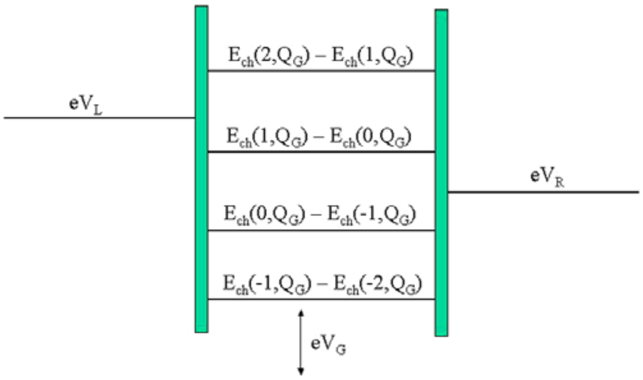

**Figure 54.** Plot of energy diagram for the SET.

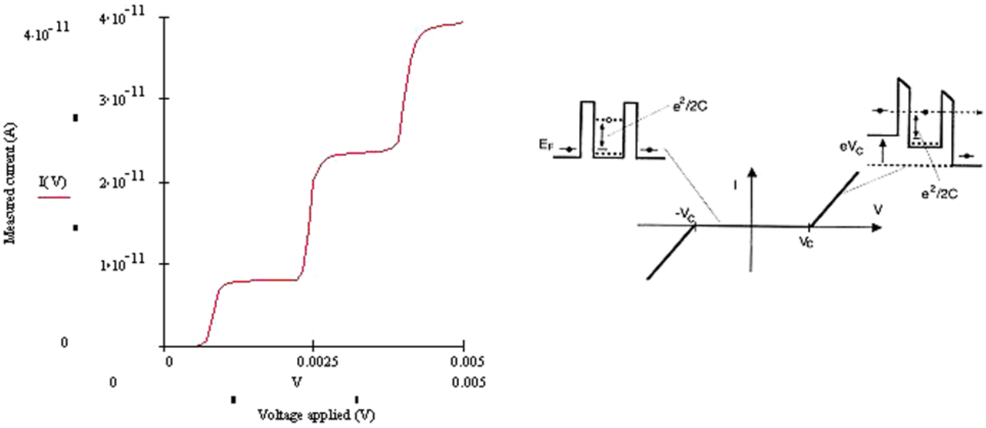

**Figure 55.** SET simulation.

from island to drain, $\Delta E$ must exceed $eV_d$. If $V_s + V_d$ is sufficient and $V_g$ is adjusted so that both these conditions obtain simultaneously, then the transistor passes current. The current may be stopped by adjusting the gate bias to violate one of the conditions. Therefore, at the threshold, the transistor is exceedingly sensitive to small changes in gate bias and, therefore, may make a very sensitive electrometer.

Pulsing the gate evidently causes charge packets to transfer as in a normal transistor. In the simplest case the electrons transfer one at a time for the duration of the gate pulse at a rate determined by the appropriate $RC$ time constant in the system, the resistances deriving from the TJs and the source impedance of the batteries. Increasing the driving voltage increases the stable charge excess on the island and causes increased currents as shown in the simulation of figure 55 (in which for simplicity the drain tunnel resistance has been set much larger than the source tunnel resistance) since more than one electron may now transfer per time constant $RC$.

In the Coulomb blockade regime, current may still flow by coherent co-tunnelling—a process in which electrons tunnel simultaneously and coherently through source and drain junctions thereby avoiding the Coulomb restriction. In order for co-tunnelling to be a serious perturbation, coherence between the successive junctions must be arranged: this will be suppressed if the tunnel resistances are considerably larger than the resistance quantum of 26 kΩ.

*8.2.3. The electron turnstile.* The third single-electron circuit is the single-electron turnstile, which consists of source and drain electrodes flanking three small islands, the central one of which is coupled to a gate electrode. Four TJs are implemented across the islands from source to drain. Unlike the basic SET which can be pulsed either on or off by the gate and which delivers a continuous current when 'on', the turnstile can deliver one electron each time the gate is pulsed in a direction determined by the polarity of the drain–source driving voltage. This additional discrimination is enabled by the fact that two locally stable charge configurations are now possible over a range of gate voltage.

*8.2.4. The ferromagnetic single-electron transistor.* The physics involved in single electronics is thus a competition between three energy terms: the electrostatic energy of the island ($E_i$) due to the presence of excess electrons, the energy $eV$ gained by an electron in falling through any of the various bias voltages and the thermal quantum $k_B T$ which should be small compared to the first two terms. However, when we combine single electronics and spin electronics, we introduce a fourth energy term into the problem, namely the electrochemical potential difference for spin-up and spin-down electrons associated with a spin accumulation. In practice this is achieved by making the electrodes and/or the island from ferromagnetic material [284–286] (see figure 56). A ferromagnetic source electrode will in principle produce a spin accumulation on a non-magnetic island and, under certain bias conditions, the associated electrochemical potential divergence holds the balance of power between the main energy terms and hence has a large degree of control over the current flow to the ferromagnetic drain. One could envisage that such a SET just below the Coulomb blockade threshold would exhibit high sensitivity to applied magnetic fields and moreover that a ferromagnetic turnstile could be similarly deployed to respond to very high frequency magnetic fields in a highly quantitative manner (see figure 57 and 58). Other configurations are possible in which the island is also magnetic. Fert and Barnas [287] have made extensive calculations for various temperature regimes of the various possible modes of behaviour of these devices, called ferromagnetic single-electron transistors (FSETs) or spin SETs. They are of particular interest to the experimental development of quantum computing since they offer a nice opportunity for the manipulation of spatially localized qubits (see section 9.4.3 for further details).

In the above discussion, the island was implicitly assumed to be sufficiently small that its electrostatic energy is capable of causing Coulomb blockade. Even smaller islands can be expected to display quantum well energy spectra where the energy gap between adjacent well states is non-negligible. In this situation, it is experimentally conceivable that, owing to the Pauli principle, an electrically neutral quantum well carrying a spin accumulation could have significantly higher energy than the same neutral island without spin accumulation. This effect could also be deployed as a means of making SET devices with high magnetic sensitivity.

### *8.3. Spin blockade*

Another interesting possibility, which arises if the magnetic island is itself a ferromagnet, is that of a spin blockaded system in which the electrical transport across the device is switched by magnetizing the island [288]. An example of a Schottky barrier at low temperature that has been spin blockaded in this fashion is shown in figure 59 [289]. 25% MR is observed at 20 K (figure 60)—a number unprecedented in a silicon device. The band structure consists of the Schottky barrier on the edge of which have been placed a series of magnetic islands which are antiferromagnetically coupled (figure 61), and hence blockaded, in zero applied magnetic field. Applying a field orients these superparamagnetic particles and the resistance of the structure decreases owing to a tunnel hopping current between adjacent islands. Exposure to

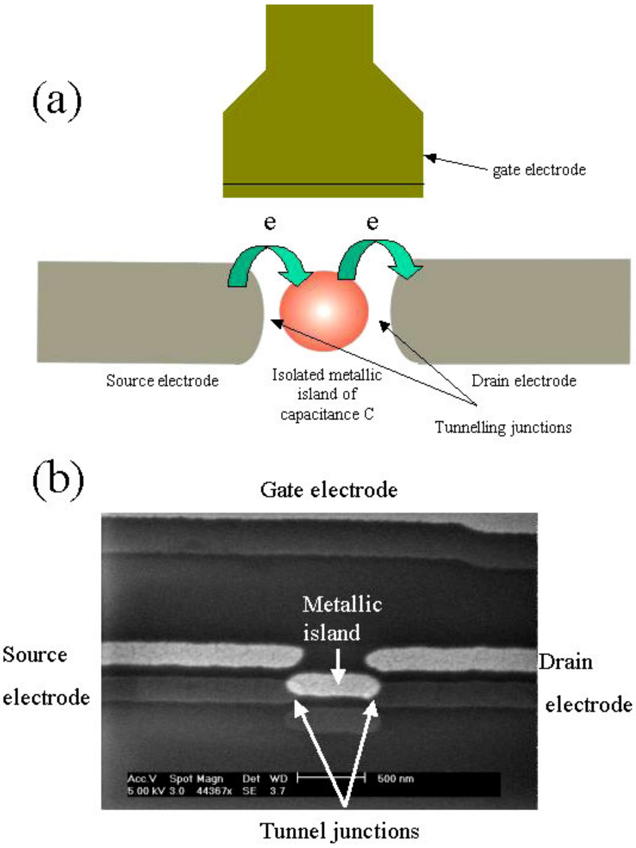

**Figure 56.** (a) Schematic diagram of an FSET and (b) the scanning electron microscope picture of the actual device.

light increases the resistance of the structure owing to photon promotion of electrons from the islands to the large density of adjacent surface states. The geometry of this system is not unlike that of a high electron mobility transistor (HEMT) in which the performance of the main current channel is controlled by localized states in an adjacent, but physically distinct region of the device.

## 9. Conclusions

In conclusion, mesomagnetism is characterized by a series of characteristic length scales. When the dimensions of magnetic systems are on a par with these lengths, new phenomena result. Some of these phenomena like magnetoresistance and magnetic TJs have already led to new technologies—read–write heads and MRAM, respectively. Others, like superparamagnetism, MQT and CIS define the fundamental limits of devices. (Superparamagnetism by how small you can make the particle and still have it operate at room temperature; MQT by how small you can make the particle and still have it operate at cryogenic temperatures; CIS by the amount of current that you can run through the system.) All of these systems offer tremendous potential for new applications, MQT and SETs as the qubit in a quantum computer and magnetic nanocontacts for even higher GMR materials. Furthermore, the most important control parameters are beginning to change, from macroscopic

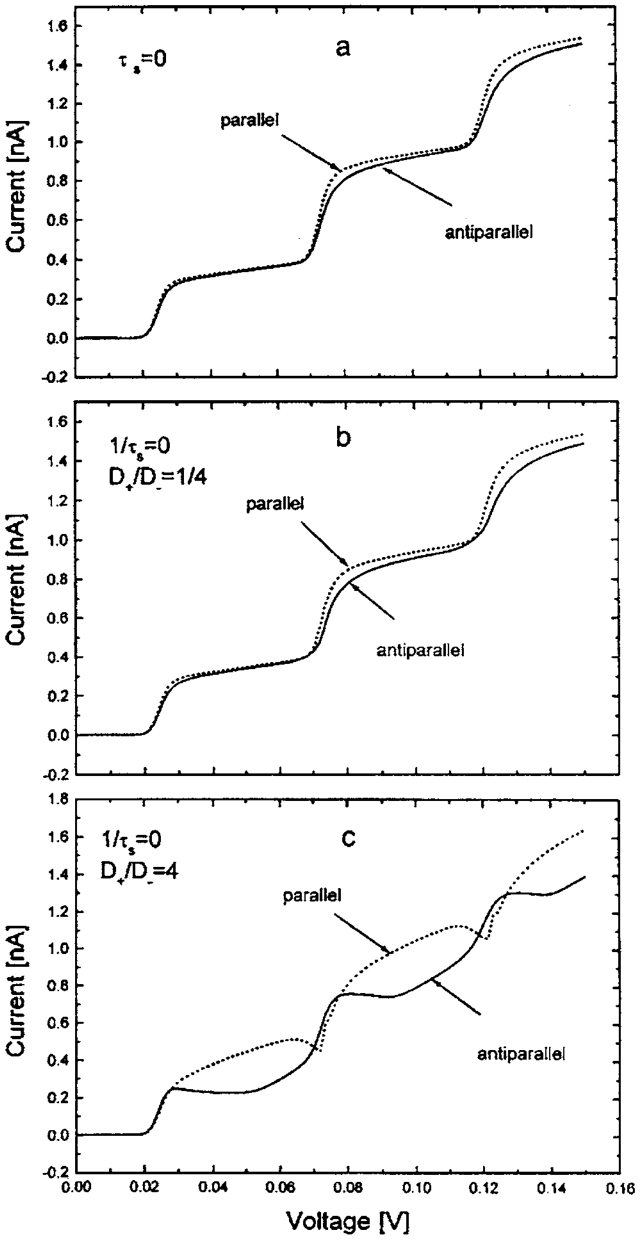

**Figure 57.** Left: I–V curves for parallel and antiparallel configurations in the limit of fast spin relaxation on the island (a) and in the limit of infinite spin relaxation time calculated for $D_+/D_- = 1/4$ (b) and $D_+/D_- = 4$ (c). (From [287].)

parameters like the material used, to microscopic parameters like control of the domain wall. This emphasizes the importance of the prediction and understanding of the local micromagnetic structure in confined systems.

Furthermore, all of the research focused on the area of spin electronics has served to illustrate an important point: spin electronic devices operate by transferring spin information

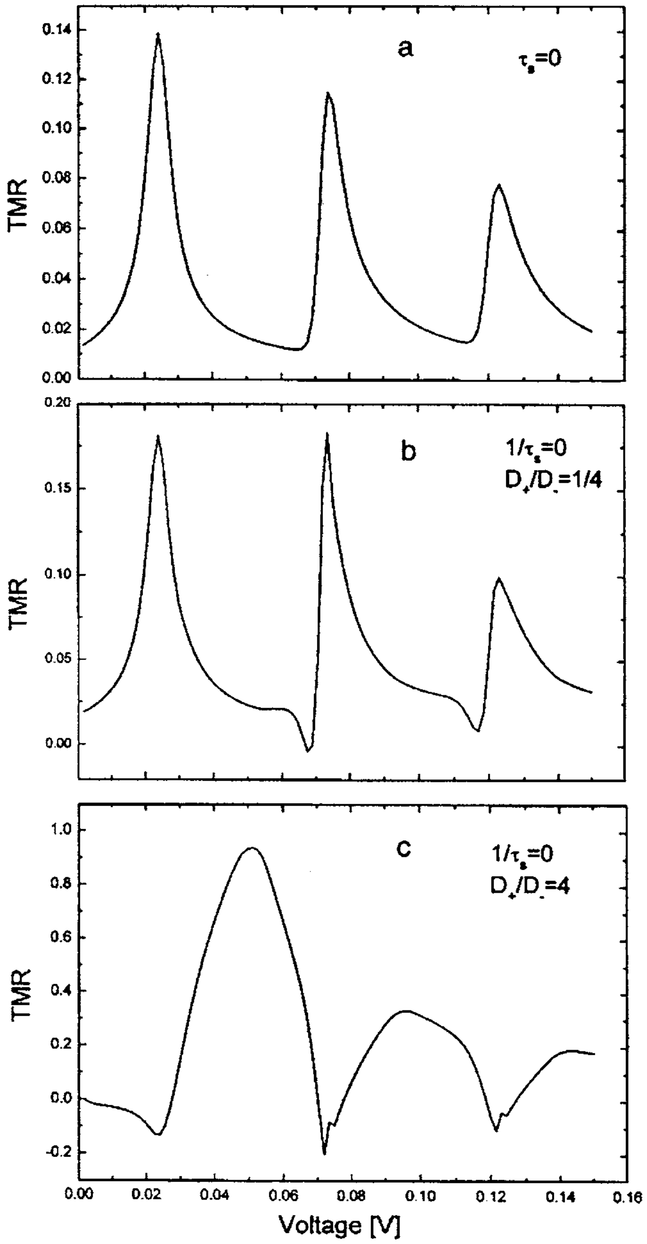

**Figure 58.** Right: TMR (denoted as the ratio $(R_{ap} - R_p)/R_p$, where $R_{ap}$ and $R_p$ are the total junction resistances in the antiparallel and parallel configurations, respectively) calculated in the limit of fast spin relaxation on the island (a) and in the limit of infinite relaxation time for $D_+/D_- = 1/4$ (b) and $D_+/D_- = 4$ (c). (From [287].)

from one part of the device to another. This can be viewed as a write–read process in which an ‘encoder’ writes spin information onto the itinerant electrons in one part of the device, which are then conveyed to a physically different part of the device where the information is read off by a ‘decoder’. Fundamentally, this information is mediated by the charge carriers and it decays on the characteristic length scale of the spin diffusion length. Therefore, the essential

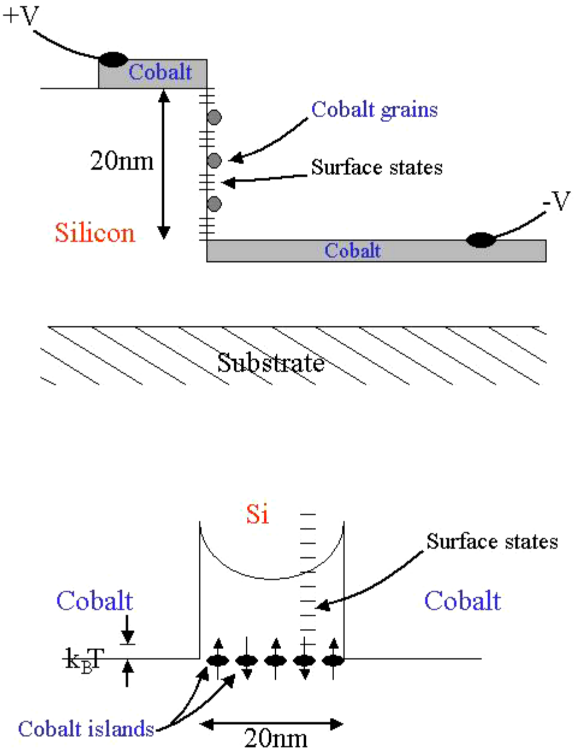

**Figure 59.** Proposed band structure for the spin blockaded Schottky barrier device.

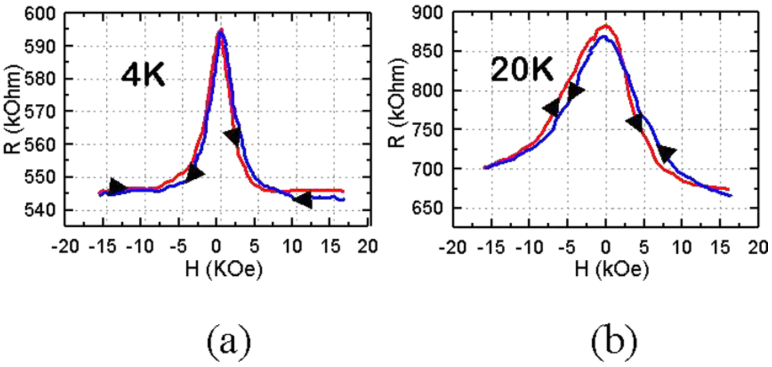

**Figure 60.** Spin blockaded Schottky barrier resistance measured at (a) 4 K and (b) 20 K. The MR effect of 25% in the latter case is unprecedented in a silicon device.

criterion for the creation of spin electronics is the ability to engineer structures whose physical dimensions are of this order of magnitude.

Ultimately, mesomagnetism serves as a medium for developing novel devices, by defining their behaviour under different operating conditions and their control mechanisms. There are many applications for ‘simple’ magnetic field detection in commercial fields as diverse as information storage and retrieval, programmable gate arrays, aviation electronics, fuel injection (for improved internal combustion engine management to reduce automotive emissions),

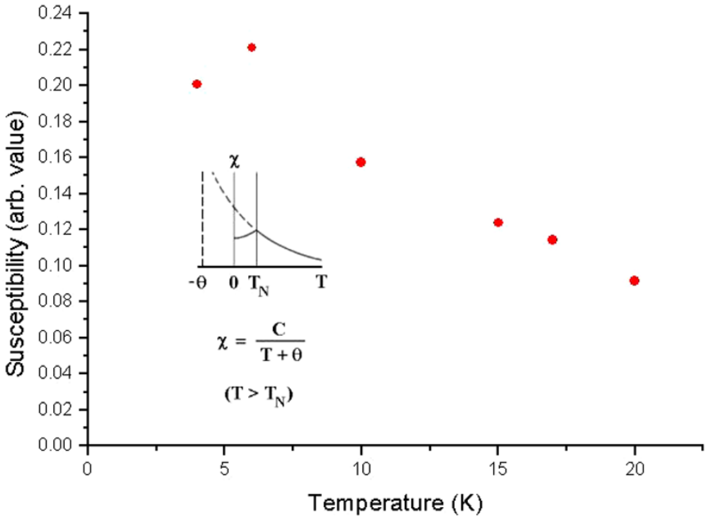

**Figure 61.** Diagram of susceptibility.

electronic engine management, automotive active safety systems (breaking and anti-skid systems, safety devices etc) and drive-by-wire control systems. As these various technologies develop, the sensitivity, stability, noise rejection and reliability specifications of the magnetic sensor elements employed become ever more demanding and there is increased pressure on the basic technology to respond to these requirements. It is the authors' view that mesomagnetism's next breakthrough may be in the RAM market using existing TJ technology. Eventually, it may spawn a new philosophy in computer memory in which the distinction between storage memory and active memory becomes less defined. The following are a few of the authors' thoughts on the future directions of meosmagnetic research.

### *9.1. Use of spin split insulators as polarizing injectors*

The transport properties of spin split europium based insulators have been studied [290, 291] at low temperatures and the resulting empirical data seem to suggest that these—or room temperature analogues thereof—might act as spin polarizers. The insulator bandgap is spin split, which means that a tunnelling quasi-particle with its energy in the bandgap sees a different tunnel barrier height depending on its spin, so its wavefunction will have a spin-dependent decay constant. For unpolarized electrons incident on a sufficiently thick barrier, there is a high spin asymmetry for the tunnel current. Therefore, this may be an ideal way to spin inject into other materials, specifically semiconductors, since there are no metals and therefore no differential material resistivities involved and no problems with Schottky barrier interface states. Although no work has been done with this material to date, this insulator/semiconductor combination affords a high degree of flexibility, including choosing where in the semiconductor band structure the spin injection occurs.

### *9.2. Fast magnetic switching*

One feature of spin electronic device performance that has not been discussed yet is device bandwidth. There are two aspects to this, device response to electrical signals and to magnetic signals. The former is determined by the same considerations that govern the speed of conventional electronics—diffusion rate, charge storage and parasitic capacitance, as well as their spin analogues. However, the latter is determined by the magnetic switching time of the spin polarizing nano-elements and is unique to spin electronics (although some analogies may be drawn between this switching time and the high frequency response of particulate recording media). Analysis of high speed magnetic switching of nano-elements has been widely researched [292, 293] and found to be highly dependent on the sample shape and the coupling of the switching mode to the spin-wave spectrum. MRAM nano-element access/write times on the order of nanoseconds are routinely achievable and are highly competitive with other memory technologies. However, higher magnetic switching speeds are desirable for future applications.

One option for faster write-time magnetic memories is optically pumped magnetic switching. This is a spin electronic device in which one of the magnetic nano-elements is a ferromagnetic spin split insulator. The memory function is contained in the orientation of this magnetic insulator relative to a metallic ferromagnetic electrode. However, since the insulator is optically transparent, its moment might be reversed very rapidly by connecting the Zeeman energy reservoir to a suitable optical transition energy reservoir by off-resonance optical irradiation. This would function as a high frequency analogue of dynamic nuclear polarization [294]. An alternative scheme might involve optical–microwave double resonance in which the device is continuously bathed in microwave radiation and the switching is achieved by exposure to a short pulse of optical radiation. A third option might be to combine a ferromagnetic film, a spin split magnetic insulator and a normal metal. The memory function would then be comprised of the magnetic configurations of the magnetic metal and the magnetic insulator. The former would be magnetically pinned and the latter would be rapidly switchable by optical double resonance techniques.

### *9.3. The spin diode*

Originally proposed by Mattheis [295], this two-terminal spin device called a spin diode consists of a five-layer magnetic system in which three ferromagnetic metal layers are each separated by a thin paramagnetic metal layer. From left to right the ferromagnetic layer magnetizations point respectively along the $y$-, $z$- and $x$-directions. $Y$-polarized spins leaving the first layer precess 90° about the $z$-oriented magnetization in the second layer (whose thickness is set according to the spin precession frequency) and end up parallel to the $x$-oriented third layer, and therefore continue through it. However, if the spins transfer in the opposite direction from the right-hand $x$-oriented layer, they precess 90° in the centre layer and end up antiparallel to the $y$-orientation of the left-hand layer, and therefore are unable to continue due to a lack of density of states of the right orientation. Thus, the entire system functions as a spin diode that is capable of fulfilling the memory and blocking function of a two-terminal MRAM element in one device. Tunnel versions of this device should also be realizable which, because their function is completely determined by the asymmetry in the density of states, should offer higher on/off ratios.

### *9.4. Quantum coherent spin electronics*

Perhaps the most far reaching development in spin electronics will be the establishment of quantum coherent spin devices. These are devices whose construction is on a sufficiently short length scale that the quantum coherence of the electronic wavefunction is preserved across the device, thereby coupling input and output electrical signals. Although the spin diffusion length is the determining length scale for spin electronics, it is the least exacting length scale

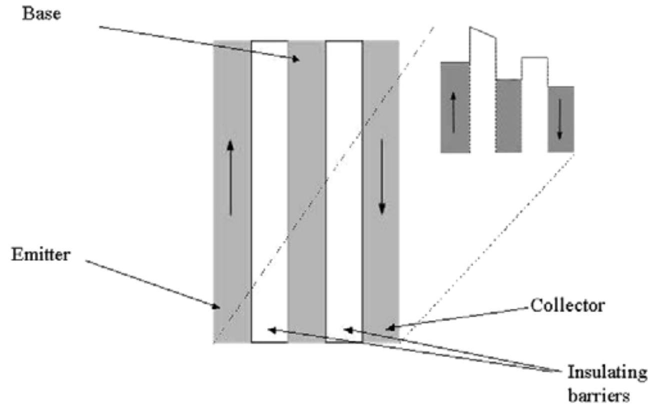

**Figure 62.** Tunnel-grid spin triode.

to reach, since it is typically thousands of Ångstroms for pure metals. At the other end is the quantum coherence length which is of the order of the mean free path—i.e. comparable with the length scale on which momentum scattering events occur—and is typically tens of Ångstroms upwards. On a slightly longer length scale are inelastic scattering events that change not only the momentum, but also the energy of the carriers.

Nanofabrication technology has advanced to the point that devices can be constructed on the ten Ångstrom scale. A typical example is the double-barrier resonant tunnel diode—three metal layers sandwiching two insulating layers—which relies on quantum mechanical interference between opposite faces of the central potential well for its operation. Since insulating barriers can now be fabricated with Ångstrom precision, it is only a short step from this to a spin transistor whose emitter, base and collector are phase coherent. (This concept was first suggested in the patent of Ounadjela and Hehn, with a recent theoretical analysis offered by Wilczynski and Barnas [296].) Other examples include SETs, FSETs, certain types of spin tunnel transistor and a spin triode.

*9.4.1. The tunnel-grid spin triode.* One spin electronic version of the double-barrier resonant tunnel diode uses a ferromagnetic collector and emitter and a third electrical contact to the non-magnetic base layer, shown in figure 62. As discussed above, the base layer is thin compared with the hot electron mean free path, so little carrier scattering occurs in the base and the phase coherence of the electrons launched by the emitter is preserved into the collector. Furthermore, during operation, the base and collector are biased progressively more positive relative to the emitter. However, although the base layer does not appreciably scatter the carriers and so does not demand significant base current, it is nonetheless substantial enough to define the electrostatic potential across the successive barriers and to modulate the current tunnelling from emitter to collector. In this respect, the base is not unlike the grid electrode in a vacuum triode. Therefore, this device controls the emitter–collector conductance by applying a potential to a high impedance base, thereby generating power gain. Moreover, owing to the ferromagnetic nature of the electrodes, the device characteristics are also switchable by applying an external magnetic field. Another variant is shown in figure 63, which uses a spin split insulator as the spin polarizing injector stage.

*9.4.2. Multilayer quantum interference spin stacks.* A more elaborate quantum coherent structure may be made which is similar to optical thin film interference filters in which stacks

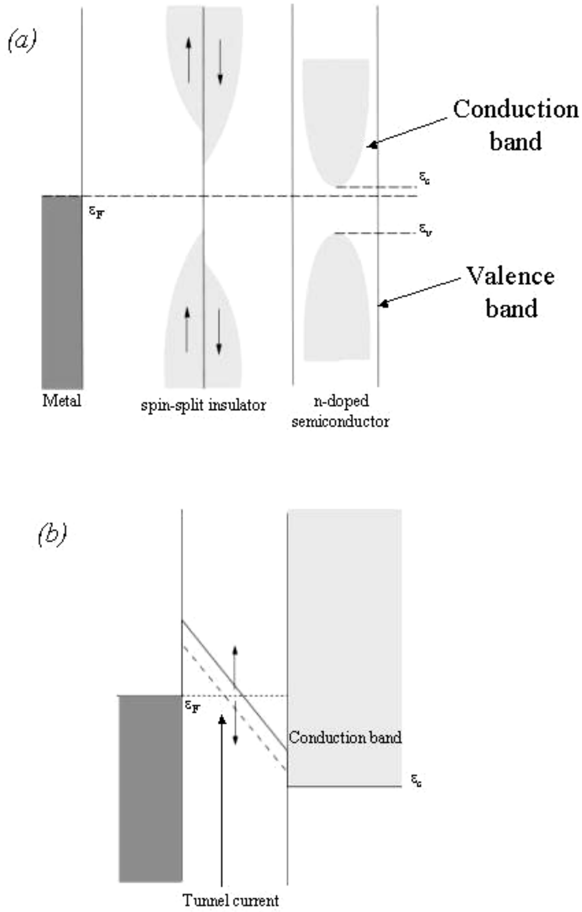

**Figure 63.** Spin split insulator injector: (a) unbiased and (b) biased.

of $\lambda/4$ dielectric layers are cascaded to provide special optical transfer functions. In like manner, combinations of $\lambda/4$ metal films and tunnel barriers may achieve analogous electrical transport effects. In particular, resonant thin film structures in which the magnetic 'refractive index' changes with a change in magnetization or spin direction can be used to modify the resonant conditions and change the transfer function of the multilayer stack.

*9.4.3. Quantum information technology.* Potentially, spin electronics could find its biggest impact in the world of quantum information technology [297]. The relatively simple spin electronic devices which have been demonstrated to date—such as GMR devices and MTJs—function by coding spin information onto the electrical carriers in one part of the device and reading it back in another remote region of the device. In short, contemporary spin electronics functions by transfer of streams of single qubits from one part of the spin electronic circuit to another. Viewed in this manner, this is just the simplest possible type of quantum information transfer in which no entanglement is involved. The next stage would be to implement devices which function by displacing spin information by means of entangled qubit pairs. For example, multi-terminal spin devices of the future might use streams of entangled qubits to communicate between different device terminals, each of which receives one qubit component of the entangled ensemble. A practical realization of such a device might be attempted using combinations of FSETs.

The FSET is a particularly important stepping-stone on the path to quantum information processing. Its distinguishing feature is that it is a rare example of a quantum processor in which the qubits (e.g. the spins) may be physically displaced, allowing the gates and their implementation hardware to be spatially localized as in conventional computing. Competing quantum processor hardware, such as nuclear magnetic resonance processors, has fixed qubits and peripatetic gates. Coupled with this configurational advantage, the FSET is also endowed with an automatic electrical facility for measuring and collapsing the qubit. These two attributes alone position it in the forefront of potential candidates for future quantum information processing hardware.

While the realization of a full blown quantum computer is a long way into the future (due to the monumental problems of overcoming uncontrolled quantum decoherence and parasitic interactions of qubits), the more modest aim of implementing demonstrators of basic quantum information processing hardware is feasible in the medium term. Particularly intriguing would be to explore their use in quantum dense coding, in which fractions of entangled qubits are used to carry increased information capacity compared to classical bit-streams. This might be achieved by using pairs of FSETs, each of which is fed entangled qubit spins by a central generator, and each of which is equipped with gate hardware capable of executing the basic single-qubit operators $X$, $Y$, $Z$, $H$ and $P(\theta)$, which are used to decode the entangled dual spin states. In the simplest case, the gates might consist simply of ferromagnetic layer sandwich structures with differing anisotropy axes in combination with ultra-fast switching microwave pulsing.

A simpler task, which could be investigated to gain insight into the functioning of this hardware, is the matter of transmitting quantum encrypted data. This has been achieved experimentally using polarized light (see for example [298] or [299]), but not yet with localized qubits. The problem is to transmit single qubits with one of two orthogonal quantization axes and then project them upon arrival onto similar axes. Interception of the data may then be detected by monitoring the bit-stream error rate, which must remain lower than 25% for guaranteed secure transmission. This configuration might be implemented using assemblies of three connected FSETs.

The main obstacles in quantum information processing are unsolicited interaction, quantum decoherence and data corruption by noise. A key element in any successful programme will be to reduce these effects to a the minimum necessary to demonstrate functioning of such primitive quantum hardware as has been outlined above. In particular, methods need to be developed to introduce quantum error correction and spin regeneration that do not violate the ‘no-qubit’ cloning rule.

## Acknowledgments

This work has been funded through several EC programs: the Training and Mobility of Researchers program DynaSpin (FMRX-CT97-0124), the EC program Magnoise (IST-1999-10849) and the EC program NanoMEM (IST-1999-13471).

## References

[1] Grünberg P 2001 *Phys. Today* **5** 31–7
[2] Kittel C 1949 *Rev. Mod. Phys.* **21** 541–83
[3] Hubert A and Schäfer R 1998 *Magnetic Domains—the Analysis of Magnetic Microstructures* (Berlin: Springer)
[4] Hehn M, Ounadjela K, Bucher J-P, Rousseaux F, Decanini D, Bartenlian B and Chappert C 1996 *Science* **272** 1782

[5] Ounadjela K, Hehn M and Ferré R 1997 *Magnetic Hysteresis in Novel Magnetic Materials* ed G Hadjipanayis (New York: Academic) p 485

[6] Weiss P 1907 *J. Physique Radium* **6** 661–90

[7] Weiss P and Foex G 1926 *Le Magnétism (Magnetism)* (Paris: Armand Colln)

[8] Andelman D 1996 *Recherche* **284** 411–13

[9] Rosensweig R E 1985 *Ferrohydrodynamics* (Cambridge: Cambridge University Press)

[10] Muller P and Gallet F 1991 *J. Phys. Chem.* **95** 3257–62

[11] Landau L D 1943 *J. Phys. USSR* **7** 99

[12] Fayt R, Hadjiandreou P and Teyssie P 1985 *J. Polym. Sci. Chem* **23** 337

[13] Sixtus K J and Tonks L 1931 *Phys. Rev.* **37** 930–58

[14] Bitter F 1932 *Phys. Rev.* **41** 507–15

[15] Landau L D and Lifshitz E 1935 *Phys. Z. Sowjetunion* **8** 153–69

[16] Vleck J H V 1945 *Rev. Mod. Phys.* **17** 27–47

[17] Craik D 1995 *Magnetism Principles and Applications* (New York: Wiley)

[18] Guggenheim E A 1936 *Proc. R. Soc.* A **155** 49–70

[19] Fokker A D 1939 *Physica* **6** 791–6

[20] Osborn J A 1945 *Phys. Rev.* **67** 351–7

[21] Williams H J, Bozorth R M and Shockley W 1949 *Phys. Rev.* **70** 965–71

[22] Chikazumi S 1997 *Physics of Ferromagnetism* (Oxford: Oxford University Press) ch 17

[23] Bloch F 1932 *Z. Phys.* **74** 295–335

[24] Néel L 1955 *C. R. Acad. Sci., Paris* **241** 533–6

[25] Malozemoff A P and Slonczewski J C 1979 *Magnetic Domain Walls in Bubble Materials* (New York: Academic)

[26] Bobeck A H and Torre E D 1975 *Magnetic Bubbles* (Amsterdam: North-Holland)

[27] Eschenfelder A H 1980 *Magnetic Bubble Technology* (Berlin: Springer)

[28] Eschenfelder A H 1981 *Magnetic Bubble Technology* 2nd edn (Berlin: Springer)

[29] Kittel C 1946 *Phys. Rev.* **70** 965

[30] Kooy C and Enz U 1960 *Philips Res. Rep.* **15** 7

[31] Hehn M, Padovani S, Ounadjela K and Bucher J-P 1996 *Phys. Rev.* B **54** 3428

[32] Ebels U, Buda L, Wigen P E and Ounadjela K 2001 *Spin Dynamics in Confined Magnetic Structures* ed B Hillebrands and K Ounadjela (Berlin: Springer) ch 6

[33] Gehanno V, Marty A, Gilles B and Samson Y 1997 *Phys. Rev.* B **55** 12552

[34] Gehanno V, Samson Y, Marty A, Gilles B and Chamberod A 1997 *J. Magn. Magn. Mater.* **172** 26

[35] Asenjo A, Garcia J M, Garcia D, Hernando A, Vazquez M, Caro P A, Ravelosona D, Cebollada A and Briones F 1999 *J. Magn. Magn. Mater.* **196** 23

[36] Folks L, Ebels U, Sooryakumar R, Weller D and Farrow R F C 1999 *J. Magn. Soc. Japan* **23** 85

[37] Wirth S, Field M, Awschalom D D and Molnár S v 1998 *Phys. Rev.* B **57** R14028

[38] Fruchart O, Klaua M, Barthel J and Kirschner J 1999 *Phys. Rev. Lett.* **83** 2769

[39] Sun S, Murray C B, Weller D, Folks L and Moser A 2000 *Science* **287** 1989

[40] Puntes V F, Krishnan K M and Alivisatos A P 2001 *Appl. Phys. Lett.* **78** 2187

[41] Jin Y, Dennis C L and Majetich S A 1999 *Nanostruct. Mater.* **12** 763

[42] Cowburn R P, Koltsov D K, Adeyeye A O and Welland M E 1998 *Appl. Phys. Lett.* **73** 3947

[43] Pardoe H, Anusorn W C, Pierre T G S and Dobsonb J 2001 *J. Magn. Magn. Mater.* **225** 41

[44] Yamamuro S, Sumiyama K, Konno T J and Suzuki K 1999 *Mater. Trans. JIM* **40** 1450

[45] Petit C, Cren T, Roditchev D, Sacks W, Klein J and Pileni M P 1999 *Adv. Mater.* **11** 1198

[46] Dormann J L, Fiorani D and Tronc E 1999 *J. Magn. Magn. Mater.* **202** 251

[47] Hansen M F and Morup S 1998 *J. Magn. Magn. Mater.* **184** 262

[48] Scheinfein M R, Schmidt K E, Helm K R and Hembree G G 1996 *Phys. Rev. Lett.* **76** 1541

[49] Gu E, Ahmad E, Gray S J, Daboo C, Bland J A C, Brown L M, Rührig M, McGibbon A J and Chapman J N 1997 *Phys. Rev. Lett.* **78** 1158

[50] Demand M, Hehn M, Ounadjela K, Stamps R L, Cambril E, Cornette A and Rousseaux F 2000 *J. Appl. Phys.* **87** 5111

[51] Shinjo T, Okuna T, Hassdorf R, Shigeto K and Ono T 2000 *Science* **289** 29

[52] Schneider M, Hoffmann H and Zweck J 2000 *Appl. Phys. Lett.* **77** 2909

[53] Cowburn R P 2000 *J. Physique* D **33** R1

[54] Allenspach R and Stampanoni M 1992 *Magnetic Surfaces, Thin Films and Multilayers* vol 231, ed S S P P Parkin and H Hopater (Pittsburgh, PA: Materials Research Society) p 17

[55] Hehn M 1997 *PhD Thesis* Université Louis Pasteur

[56] Hehn M, Ferré R, Ounadjela K, Bucher J-P and Rousseaux F 1997 *J. Magn. Magn. Mater.* **165** 5

[57] Ferré R, Hehn M and Ounadjela K 1997 *J. Magn. Magn. Mater.* **165** 9

[58] Cowburn R P, Adeyeye A O and Welland M E 1998 *Phys. Rev. Lett.* **81** 5414

[59] Gomez R D, Luu T V, Pak A O, Kirk K J and Chapman J N 1999 *J. Appl. Phys.* **85** 6163

[60] Cowburn R P, Koltsov D K, Adeyeye A O, Welland M E and Tricker D M 1999 *Phys. Rev. Lett.* **83** 1042

[61] Demand M 1998 *PhD Thesis* Université Louis Pasteur

[62] Raabe J, Pulwey R, Sattler R, Zweck T and Weiss D 2000 *J. Appl. Phys.* **88** 4437

[63] Pokhil T, Song D and Nowak J 2000 *J. Appl. Phys.* **87** 6319

[64] Fernandez A and Cerjan C J 2000 *J. Appl. Phys.* **87** 1395

[65] Fernandez A, Gibbsons M R, Wall M A and Cerjan C J 1998 *J. Magn. Magn. Mater.* **190** 71

[66] Girgis E, Schelten J, Shi J, Janeski J, Tehrani S and Goronkin H 2000 *Appl. Phys. Lett.* **76** 3780

[67] Kleiber M, Kümmerlein F, Löhndorf M, Wadas A, Weiss D and Wiesendanger R 1998 *Phys. Rev.* B **58** 5563

[68] Stoner E C and Wohlfarth E P 1948 *Phil. Trans. R. Soc.* A **240** 599

[69] Néel L 1947 *C. R. Acad. Sci., Paris* **224** 1550

[70] Legrand J, Petit C, Bazin D and Pileni M P 2000 *Appl. Surf. Sci.* **164** 186

[71] http://www.ctcms.nist.gov/ rdm/mumag.org.html

[72] Buda L D, Prejbeanu I L, Demand M, Ebels U and Ounadjela K 2001 *IEEE Trans. Magn.* **37** 2061–3

[73] Miltat J 1994 *Applied Magnetism* ed C D W R Gerber and G Asti (Dordrecht: Kluwer) p 221

[74] Schabes M E and Bertram H N 1988 *J. Appl. Phys.* **64** 1347

[75] Zheng Y and Zhu J 1997 *J. Appl. Phys.* **81** 5471

[76] Kirk K J, Chapman J N and Wilkinson C D W 1997 *Appl. Phys. Lett.* **71** 539

[77] Shi J, Zhu T, Durlam M, Chen E, Tehrani S, Zheng Y F and Zhu J-G 1998 *IEEE Trans. Magn.* **34** 997–9

[78] Gadbois J, Zhu J-G, Vavra W and Hurst A 1998 *IEEE Trans. Magn.* **34** 1066

[79] Rührig M, Khamesehpour B, Kirk K J, Chapman J N, Aitchison P, McVitie S and Wilkinson C D W 1996 *IEEE Trans. Magn.* **32** 4452

[80] Zhu J G, Zheng Y and Prinz G A 2000 *J. Appl. Phys.* **87** 6668

[81] Zhu J and Prinz G A 2000 *Data Storage* **40**

[82] Li S P, Peyrade A, Natali M, Lebib A, Chen Y, Ebels U, Buda L D and Ounadjela K 2001 *Phys. Rev. Lett.* **86**

[83] Wernsdorfer W, Doudin B, Mailly D, Hasselbach K, Benoit A, Meier J, Ansermet J-P and Barbara B 1996 *Phys. Rev. Lett.* **77** 1873

[84] Ledermann M, Barr R O and Schultz S 1997 *IEEE Trans. Magn.* **31** 3793

[85] Ferré R, Ounadjela K, George J M, Piraux L and Dubois S 1997 *Phys. Rev.* B **56** 14066

[86] Wegrowe J-E, Kelly D, Franck A, Gilbert S E and Ansermet J-P 1999 *Phys. Rev. Lett.* **82** 3681

[87] Prejbeanu I L, Buda L D, Ebels U and Ounadjela K 2000 *Appl. Phys. Lett.* **77** 3066

[88] Hubert A 1985 *IEEE Trans. Magn.* **21** 1604

[89] Prejbeanu I L, Buda L D, Ebels U, Viret M, Fermon C and Ounadjela K 2001 *IEEE Trans. Magn.* **37** 2108–10

[90] Piraux L, Dubois S, Ferain E, Legras R, Ounadjela K, George J-M, Maurice J-L and Fert A 1997 *J. Magn. Magn. Mater.* **165** 352

[91] Ferain E and Legras R 1997 *Nucl. Instrum. Methods* B **131** 97 and references therein

[92] Maurice J-L, Imhoff D, Etienne P, Durand O, Dubois S, Piraux L, George J-M, Galtier P and Fert A 1998 *J. Magn. Magn. Mater.* **184** 1

[93] Aharoni A 1996 *Introduction to the Theory of Ferromagnetism* (Oxford: Clarendon)

[94] Hinzke D and Nowak U 2000 *J. Magn. Magn. Mater.* **221** 365

[95] Handley R C O 2000 *Modern Magnetic Materials, Principles and Applications* (New York: Wiley) ch 9.2

[96] Ebels U, Radulescu A, Henry Y, Piraux L and Ounadjela K 2000 *Phys. Rev. Lett.* **84** 983

[97] Frenkel J and Dorfman J 1930 *Nature* **126** 274

[98] Majetich S A and Jin Y 1999 *Science* **284** 470

[99] Cullity B D 1972 *Introduction to Magnetic Materials* (Reading, MA: Addison-Wesley)

[100] Gider S, Shi J, Awschalom D D, Hopkins P F, Campman K L, Gossard A C, Kent A D and von-Molnar S 1996 *Appl. Phys. Lett.* **69** 3269

[101] Néel L 1949 *Ann. Géophys.* **5** 99

[102] Heukelom B and Reijen V 1954 *J. Chim. Phys.* **51** 474

[103] Bean C P and Livingston J D 1959 *J. Appl. Phys.* **30** 120S

[104] Reif F 1990 *Fundamentals of Statistical Mechanics* (New York: Springer)

[105] Majetich S A, Scott J H, Kirkpatrick E M, Chowdary K, Gallagher K and McHenry M E 1997 *Nanostruct. Mater.* **9** 291

[106] Ross C A, Chantrell R, Hwang M, Farhoud M, Savas T A, Had Y, Smith H I, Ross F M, Redjdal M and Humphrey F B 2000 *Phys. Rev.* B **62** 14252

[107] Brown W F 1963 *Phys. Rev.* **130** 1677

[108] Wernsdorfer W, Orozco E B, Hasselbach K, Benoit A, Barbara B, Demoncy N, Loiseau A, Pascard H and Mailly D 1997 *Phys. Rev. Lett.* **78** 1791

[109] Hansen M F, Bodker F, Morup S, Lefmann K, Clausen K N and Lindgard P-A 1997 *Phys. Rev. Lett.* **79** 4910

[110] Bean C P and Jacobs I S 1956 *J. Appl. Phys.* **27** 1448

[111] Weil L 1954 *J. Chim. Phys.* **51** 715

[112] Weil L and Gruner L 1956 *C. R. Acad. Sci., Paris* **243** 1629

[113] Frydman A, Kirk T L and Dynes R C 2000 *Solid. State Commun.* **114** 481

[114] Kravtsov E, Lauter-Pasyuk V, Lauter H J, Toperverg B, Nikonov O, Petrenko A, Milyaev M, Romashev L and Ustinov V 2001 *Physica* B **297** 118

[115] Chassaing H, Morrone A and Schmidt J E 2000 *Electrochemical Technology Applications in Electronics. Proc. 3rd Int. Symp. (Electrochem. Soc. Proc. vol 99-34)* (Pennington, NJ: Electrochemical Society)

[116] Sankar S, Berkowitz A E and Smith D J 2000 *Phys. Rev.* B **62** 14273

[117] Bellouard C, Delcroix P and le-Caer G 2000 *Mater. Sci. Forum* **343–346** 819

[118] Kuzminski M, Waniewska A S and Lachowicz H K 1999 *IEEE Trans. Magn.* **35** 2853

[119] Rozenberg E, Shames A I, Gorodetsky G, Pelleg J and Felner I 1999 *J. Magn. Magn. Mater.* **203** 102

[120] Pohorilyi A N, Kravetz A F, Shipil E V, Vovk A Y, Kim C S and Khan H R 1998 *J. Magn. Magn. Mater.* **186** 87

[121] Madurga V, Ortega R J, Korenivski V and Rao K V 1996 *Proc. Science and Technology of Atomically Engineered Materials* vol 26 (Singapore: World Scientific) pp 619–25

[122] Sugiyama T and Nittono O 1996 *J. Magn. Magn. Mater.* **156** 143

[123] Zhang S Y and Cao Q Q 1996 *J. Appl. Phys.* **79** 6261

[124] Holody P, Steren L B, Morel R, Fert A, Loloee R and Schroeder P A 1994 *Phys. Rev.* B **50** 12999

[125] Cowburn R P, Koltsov D K, Adeyeye A O and Welland M E 2000 *J. Appl. Phys.* **87** 7082

[126] Stamm C, Marty F, Vaterlaus A, Weich V, Egger S, Maier U, Ramsperger U, Fuhrmann H and Pescia D 1998 *Science* **282** 449

[127] Kachkachi H, Noguès M, Tronc E and Garanin D A 2000 *J. Magn. Magn. Mater.* **221** 158

[128] Christou G, Gatteschi D, Hendrickson D N and Sessoli R 2000 *MRS Bull.* **25** 66

[129] Suber L, Zysler R, Santiago A G, Fiorani D, Angiolini M, Montone A and Dormann J L 1998 *Mater. Sci. Forum* **269–272** 937

[130] Kodama R H and Berkowitz A E 1999 *Phys. Rev.* B **59** 6321

[131] Malaescu I and Marin C N 2000 *J. Magn. Magn. Mater.* **218** 91

[132] Hesse J, Bremers H, Hupe O, Veith M, Fritscher E W and Valtchev K 2000 *J. Magn. Magn. Mater.* **212** 153

[133] Garcia-Otero J, Porto M, Rivas J and Bunde A 2000 *Phys. Rev. Lett.* **84** 167

[134] Berkowitz A E 1991 *Science and Technology of Nanostructured Magnetic Materials* vol 11 (New York: Plenum)

[135] Chudnovsky E M and Tejada J 1998 *Macroscopic Quantum Tunneling of the Magnetic Moment* (Cambridge: Cambridge University Press)

[136] Chudnovsky E M and Gunther L 1988 *Phys. Rev. Lett.* **60** 661

[137] Chudnovsky E 1994 *Phys. Rev. Lett.* **72** 3433

[138] Frei E H, Shtrikman S and Treves D 1957 *Phys. Rev.* **106** 446

[139] Brown W F 1957 *Phys. Rev.* **105** 1479

[140] Brown W F 1968 *J. Appl. Phys.* **39** 993

[141] Aharoni A and Shtrikman S 1958 *Phys. Rev.* **109** 1522

[142] Aharoni A 1966 *Phys. Status Solidi* **16** 3

[143] Stauffer D 1976 *Solid State Commun.* **18** 533

[144] Zaslavskii O B 1990 *Phys. Rev.* B **42** 992

[145] Miguel M C and Chudnovsky E M 1996 *Phys. Rev.* B **54** 388

[146] Kim G-H and Hwang D S 1997 *Phys. Rev.* B **55** 8918

[147] Fujikawa K 1998 *Phys. Rev.* E **57** 5023

[148] Chudnovsky E M 1996 *Phys. Rev.* B **54** 5777

[149] Liang J-Q, Müller-Kirsten H J W, Nie Y-H, Pu F-C and Zhang Y-B 1998 *Phys. Lett.* A **248** 434

[150] Gunther L and Barbara B 1994 *Phys. Rev.* B **49** 3926

[151] Braun H-B, Kyriakidis J and Loss D 1997 *Phys. Rev.* B **56** 8129

[152] Barbara B, Sampaio L C, Wegrowe J E, Ratnam B A, Marchand A, Paulsen C, Novak M A, Tholence J L, Uehara M and Fruchart D 1993 *J. Appl. Phys.* **73** 6703–8

[153] Kim G-H 1999 *J. Appl. Phys.* **86** 6291

[154] Lü R, Zhu J-L, Wang X-B and Chang L 1999 *Phys. Rev.* B **60** 4101

[155] Tejada J, Hernandez J M and Barco E d 1999 *J. Magn. Magn. Mater.* **196/197** 552

[156] Sappey R, Vincent E, Ocio M and Hammann J 2000 *J. Magn. Magn. Mater.* **221** 87

[157] Awschalom D D, McCord M A and Grinstein G 1990 *Phys. Rev. Lett.* **65** 783

[158] Coppinger F, Genoe J, Maude D K, Gennser U, Portal J C, Singer K E, Rutter P, Taskin T, Peaker A R and Wright A C 1995 *Phys. Rev. Lett.* **75** 3513

[159] Thomas L, Lionti F, Ballou R, Gatteschi D, Sessoli R and Barbara B 1996 *Nature* **383** 145

[160] Lionti F, Thomas L, Ballou R, Barbara B, Sulpice A, Sessoli R and Gatteschi D 1997 *J. Appl. Phys.* **81** 4608

[161] Barbara B, Thomas L, Lionti F, Chiorescu I and Sulpice A 1999 *J. Magn. Magn. Mater.* **200** 167

[162] Evangelisti M and Bartolomé J 2000 *J. Magn. Magn. Mater.* **221** 99

[163] Wernsdorfer W, Orozco E B, Hasselbach K, Benoit A, Mailly D, Kubo O, Nakano H and Barbara B 1997 *Phys. Rev. Lett.* **79** 4014

[164] Wernsdorfer W, Orozco E B, Barbara B, Benoit A, Mailley D, Demoncy N, Pascard H, Kubo O and Nakano H 1998 *IEEE Trans. Magn.* **34** 973

[165] Tejada J, Zhang X X, Barco E d, Hernández J M and Chudnovsky E M 1997 *Phys. Rev. Lett.* **79** 1754

[166] Zhang X X, Tejada J, Hernandez J M and Ziolo R F 1997 *Nanostruct. Mater.* **9** 301

[167] Caneschi A, Gatteschi D, Sangregorio C, Sessoli R, Sorace L, Cornia A, Novak M A, Paulsen C and Wernsdorfer W 1999 *J. Magn. Magn. Mater.* **200** 182

[168] Batlle X, Garcia del Muro M and Labarta A 1997 *Phys. Rev.* B **55** 6440

[169] Gregg J F, Allen W, Viart N, Kirschman R, Sirisathitkul C, Schille J P, Gester M, Thompson S, Sparks P, da Costa V, Ounadjela K and Skvarla M 1997 *J. Magn. Magn. Mater.* **175** 1

[170] Gurney B A, Speriosu V S, Nozieres J P, Lefakis H, Wilhoit D R and Need O U 1993 *Phys. Rev. Lett.* **71** 4023

[171] Dieny B 1992 *J. Phys.: Condens. Matter* **4** 1

[172] Yang Q, Holody P, Lee S-F, Henry L L, Loloee R, Schroeder P A W P, Pratt J and Bass J 1994 *Phys. Rev. Lett.* **72** 3274

[173] Pugh D I 2001 *Thesis* University of York

[174] Kikkawa J M and Awschalom D D 1999 *Nature* **397** 139

[175] Kikkawa J M, Smorchkova I P, Samarth N and Awschalom D D 1997 *Science* **277** 1284

[176] Awschalom D D and Samarth N 2000 *J. Supercond.* **13** 201

[177] Dzhioev R I, Zakharchenya B P, Korenev V L and Stepanova M N 1997 *Phys. Solid State* **39** 1765–8

[178] Fabian J and Sarma S D 1999 *J. Vac. Sci. Technol.* B **17** 1708

[179] D'Yakanov M I and Perel V I 1971 *Sov. Phys.–JETP* **33** 1053

[180] D'Yakanov M I and Perel V I 1972 *Sov. Phys.–Solid State* **13** 3023

[181] D'Yakanov M I and Perel V I 1973 *Sov. Phys.–JETP* **38** 177

[182] Bir G L, Aronov A G and Pikus G E 1976 *Sov. Phys.–JETP* **42** 705

[183] Elliot R J 1954 *Phys. Rev.* **96** 266

[184] Zhu H J, Ramsteiner M, Kostial H, Wassermeier M, Schönherr H-P and Ploog K H 2001 *Phys. Rev. Lett.* **87** 16601

[185] Schwerer F C and Silcox J 1968 *Phys. Rev. Lett.* **20** 101

[186] Thompson W 1857 *Proc. R. Soc.* **8** 546–50

[187] Fert A and Campbell I A 1976 *J. Physique* F **6** 849

[188] Malozemoff A P 1985 *Phys. Rev.* B **32** 6080

[189] McGuire T R and Potter R I 1975 *IEEE Trans. Magn.* **11** 1018–38

[190] Barthelemy A, Fert A and Petroff F 1999 *Handbook of Magnetic Materials* vol 12, ed K Buschow (Amsterdam: Elsevier)

[191] Heinrich B and Bland J A C (ed) 1994 *Ultrathin Magnetic Structures* vols 1 and 2 (Berlin: Springer)

[192] Baibich M N, Broto J M, Fert A, Dau F N V, Petroff F, Eitenne P, Creuzet G, Friederich A and Chazelas J 1988 *Phys. Rev. Lett.* **61** 2472

[193] Coey J M D, Viret M and Molnár S v 1999 *Adv. Phys.* **48** 167–293

[194] Penney T, Shater M W and Torrance J B 1972 *Phys. Rev.* B **5** 3669

[195] Gregg J F, Allen W D, Ounadjela K, Viret M, Hehn M, Thomson S M and Coey J M D 1996 *Phys. Rev. Lett.* **77** 1580

[196] Viret M, Vignoles D, Cole D, Coey J M D, Allen W D, Daniel D S and Gregg J F 1996 *Phys. Rev.* B **53** 8464

[197] Wegrowe J E, Comment A, Jaccard Y, Ansermet J P, Dempsey N M and Nozieres J P 2000 *Phys. Rev.* B **61** 12216

[198] Levy P M and Zhang S 1997 *Phys. Rev. Lett.* **79** 5110

[199] Cabrera G G and Falicov L M 1975 *Phys. Rev.* B **11** 2651–9

[200] Berger L 1978 *J. Appl. Phys.* **49** 2156–61

[201] Ravelosona D, Cebollada A, Briones F, Diaz-Paniagua C, Hidalgo M A and Batallan F 1999 *Phys. Rev.* B **59** 4322

[202] Kent A D, Ruediger U, Yu J, Thomas L and Parkin S S P 1999 *J. Appl. Phys.* **85** 5243

[203] Viret M, Samson Y, Warin P, Marty A, Ott F, Sondergard E, Klein O and Fermon C 2000 *Phys. Rev. Lett.* **85** 3962

[204] Zhang S and Levy P M 1991 *J. Appl. Phys.* **69** 4786

[205] Pratt W P, Lee S-F, Slaughter J M, Loloee R, Schroeder P A and Bass J 1991 *Phys. Rev. Lett.* **66** 3060

[206] Johnson M 1991 *Phys. Rev. Lett.* **67** 3594

[207] Valet T and Fert A 1993 *Phys. Rev.* B **48** 7099

[208] Camley R E and Barnas J 1989 *Phys. Rev. Lett.* **63** 664

[209] Barnas J, Fuss A, Camley R E, Grunberg P and Zinn W 1990 *Phys. Rev.* B **42** 8110

[210] Parkin S S P, More N and Roche K P 1990 *Phys. Rev. Lett.* **64** 2304

[211] Costa A T, d'Albuquerque e Castro J, Muniz R B, Ferreira M S and Mathon J 1997 *Phys. Rev.* B **55** 3724

[212] Costa A T, d'Albuquerque e Castro J and Muniz R B 1997 *Phys. Rev.* B **56** 13697

[213] Costa A T, d'Albuquerque e Castro J and Muniz R B 1999 *Phys. Rev.* B **59** 11424

[214] Costa A T, d'Albuquerque e Castro J, Ferreira M S and Muniz R B 1999 *Phys. Rev.* B **60** 11894

[215] Bruno P and Chappert C 1991 *Phys. Rev. Lett.* **67** 1902

[216] Dieny B, Speriosu V S, Parkin S S, Gurney B A, Wilhoit D R and Mauri D 1991 *Phys. Rev.* B **43** 1297–300

[217] Tiusan C, Hehn M, Ounadjela K, Henry Y, Hommet J, Meny C, van den Berg H, Baer L and Kinder R 1999 *J. Appl. Phys.* **85** 5276–8

[218] Binasch G, Grunberg P, Saurenbach F and Zinn W 1989 *Phys. Rev.* B **39** 4828

[219] Gijs M A M and Okada M 1992 *J. Magn. Magn. Mater.* **113** 105

[220] Celinski Z and Heinrich B 1991 *J. Magn. Magn. Mater.* **99** L25

[221] Johnson M T, Purcell S T, McGee N W E, aan de Stegge J and Hoving W 1992 *Phys. Rev. Lett.* **68** 2688

[222] Toigo J W 2000 *Sci. Am.* **282** 58

[223] Rodgers P 1996 *New Sci.* **149** 34

[224] Prinz G A 1999 *J. Magn. Magn. Mater.* **200** 57

[225] van Wees B J, Houten H v, Beenakker C W J, Williamson J G, Kouwenhoven L P, van der Marel D and Foxon C T 1988 *Phys. Rev. Lett.* **60** 848

[226] Sharvin Y V 1965 *Sov. Phys.–JETP* **21** 655

[227] Muller C J, van Ruitenbeek J M and Jongh L J d 1992 *Phys. Rev. Lett.* **69** 140

[228] Pascual J I, Mendez J, Gomez-Herrero J, Baro A M, García N and Binh V T 1993 *Phys. Rev. Lett.* **71** 1852

[229] Pascual J I, Mendez J, Gomez-Herrero J, Baro A M, García N, Landman U, Luedtke W D, Bogachek E N and Cheng H P 1995 *Science* **267** 1793

[230] Olesen L, Lægsgaard E, Stensgaard I, Besenbacher F, Schiøtz J, Stoltze P, Jacobson K W and Nørskov J K 1994 *Phys. Rev. Lett.* **72** 2251

[231] Costa-Kramer J L 1997 *Phys. Rev.* B **52** R4875

[232] Costa-Kramer J L, García N and Olin H 1997 *Phys. Rev.* B **55** 12910

[233] Costa-Kramer J L, García N, García-Mochales P and Serena P A 1995 *Surf. Sci.* **342** L1144

[234] Hansen K, Lægsgaard E, Stensgaard I and Besenbacher F 1997 *Phys. Rev.* B **56** 2208

[235] Garcia N, Munoz M and Zhao Y-W 1999 *Phys. Rev. Lett.* **82** 2923

[236] Tatara G, Zhao Y-W, Muñoz M and García N 1999 *Phys. Rev. Lett.* **83** 2030

[237] Zhao Y-W, Muñoz M, Tatara G and García N 2001 *J. Magn. Magn. Mater.* **223** 169

[238] García N, Muñoz M and Zhao Y-W 2000 *Appl. Phys. Lett.* **76** 2586

[239] Versluijs J J, Bari M, Ott F, Coey J M D and Revcolevschi A 2000 *J. Magn. Magn. Mater.* **211** 212

[240] Versluijs J J, Bari M and Coey J M D 2001 *Phys. Rev. Lett.*

[241] Slonczewski J C 1996 *J. Magn. Magn. Mater.* **159** L1

[242] Berger L 1996 *Phys. Rev.* B **54** 9353

[243] Bazaliy Y B, Jones B A and Zhang S-C 1998 *Phys. Rev.* B **57** R3213

[244] Tsoi M, Jansen A G M, Bass J, Chiang W-C, Seck M, Tsoi V and Wyder P 1998 *Phys. Rev. Lett.* **80** 4281

[245] Sun J Z 1999 *J. Magn. Magn. Mater.* **202** 157

[246] Wegrowe J-E, Kelly D, Jaccard Y, Guittienne P and Ansermet J-P 1999 *Europhys. Lett.* **45** 626

[247] Myers E B, Ralph D C, Katine J A, Louie R N and Buhrman R A 1999 *Science* **285** 867

[248] Giaever I and Megerle K 1961 *Phys. Rev.* **122** 1101

[249] Tiusan C-V 2000 *PhD Thesis* Université Louis Pasteur

[250] Julliere M 1975 *Phys. Lett.* A **54** 225

[251] Maekawa S and Gafvert U 1982 *IEEE Trans. Magn.* **18** 707

[252] Tedrow P M and Merservey R 1971 *Phys. Rev. Lett.* **26** 192

[253] Moodera J S, Kinder L R, Wong T M and Meservey R 1995 *Phys. Rev. Lett.* **74** 3273
[254] Simmons J G 1963 *J. Appl. Phys.* **34** 1793–803
[255] Slonczewski J C 1989 *Phys. Rev.* B **39** 6995
[256] Landauer R 1988 *IBM J. Res. Dev.* **32** 306
[257] Mathon J 1997 *Phys. Rev.* B **56** 11810
[258] Sousa R C, Sun J J, Soares V, Freitas P P, Kling A, da Silva M F and Soares J C 1999 *J. Appl. Phys.* **85** 5258
[259] Sousa C, Sun J J, Soares V, Freitas P P, Kling A, da Silva M F and Soares J C 1995 *Appl. Phys. Lett.* **73** 3288
[260] Moodera J S, Gallagher E F, Robinson K and Nowak J 1997 *Appl. Phys. Lett.* **70** 3050
[261] MacLaren J M, Zhang X-G and Butler W H 1997 *Phys. Rev.* B **56** 11827
[262] Meservey R and Tedrow P M 1994 *Phys. Rep.* **238** 173
[263] Zhang S, Levy P M, Marley A C and Parkin S S P 1997 *Phys. Rev. Lett.* **79** 3744
[264] Bratkovsky A M 1997 *Phys. Rev.* B **56** 2344
[265] Halbritter J 1982 *Surf. Sci.* **122** 80
[266] Tsymbal E Y and Pettifor D G 1998 *Phys. Rev.* B **58** 432
[267] Sun J and Freitas P P 1999 *J. Appl. Phys.* **85** 5264
[268] Moodera J S, Nowak J, Kinder L R, Tedrow P M, van de Veerdonk R J M, Smits B A, Karnpen M V, Swagien H J M and Jonge W J M D 1999 *Phys. Rev. Lett.* **83** 3029–32
[269] Mathon J and Umerski A 1999 *Phys. Rev.* B **60** 1117–21
[270] Mathon J, Villeret M, Muniz R B, Castro J d A e and Edwards D M 1995 *Phys. Rev. Lett.* **74** 3696
[271] Ortega J E, Himpsel F J, Mankey G J and Willis R F 1993 *Phys. Rev.* B **47** 1540
[272] Segovia P, Michel E G and Ortega J E 1996 *Phys. Rev. Lett.* **77**
[273] Chui S T 1997 *Phys. Rev.* B **55** 5600–3
[274] Inoue J and Maekawa S 1999 *J. Magn. Magn. Mater.* **198/199** 167–9
[275] Moodera J S, Nowak J and van de Veerdonk R J M 1998 *Phys. Rev. Lett.* **80** 2941
[276] MacDonald A H, Jungwirth T and Kasner M 1998 *Phys. Rev. Lett.* **81** 705
[277] Mitsuzuka T, Matsuda K, Kamijo A and Tsuge H 1999 *J. Appl. Phys.* **85** 5807–9
[278] Zhang X, Li B-Z, Sun G and Pu F-C 1997 *Phys. Rev.* B **56** 5484
[279] Teresa J M D, Barthelemy A, Fert A, Contour J P, Montaigne F and Seneor P 1999 *Science* **286**
[280] Barner J B and Ruggiero S T 1987 *Phys. Rev. Lett.* **59** 807–10
[281] Amman M, Mullen K and Ben-Jacob E 1989 *J. Appl. Phys.* **65** 339
[282] Devoret M H and Grabert H 1992 *Single Charge Tunneling* (New York: Plenum)
[283] Altimeyer S, Spangenberg B and Kurz H 1995 *Appl. Phys. Lett.* **67** 569
[284] Barnas J and Fert A 1998 *Phys. Rev. Lett.* **80** 1058
[285] Majumdar K and Hershfield S 1998 *Phys. Rev.* B **57** 11521
[286] Ono K, Shimada H and Ootuka Y 1998 *J. Phys. Soc. Japan* **67** 2852
[287] Barnas J and Fert A 1998 *Europhys. Lett.* **44** 85
[288] Schelp L F, Fert A, Fettar F, Holody P, Lee S F, Maurice J L, Petroff F and Vaures A 1997 *Phys. Rev.* B **56** 5747
[289] Sirisathitkul C, Gregg J F, Petej I, Allen W, Sparks P D and Thompson S M 2002 in preparation
[290] Esaki L, Stiles P J and Molnar S v 1967 *Phys. Rev. Lett.* **19** 852
[291] Moodera J S, Hao X, Gibson G A and Meservey R 1988 *Phys. Rev. Lett.* **61** 637
[292] Stamps R L and Hillebrands B 1999 *Appl. Phys. Lett.* **75** 1143
[293] Shi X, Koeppe P V and Kryder M H 1991 *IEEE Trans. Magn.* **27** 4942
[294] Abragam A and Goldman M 1982 *Nuclear Magnetism: Order and Disorder* (Oxford: Oxford University Press)
[295] Mattheis R private communication
[296] Wilczynski M and Barnas J 2001 *Sensors Actuators* A **91** 188
[297] Steane A 1998 *Rep. Prog. Phys.* **61** 117
[298] Phoenix S J D and Townsend P D 1995 *Cryptography and Coding (5th IMA Conf.)* (Berlin: Springer) pp 112–31
[299] Zbinden H, Gautier J D, Gisin N, Huttner B, Muller A and Tittle W 1997 *Electron. Lett.* **33** 586